Thermal Conductance in Spin Caloritronics

Dissertation
zur Erlangung des Grades
„Doktor der Naturwissenschaften“
am Fachbereich Physik, Mathematik und Informatik
der Johannes-Gutenberg-Universität Mainz

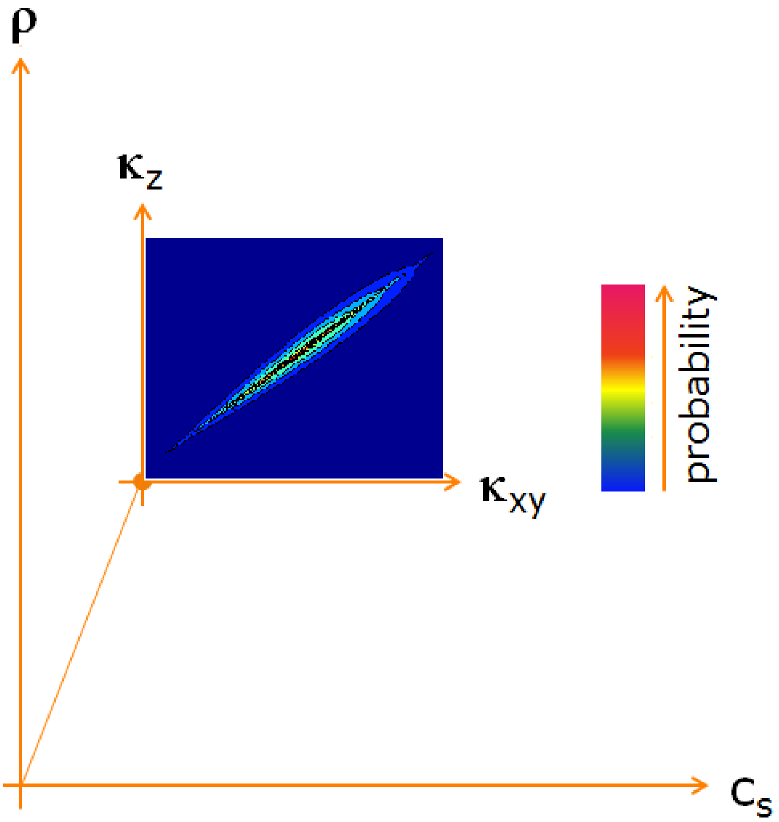

vorgelegt von
Christoph Euler
geboren in Hannover

Mainz, den 11. Dezember 2015

1. Berichterstatter: Removed due to data privacy
2. Berichterstatter: Removed due to data privacy
Datum der Prüfung: 10. Dezember 2015

ABSTRACT

Spin caloritronics is a field of research that relates the interaction of the electronic spin to a heat flow in a sample. Since the magnitude of such a heat flow is only quantifiable with precise knowledge of the thermal conductivity of the sample, this thesis studies the role of the thermal conductivity in spin caloritronics. However, the 3ω method as developed by Cahill *et al.* that is commonly used to determine the thermal conductivity in thin films is only capable of analyzing films with a thermal conductivity much lower than that of the substrate.

This thesis describes and applies a suitable extension of the original 3ω method that eliminates these shortcomings. So far, determining the thermal conductivity by this extension led to large numerical uncertainties. The novel data evaluation scheme presented here is based on Bayesian statistics in order to reduce the numerical instability.

While the majority of the projects within spin caloritronics considers the impact of a temperature gradient applied to a solid on the spin structure, this project analyzes the inverse question: How does a change in magnetic texture change the thermal conductivity of a material? In particular, such an effect of a magnetic field on the thermal conductivity was studied concerning thermal transport perpendicular to the film plane in $La_{0.67}Ca_{0.33}MnO_3$ and in the film plane in Permalloy. In both cases the measured change in thermal conductivity in the presence of a magnetic field is discussed.

Finally, as explained, the community of spin caloritronics relies on accurate values of the thin film thermal conductivity of a number of characteristic materials. Especially $Y_3Fe_5O_{12}$ (YIG) is studied frequently, so that as an example of particular interest the thin film thermal conductance of YIG is presented and analyzed.

The methods and results presented here provide a different approach to spin caloritronic research and allow a novel path to studying thermal conductivity.

ZUSAMMENFASSUNG

Spin-Kaloritronik ist ein Forschungsfeld, in dem die Wechselwirkung von Spin mit Wärmestömen untersucht wird. Da die Größe solcher Ströme nur durch genaue Kenntnis der Wärmeleitfähigkeit des Materials zu untersuchen ist, beschäftigt sich diese Arbeit mit der Rolle der Wärmeleitfähigkeit im Bereich der Spin-Kaloritronik. Allerdings ist die 3ω-Methode, wie sie von Cahill *et al.* etwickelt wurde, und die häufig verwendet wird um die Wärmeleitfähigkeit dünner Filme zu bestimmen, nicht für alle erdenklichen Film-Substrat-Systeme geeignet.

Die vorliegende Arbeit beschreibt eine geeignete Erweiterung der ursprünglichen 3ω-Methode, die diese Mängel ausgleicht, und ihre Anwendung. Bisher war die Bestimmung der Wärmeleitfähigkeit durch diese Erweiterung mit großen numerischen Unsicherheiten verbunden. Das neuartige Auswertungsschema, das hier gezeigt wird, basiert auf Bayesscher Statistik, um diese Unsicherheiten zu reduzieren.

Während sich die Mehrzahl der Projekte in der Spin-Kaloritronik mit dem Einfluss eines Temperaturgradienten auf die Spinstruktur eines Festkörpers auseinandersetzt, analysiert diese Arbeit die inverse Fragestellung: Wie beeinflusst eine Änderung der magnetischen Struktur die Wärmeleitfähigkeit eines Materials? Insbesondere wurde ein solcher Effekt eines Magnetfelds auf die Wärmeleitfähigkeit senkrecht zur Filmebene von $La_{0.67}Ca_{0.33}MnO_3$ und in der Filmebene von Permalloy untersucht. In beiden Fällen wird die gemessene Änderung der Wärmeleitfähigkeit in einem Magnetfeld diskutiert.

Schließlich beruht die Spin-Kaloritronik auf präzisen Werten der Dünnfilmwärmeleitfähigkeit relevanter Materialien. Insbesondere wird $Y_3Fe_5O_{12}$ (YIG) häufig untersucht, sodass als Beispiel von besonderem Interesse die Dünnfilmwärmeleitfähigkeit von YIG gezeigt und analysiert wird.

Die vorgestellten Methoden und Ergebnisse stellen einen anderen Blick auf die Spin-Kaloritronik und einen neuartigen Zugang zur Untersuchung der Wärmeleitfähigkeit dar.

TABLE OF CONTENTS

1. Spin Caloritronics **1**

2. Relevant Electric and Thermal Transport Processes **7**

2.1. Electronic Transport and the Wiedemann-Franz Law . . . 7
2.2. Thermal Conductance . . . 12
    2.2.1. Lattice Vibrations . . . 12
    2.2.2. Debye's T^3 Law . . . 13
    2.2.3. Scattering Processes . . . 16

3. Bayesian Data Evaluation Scheme for the 3ω Method **25**

3.1. The Original 3ω Technique . . . 27
3.2. The Two-Dimensional Expansion . . . 33
3.3. Computational Implementation . . . 37
3.4. Experimental Setup and Error Estimation . . . 43

4. Magnetothermal Resistance Perpendicular to the Film Plane **53**

4.1. The Colossal Magnetoresistive Manganite LCMO . . . 56
4.2. LCMO: Deposition and Characterization . . . 62
    4.2.1. Applied Techniques . . . 63
    4.2.2. Results . . . 66
4.3. Magnetothermal Resistance in LCMO . . . 71
4.4. Phonon Spectrum in LCMO . . . 77
    4.4.1. Basics of Raman Spectroscopy . . . 77
    4.4.2. Previous Research . . . 80
    4.4.3. Temperature Dependent Raman Spectroscopy . . . 82

5. Magnetothermal Resistance In the Film Plane 89
5.1. The Anisotropic Magnetoresistance 90
5.2. Magnetothermal Resistance in Permalloy 91
5.3. Discussion 96

6. Thin Film Thermal Conductance of YIG 99
6.1. Previous Research 99
6.2. Thickness Dependence and Magnetic Field Contribution 101

7. Conclusion and Outlook 113

A. Temperature Profile of the PLD Heater 115

List of Figures 117

Bibliography 123

List of Publications 135

Acknowledgments 137

Curiculum Vitae 139

CHAPTER 1

SPIN CALORITRONICS

The charge property of electrons is the foundation of any type of electronics and the success thereof is, amongst other indicators, quantified by Moore's law, that demonstrates an exponential increase in performance of computer technology. However, a significant caveat of electronics and increasing miniaturization is the abundance of waste heat, so that besides the acceleration of computation the temperature control is a crucial point in research.

Apart from the application in electronics, electron charge can be used to generate heat from an electric potential difference, or vice versa, as is known from traditional thermoelectrics, which is a commonly applied method of regenerating waste heat. While in electronics an electric field gives rise to an electric current, in thermoelectrics a temperature gradient results in charge transport, and also the inverse process is possible. For several centuries the Seebeck, Peltier and Nernst effects have been known as a consequence of the interplay between heat and charge.

Thermoelectricity stems from an asymmetry at the Fermi level in metals with respect to electrons and holes. Heat currents $\mathbf{Q}$ transform some of their energy to kinetic energy of electrons and thus generate an electric field $\mathbf{E}$, which is related to a charge current $\mathbf{J}_c$ and a temperature gradient ∇T as

$$\begin{pmatrix} \mathbf{E} \\ \mathbf{Q} \end{pmatrix} = \begin{pmatrix} \frac{1}{\sigma} & S \\ \mathit{\Pi} & \kappa \end{pmatrix} \begin{pmatrix} \mathbf{J}_c \\ -\nabla T \end{pmatrix}, \tag{1.1}$$

where σ is the electric conductivity, S the Seebeck coefficient, $\mathit{\Pi}$ the Peltier coefficient relating S and the temperature T by $\mathit{\Pi} = ST$, and κ the thermal conductivity (Bauer et al., 2012). The relation between the Peltier and Seebeck coefficients physically originates from the Onsager reciprocity of the Peltier and Seebeck effects, that states that a gradient in a property causes a flux in a second quantity.

In information technology the second intrinsic property of electrons, their spin property, has frequently been ignored. The technological rediscovery of electron spin in the 1990s subsequently led to the development of prototypes of spin-based 'spintronic' devices. Spintronics offers the opportunity to generate devices that not only apply standard electronics, but in addition take advantage of spin-dependent effects that arise from the interaction of electron spin and magnetization of the material. Spintronic devices include read heads and sensors as used in hard disks or cars, spin transfer mechanisms or magnetic memory (e.g. MRAM). Spin caloritronics is set at the third edge of the triangle composed of charge, heat and spin (Fig. 1.1) and studies the interdependence of spin (magnetism) and heat. The underlying question of this project is the role of the thermal conductivity in spin caloritronics. Frequently, the thermal conductivity is not accessible experimentally due to mathematical or experimental constraints. This thesis aims at providing a tool and applications thereof in order to resolve this issue for important applications in spin caloritronics.

The electrical currents present in electric and thermoelectric experiments naturally are flows of electrons with statistically distributed spins which move in a common direction. It is now necessary to distinguish between spin polarized currents (electrical (charge) currents, in which all spins are aligned) and pure spin currents. Since in the latter case no charge is transported and only angular momentum is transfered (Fig. 1.2), these two current types give rise to different physics.

While the distinction between these types of spin and charge currents does not play a crucial role in this project, other research exploits experiments based on pure spin currents and collective spin-based phenomena, such as spin waves, in order to affect heat. A branch of common research topics concerns the spin analoga of the thermoelectric effects, in particular the spin Seebeck effect.

Spin polarized electric currents in a solid transport not only charge but also angular momentum and thereby possess the ability to transfer angular momentum to other subsystems of the material, such as the magnetic lattice. An extension of the classical Hall effect, the spin Hall effect, is crucial to most spin caloritronic experiments, as it has the ability to transform electrical into spin currents and vice versa (Bauer et al., 2012, Althammer et al., 2013). Generally, the electric current is perceived as a superposition of spin polarized currents with spin up and spin down (Bauer et al., 2012).

This description is useful for example in the description of the tunneling magnetothermal resistance (Fabian et al., 2004, Liebing et al., 2011). This phenomenon describes the influence of the charge carrier spin in a junction of a magnetic metal, a nonmagnetic insulator and a magnetic metal. If one spin polarization is suppressed by the magnetic alignment of the two metallic layers, that causes the inverse spin direction to be scattered predominantly, the electrical

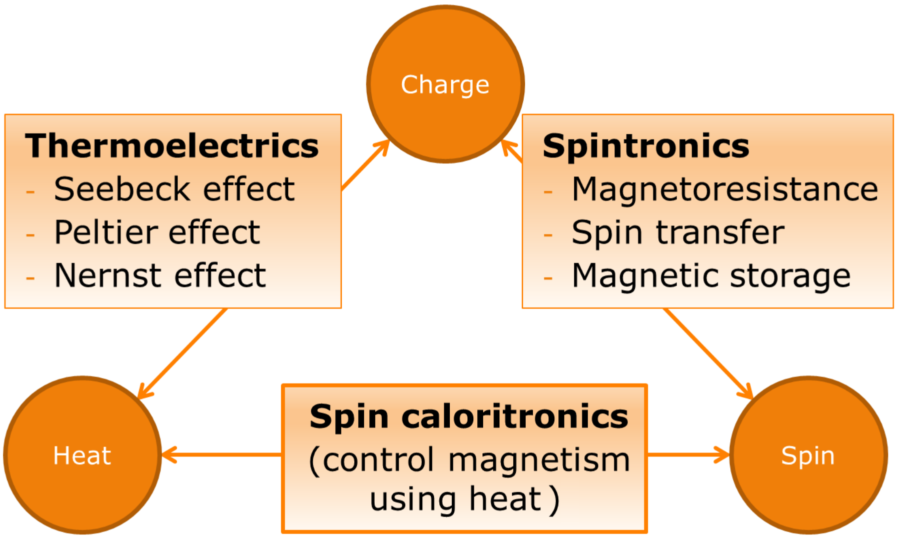

Figure 1.1.: Idea of spin caloritronics.

resistance of the system changes. A second example is that of the spin dependent Peltier effect, which describes the regular Peltier effect in a spin-polarized environment. By comparing both spin orientations in a Peltier device, it is possible to determine temperature differences and attribute these to the thermal conductance of the respective spin channel (Boona et al., 2014). Finally, collective phenomena such as spin waves (magnons) are a particularly interesting field, as these quasiparticles appear to be linked to most phenomena in spin caloritronics (Uchida et al., 2010, Schreier et al., 2013, Kehlberger et al., 2013, Agrawal et al., 2013, Ritzmann et al., 2014).

Common to all these experiments is the presence of a temperature gradient, so that the distribution of heat plays a crucial role. The distribution of heat within a specific material is primarily given by the thermal conductivity that in principle is a bulk property describing the efficiency of the transport of thermal energy. It is contributed to by two material specific components: electrons and lattice vibrations. With decreasing length scales of a system the number of accessible lattice vibrations decreases, so that in thin film research the term thermal conductivity looses its meaning. Therefore, in the context of thin films and in this project the (thickness dependent) thermal property is termed ‘thermal conductance’.

The thermal conductance in all experiments connected to this project has been measured by the 3ω method. The experimental idea of the 3ω method is based on a set of equations describing the heat resistance of a material. These equations cannot be solved analytically, so that a number of simplifying assumptions are made (section 3.1). As a result the thermal conductance perpendicular to the film plane can be determined at the expense of the in-plane thermal conductance parallel to the film plane. So far the full set of equations has not previously

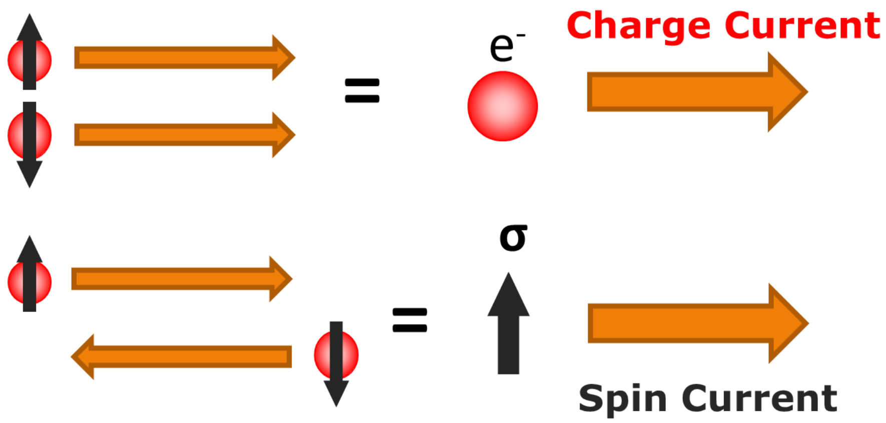

Figure 1.2.: Charge current with arbitrary spin orientation (top) and pure spin current (bottom). In the former case no angular momentum is transfered, whereas in the latter case no net charge is transported.

been applied successfully. Therefore, an algorithm that estimates the value of both the cross-plane and in-plane thermal conductance of a thin film based on the full equations has been developed (section 3.3).

Several areas of industrial and academic research require knowledge of the thermal properties of a system. This can include liquids, bulk solids and thin film systems and leads to different approaches concerning measurements of the cross-plane and the in-plane thermal conductance especially in the case of thin films. Most groups in this field studied the influence of a thermal gradient on the spin structure of a material. The original idea of the research on thermal conductance in spin caloritronics described in this thesis stems from a project based on the reciprocal question: How is thermal transport manipulated by a change in the spin configuration of a material?

Particularly in the material class of manganites a large effect of the spin state of the central manganese atoms on the electric conductance is known (the phenomenon is usually termed colossal magnetoresistance). In these materials the local spin structure, the conduction electrons and the lattice are strongly linked. Since a magnetic field is capable of changing the local spin structure, correspondingly an effect on the lattice is expected, as well as a subsequent effect on the thermal conductance. The contribution to the lattice (phonon) structure, however, proved to exceed the expectations by far. Research about the influence of a magnetic field on the thermal conductance perpendicular to the film plane is presented in chapter 4. A phenomenologically similar, but physically very different effect is studied in the film plane and results are described in chapter 5.

Even further, knowledge of the thermal properties of a system are fundamental in all branches of spin-caloritronics, especially since spin currents are generated by temperature gradients. In order to quantify the efficiency of the spin current generation by the temperature gradient, the heat flux needs to be measured by means of a noninvasive method. However, measurements of the thermal conductance within spintronic devices possess particular difficulty. Additional challenges emerge in anisotropic systems such as certain film/substrate combinations or superstructures. In particular, YIG ($Y_3Fe_5O_{12}$) is of interest in spin-caloritronics, as the material is a prototype of temperature driven pure spin currents and the spin Seebeck effect. Unfortunately, in previous experiments temperature gradients were calculated using the bulk thermal conductivity of YIG, even though thin films of several hundred nm thickness were used. In order to solve this caveat, Chapter 6 describes the application of this novel method to technologically relevant yttrium iron garnet films and for the first time presents temperature and thickness dependent data of the thin film thermal conductance of YIG.

CHAPTER 2

RELEVANT ELECTRIC AND THERMAL TRANSPORT PROCESSES

This chapter provides an overview over the theoretical framework within which the conducted research is located. It is divided into two sections: The first section reviews the theory of electric conduction in metals given by Drude and Sommerfeld and introduces to the Wiedemann-Franz law. The second section reviews the theory of heat conduction, thermal conductivity and the underlying processes. The chapter is based on Rebhan (2005), Tritt (2004), Kittel (2006) and Hunklinger (2007).

2.1. Electronic Transport and the Wiedemann-Franz Law

Theoretical understanding of electronic transport in metals met one of its first milestones in 1900, when Drude developed his theory of electronic conduction, which was able to reproduce Ohm's law and the Wiedemann-Franz law. However, failing to take into account the then unknown Pauli principle Drude's theory was unable to reproduce other quantities such as the specific heat of solids. The theory was improved by Sommerfeld who introduced electrons as particles behaving according to the Schrödinger equation and the Pauli principle.

Drude's theory assumed that electrons follow the classical ideal gas law, i.e. they are free particles moving at a thermal velocity and occasionally colliding with atomic nuclei. The theory relies only on two parameters, namely electron density and a mean relaxation time τ. Electrons of mass m then move at an effective drift velocity $\mathbf{v}_d$, which differs from the thermal velocity because of an external electric field $\mathbf{E}$. The stationary solution of the resulting differential equation

$$\frac{d\mathbf{v}_d}{dt} = -\frac{e}{m}\mathbf{E} - \frac{\mathbf{v}_d}{\tau}, \tag{2.1}$$

by coincidence, is of the same physical form as the correct result (Ohm's law). This is true even though all electrons within the material are assumed to be accelerated and deflected, which is incompatible with the Fermi-Dirac distribution, that takes into account only the electrons at the Fermi edge.

According to Drude, the probability $P(t)$ that an electron is undisturbed for the time t and collides within the following dt is given by

$$P(t)dt = \frac{e^{-t/\tau}}{\tau}dt, \tag{2.2}$$

from which the mean velocity of the electrons in an electrical field $\mathbf{E}$ can be calculated using the mean time between collisions $\bar{t}$ to be

$$\bar{\mathbf{v}}_d = -\frac{e\mathbf{E}}{m}\bar{t} = -\frac{e\mathbf{E}}{m}\int\limits_0^\infty t\frac{e^{-t/\tau}}{\tau}\,dt = -\frac{e\tau}{m}\mathbf{E}. \tag{2.3}$$

Combining this with the definition of the current density $\mathbf{J}_e = -ne\bar{\mathbf{v}}_d$ with n the electron density leads to Ohm's law

$$\mathbf{J}_e = \frac{ne^2\tau}{m}\mathbf{E} =: \sigma\mathbf{E}. \tag{2.4}$$

Furthermore, for $\mathbf{E} = 0$ kinetic theory calculates mean velocities from the energy equipartition theorem

$$\frac{1}{2}m\bar{v}_d^2 = \frac{3}{2}k_B T, \tag{2.5}$$

in which k_B is Boltzmann's constant and T the temperature. In a medium that is subject to a temperature gradient ∇T the corresponding heat flow $\mathbf{J}_Q$ is proportional to the number of particles crossing the cross-section A per time with a drift velocity $\mathbf{v}_d$, $n\mathbf{v}_d A$. Furthermore, the magnitude of this heat flow is proportional to the energy transported per particle c. As follows from symmetry and Eq. 2.5, the proportionality factor amounts to $\frac{1}{3}$, so that

$$\mathbf{J}_Q = \frac{1}{3}n\bar{v}_d^2 c\tau(-\nabla T). \tag{2.6}$$

Using the definition of the mean free path, $\lambda_e = \bar{v}_d\tau$, and that of the specific heat capacity, $C = nc$, Eq. 2.6 leads to an expression for heat currents $\mathbf{J}_Q$ generated by a temperature gradient ∇T as

$$\mathbf{J}_Q = \frac{1}{3}\lambda_e\bar{v}_d c_v(-\nabla T) =: -\kappa_e\nabla T, \tag{2.7}$$

where κ_e is the electronic thermal conductivity[1] and c_v is the electronic specific heat per unit volume. Drude's theory furthermore expresses the specific heat per unit volume in terms of the molar specific heat c_m as

$$c_v = c_m \frac{n}{N_A} = \frac{3}{2} N_A k_B \left(\frac{n}{N_A} \right) = \frac{3}{2} k_B n, \tag{2.8}$$

where N_A is the Avogadro number and k_B is Boltzmann's constant. Inserting this expression into Eq. 2.7 leads to

$$\kappa_e = \frac{1}{2} \lambda_e \bar{v_d} k_B n. \tag{2.9}$$

Division by the definition of the electrical conductivity from Eq. 2.4 and subsequent canceling finally leads to the Wiedemann-Franz law

$$\frac{\kappa_e}{\sigma} = \frac{3}{2} \left(\frac{k_B}{e} \right)^2 T, \tag{2.10}$$

which, including the definition of all constants to the Lorenz number L_0, is equivalent to the formulation in terms of electrical resistivity $\rho = \sigma^{-1}$

$$\kappa_e \rho = L_0 T. \tag{2.11}$$

It is noteworthy that the value of L_0 is only smaller than expected from experiments by a factor of approximately two. This deviation originates from two conceptual mistakes, the first being the calculation of electronic specific heat from classical theory, which overestimates the electronic contribution, and the second arising from the velocity distribution not following Maxwell-Boltzmann statistics, but rather a small region of the Fermi distribution around the Fermi energy. Sommerfeld's theory improves Drude's model and takes into account the Schrödinger equation and the Pauli principle. Therefore, treating electrons as Fermions and accounting for the Fermi-Dirac distribution permits the calculation of the 'true' value of the Lorenz number to

$$L_0 = \frac{\pi^2}{3} \left(\frac{k_B}{e} \right)^2 = 2.44 \cdot 10^{-8} \frac{\mathrm{V}^2}{\mathrm{K}^2}, \tag{2.12}$$

which differs from the trivial value of Eq. 2.10 by $2\pi^2/9 \approx 2.2$.

As mentioned above, quantum mechanical treatment is essential for a correct approach to electronic transport theory. Following the electron's fermionic nature, theoretical formulations of electron transport need to obey the Pauli principle, which is ensured by the Fermi-Dirac distribution

---

[1] Thermal conductivity is defined in Eq. 2.44 in section 2.2.

$$f(E,T) = \frac{1}{e^{(E-\mu)/(k_B T)} + 1}\,. \tag{2.13}$$

Here μ is the electrochemical potential, which usually is referred to as the Fermi energy E_F at finite temperature. While at $T = 0$ the Fermi-Dirac distribution is a step function, it is smeared out over a region of approximately $4k_BT$ at finite temperatures. Because of this, electrons within the broadened Fermi edge have access to empty states, thus allowing them to interact with other sources of energy such as thermal gradients or electrical fields.

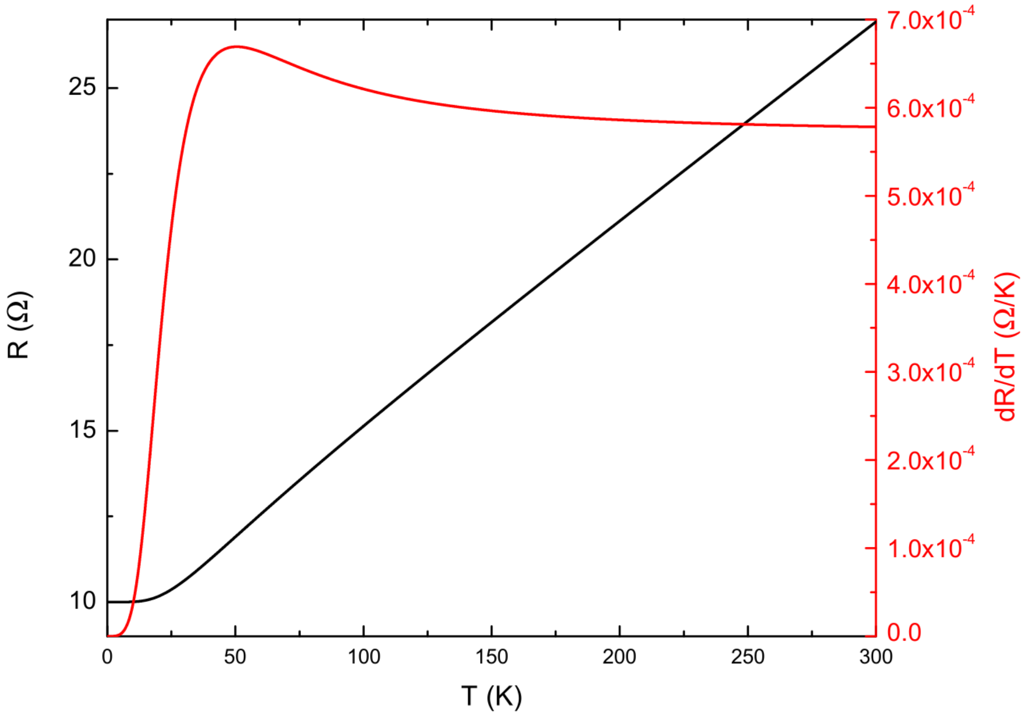

Figure 2.1.: The resistance (black) and the numerical temperature derivative of the resistance (red) as a function of temperature of a metal with a Debye temperature of 140 K, a constant $A = 32$ and a saturation resistance of 10 Ω.

Any accurate description of electron transport requires a value of electron density n, which can be calculated from

$$n = \int_0^\infty \mathcal{D}(E) f(E,T)\, dE \tag{2.14}$$

assuming knowledge of the energy dependent density of states $\mathcal{D}(E)$. From this expression the gain in internal energy of the electron system at finite energy can be calculated, which, after differentiation by the temperature, leads to an expression for the heat capacity c_v as

$$c_v = \int_0^\infty (E - E_F)\mathcal{D}(E)\frac{\partial f(E,T)}{\partial T}\, dE. \tag{2.15}$$

Assuming that the density of states changes only slowly with energy, integration yields

$$c_v = \frac{\pi^2}{3} k_B^2 T \mathcal{D}(E_F). \tag{2.16}$$

For the case of a free electron gas the density of states has a $\sqrt{E}$ dependence, so that with the definition of the Fermi temperature as $T_F = E_F/k_B$ the heat capacity of the electron system can be expressed as

$$c_v = \frac{\pi^2}{2} n k_B \frac{T}{T_F} =: \gamma T. \tag{2.17}$$

Comparing this outcome to Eq. 2.8 illustrates the deviation between the classical and the quantum treatment, which is in particular given by the fraction $\frac{T}{T_F}$ relating the temperature to the Fermi temperature. If this result is now multiplied by the molar volume $\frac{ZN_A}{n}$, one finally arrives at the heat capacity per unit volume

$$C_V = \frac{\pi^2}{2} Z k_B N_A \frac{T}{T_F}. \tag{2.18}$$

In Eq. 2.17, γ is usually called Sommerfeld's constant. It is worthwhile to point out that the specific heat capacity of electrons is linear in temperature. The theory of thermal conductivity derived in section 2.2 will show that the electronic contribution to the total specific heat capacity usually is much smaller than the lattice contribution, which is proportional to T^3.

The description of electronic conduction is modified in thin film systems and at low temperatures, when the dominant scattering mechanisms contributing to the process change. The electrical resistivity finally depends both on the sample's thickness (Fuchs, 1938, Sondheimer, 2001) and the ambient temperature. In particular, Bloch (1930) demonstrated that due to defect scattering the electrical resistivity saturates at low temperatures and approaches the known linear regime towards high temperatures. The description of the intermediate temperature regime was refined by Grüneisen (1933). The resulting equation,

$$R(T) = R_0 + A \left(\frac{T}{\Theta_D} \right)^5 \int\limits_0^{\frac{\Theta_D}{T}} \frac{e^x x^5}{(e^x - 1)^2} \, dx, \tag{2.19}$$

describes the resistivity of a metal as a function of temperature (Fig. 2.1). R_0 is the saturation value given by defect scattering at low temperature, A is a constant, Θ_D is the Debye temperature defined in the context of Eq. 2.38 and the integration is carried out up to a value of $\frac{\Theta_D}{T}$.

2.2. Thermal Conductance

Thermal conductivity is a material specific parameter describing the ease at which heat flows through a substance. Its origin lies in the spectrum of excited lattice vibrations (phonons), to which the electron subsystem contributes additionally in the case of electrical conductors and semiconductors. Phonon physics will be introduced in more detail in the course of this section following the discussions of Hunklinger (2007, p. 178f.) and Tritt (2004, Sec. 3). One piece of basic terminology, however, requires immediate attention. Phonons manifest themselves as vibrational modes with a wavelength spectrum λ_i^{Ph} within the lattice, which implies that especially in thin film systems long-wavelength phonons cannot contribute to the thermal conductivity. The term thermal conductivity thus only is valid in bulk material and thin film samples possess a particularly thickness dependent thermal conductance, which will in the following chapters specifically be used to correct for the above described misconception if necessary. This section introduces the theory of thermal conductivity as a bulk parameter. The Callaway model (Callaway, 1959), which takes additional processes and the sample thickness dependence into account, is introduced at the end of the section.

2.2.1. Lattice Vibrations

In electrical insulators heat is transported by lattice vibrations and the electronic contribution to the thermal conductivity, which was introduced in the derivation of the Wiedemann-Franz law, Eq. 2.11, is zero. Lattice vibrations are described as quasiparticles termed phonons. The following discussion of basic phonon properties assumes a crystal with a two-atomic unit cell (atom types A and B) and a lattice constant of a. Furthermore, these atoms form two one-dimensional linked chains with other atoms of the same kind (atoms of type A in the one and type B in the other chain). If it is finally assumed, that all inter-atomic forces decrease rapidly with increasing radius, only the next neighbors need to be considered. Assume that atoms of type A are displaced by a length x_A and those of type B by x_B. Forces between atoms in layer $s \in \mathbb{N}$ on those in the neighboring layer $s-1$ are of the type

$$F_1 = \mathcal{C}(x_{B,s} + x_{B,s-1} - 2x_{A,s}) = M_1 \frac{d^2 x_{A,s}}{dt^2} \tag{2.20}$$

$$F_2 = \mathcal{C}(x_{A,s} + x_{A,s-1} - 2x_{B,s}) = M_2 \frac{d^2 x_{B,s}}{dt^2}. \tag{2.21}$$

These equations are solved by plane waves of the type

$$x_{A,s} = U e^{-i(\omega t - qsa)} \tag{2.22}$$

$$x_{B,s} = V e^{-i(\omega t - qsa)}. \tag{2.23}$$

Inserting the solutions into the respective differential equation leads to

$$(2C - \omega^2 M_1)U - C(1 + e^{-iqa})V = 0 \tag{2.24}$$
$$(2C - \omega^2 M_2)V - C(1 + e^{-iqa})U = 0\,, \tag{2.25}$$

of which the non-trivial solutions are

$$\omega^2_{a,o} = C\left(\frac{1}{M_1} + \frac{1}{M2}\right) \mp C\sqrt{\left(\frac{1}{M_1} + \frac{1}{M2}\right)^2 - \frac{4}{M_1 M_2}\sin^2\left(\frac{qa}{2}\right)}. \tag{2.26}$$

The indices a and o abbreviate 'acoustic' and 'optical', respectively, and correspond to the negative and positive sign of the square root. The acoustic branch corresponds to the behavior of a chain with mono-atomic base. The reason for the existence of two different branches lies within the phase difference between the oscillations of the two chains. The ratio of x_A to x_B has the approximate form

$$\frac{x_A}{x_B} \approx \frac{2C}{2C - \omega^2 M_1}. \tag{2.27}$$

Phonons in the acoustic branch oscillate in phase (hence the name), as is seen if ω is approximated to zero, which implies $x_A \approx x_B$. In the optical case there is a phase difference of $180°$, as the limit of $q \to 0$ leads to $\omega^2 = 2C/\mu$ (μ is the reduced mass $\mu^{-1} = M_1^{-1} + M_2^{-1}$) and therefore $x_A/x_B = -M_2/M_1$.

2.2.2. Debye's T^3 Law

Transport processes and scattering processes within are commonly described by the Boltzmann equation, which characterizes the distribution function f as a function of the position $\mathbf{r}$, the velocity $\mathbf{v}$ and time t as $f(\mathbf{r}, \mathbf{v}; t)$. It originally assumes a gas of indistinguishable non-interacting particles of mass m in an external force field $\mathbf{F}$, so that the equations of motion are $\dot{\mathbf{r}} = \mathbf{v}$ and $\dot{\mathbf{v}} = \frac{\mathbf{F}(\mathbf{r})}{m}$. For small time differences $\Delta t = t' - t$ the distribution function can be expanded to

$$f'(\mathbf{r}', \mathbf{v}'; t') = f(\mathbf{r} + \mathbf{v}\Delta t, \mathbf{v} + \frac{\mathbf{F}}{m}\Delta t; t + \Delta t) \tag{2.28}$$
$$= f(\mathbf{r}, \mathbf{v}; t) + \left(\frac{\partial f}{\partial \mathbf{r}}\mathbf{v} + \frac{\partial f}{\partial \mathbf{v}}\frac{\mathbf{F}}{m} + \frac{\partial f}{\partial t}\right)\Delta t. \tag{2.29}$$

As particles within a phase space volume remain within this phase space volume due to their non-interacting nature, the expectation value of the number of particles in the phase space volume remains constant. Further following the justification of Rebhan (2005, section 30.3), that exploits that by Liouville's theorem the occupied phase space volume is constant with time, also the distribution function remains unchanged, so that $f' = f$ (any change in f would result in a violation of the second law of thermodynamics[2]). Inserting this into the above equation leads to the colisionless Boltzmann equation

$$\frac{df}{dt} = \frac{\partial f}{\partial t} + \mathbf{v}\frac{\partial f}{\partial \mathbf{r}} + \frac{\mathbf{F}}{m}\frac{\partial f}{\partial \mathbf{v}} = 0. \tag{2.30}$$

Should the system be allowed to deviate from equilibrium, an interaction (collision) term needs to be included, so that $\frac{df}{dt} = \frac{df}{dt}|_{\mathrm{coll}}$. Assuming a mean time between two collisions, τ, that is independent of **r**, **v** and t, and denoting the equilibrium distribution function f^0, the collisional Boltzmann equation in relaxation time approximation is formulated as

$$\frac{\partial f}{\partial t} + \mathbf{v}\frac{\partial f}{\partial \mathbf{r}} + \frac{\mathbf{F}}{m}\frac{\partial f}{\partial \mathbf{v}} = -\frac{f - f^0}{\tau}. \tag{2.31}$$

The above will now be applied to thermal transport. Phonons are bosons and as such obey the Bose-Einstein distribution function describing the number of phonons $N^0_{\mathbf{q}}$ with wave vector **k** as

$$N^0_{\mathbf{k}} = \frac{1}{e^{\hbar\omega_{\mathbf{k}}/(k_B T)} - 1}. \tag{2.32}$$

Boltzmann statistics assumes scattering processes to restore thermal equilibrium $N^0_{\mathbf{k}}$ from a deviation $N_{\mathbf{k}}$, so that in an application of Eq. 2.31

$$\frac{N_{\mathbf{k}} - N^0_{\mathbf{k}}}{\tau_k} = -(\mathbf{v}_g \cdot \nabla T)\frac{\partial N^0_{\mathbf{k}}}{\partial T}, \tag{2.33}$$

where $\mathbf{v}_g$ is the phononic group velocity and τ_k is the relaxation time required to approach thermal equilibrium (Tritt, 2004, Sec. 3). Because the heat flux caused by a phonon mode is the product of the average energy and the group velocity, the total heat flux carried by phonons can be expressed as the sum over the contribution of the modes **k**

$$\mathbf{Q} = \sum_{\mathbf{k}} N_{\mathbf{k}}\hbar\omega_{\mathbf{k}}\mathbf{v}_{\mathbf{k}}. \tag{2.34}$$

Inserting Eq. 2.33 into Eq. 2.34 and defining θ as the angle between $\mathbf{v}_{\mathbf{k}}$ and ∇T results in an expression for **Q**

$$\mathbf{Q} = \sum_{\mathbf{k}} \hbar\omega_{\mathbf{k}} v^2_{\mathbf{k}} \tau_{\mathbf{k}} \langle\cos^2\theta\rangle \frac{\partial N^0_{\mathbf{k}}}{\partial T}\nabla T = -\frac{1}{3}\sum_{\mathbf{k}} \hbar\omega_{\mathbf{k}} v^2_{\mathbf{k}} \tau_{\mathbf{k}} \frac{\partial N^0_{\mathbf{k}}}{\partial T}\nabla T \tag{2.35}$$

and subsequently, for the lattice thermal conductivity, to an expression obtained from the definition of the thermal conductivity,

---

[2] Mathematically speaking, for a phase space volume of $\Delta\Omega$ Liouville's theorem can be formulated as $\frac{d}{dt}\Delta\Omega = 0$. Assume it was not valid, that is, $\frac{d}{dt}\Delta\Omega \neq 0$. In equilibrium, $\frac{d\rho}{dt} = 0$, so that $\frac{d(\rho\ln\rho\Delta\Omega))}{dt} = \Delta\Omega\frac{d(\rho\ln\rho)}{dt} + \rho\ln\rho\frac{d\Delta\Omega}{dt}$. The derivative in the first term is zero in equilibrium, which leads to $\frac{d(\rho\ln\rho\Delta\Omega))}{dt} = \rho\ln\rho\frac{d\Delta\Omega}{dt} \neq 0$. Therefore, also the integral $\int d\Omega\,\rho\ln\rho \neq 0$, so that for entropy, $S = -k_B\int d\Omega\rho\ln\rho$, the total time derivative is negative. This, however, is a violation of the second law of thermodynamics.

$$\kappa_{\mathrm{Ph}} := -\frac{\mathbf{Q}}{\nabla T} = \frac{1}{3}\sum_{\mathbf{k}} \hbar\omega_{\mathbf{k}} v_g^2 \tau_{\mathbf{k}} \frac{\partial N_{\mathbf{k}}^0}{\partial T}\,. \tag{2.36}$$

The factor $\frac{1}{3}$ originates from the assumption of isotropic heat transport. For simplicity it is now assumed that all phonon branches have identical velocity. The sum in Eq. 2.36 is then transfered into an integral, in which the Debye approximation of a cutoff of a linear dispersion relation is included and the density of states is quadratic. Using Eq. 2.32 leads to

$$\kappa_{\mathrm{Ph}} = \frac{1}{3}\int \hbar\omega_{\mathbf{k}} v_g^2 \tau_k \frac{\partial N_{\mathbf{k}}^0}{\partial T} f(q)\,d\mathbf{k} = \frac{1}{2\pi^2 v_g}\int_0^{\omega_D} \hbar\omega^3 \tau_k(\omega) \frac{\hbar\omega/(k_B T^2) e^{\hbar\omega/(k_B T)}}{\left[e^{\hbar\omega/(k_B T)} - 1\right]^2}\,d\omega, \tag{2.37}$$

where ω_D is the Debye frequency defined by the total number of phonon modes

$$3N = \int_0^{\omega_D} f(\omega)\,d\omega. \tag{2.38}$$

Additionally defining a dimensionless energy parameter $x = \frac{\hbar\omega}{k_B T}$ and the Debye temperature Θ_D as the temperature corresponding to the Debye frequency $\hbar\omega_D = k_B\Theta_D$ simplifies Eq. 2.37 to

$$\kappa_{\mathrm{Ph}} = \frac{k_B}{2\pi^2 v_g}\left(\frac{k_B}{\hbar}\right)^3 T^3 \int_0^{\Theta_D/T} \tau_k(x)\frac{x^4 e^x}{(e^x-1)^2}\,dx. \tag{2.39}$$

For the lattice specific heat capacity then follows that

$$C_{V,\mathrm{Ph}} = \frac{3k_B}{2\pi^2 v_g^3}\left(\frac{k_B}{\hbar}\right)^3 T^3 \int_0^{\Theta_D/T} \frac{x^4 e^x}{(e^x-1)^2}\,dx. \tag{2.40}$$

This equation can conveniently be evaluated in the high-temperature and the low-temperature limit as follows. In the low-temperature limit $x \to \infty$ and the integral is solvable analytically to

$$\int_0^{\infty} \frac{x^4 e^x}{(e^x-1)^2}\,dx = \frac{4\pi^4}{15}, \tag{2.41}$$

so that

$$C_{V,\mathrm{Ph}} \propto \left(\frac{T}{\Theta_D}\right)^3, \tag{2.42}$$

which is the typical Debye T^3 law. The high-temperature limit provides $x \to 0$, so that the integral can be simplified to

$$\int_0^{\Theta_D/T} \frac{x^4 e^x}{(e^x-1)^2}\,dx \approx \int_0^{\Theta_D/T} \frac{x^4}{(1+x-1)^2}\,dx = \int_0^{\Theta_D/T} x^2\,dx = \frac{1}{3}\left(\frac{\Theta_D}{T}\right)^3. \tag{2.43}$$

Inserting this into Eq. 2.40 results in the Dulong-Petit law $C_{V,\mathrm{Ph}} = 3R$.

2.2.3. Scattering Processes

Thermal conductivity is a measure for the efficiency of heat transport through a material that is, as in the electric case, limited by scattering. Heat can be transported by means of electrons or excitations of the material such as lattice excitations (phonons), spin waves or other forms of excitations. The total thermal conductivity can then be expressed as the sum of all contributing thermal conductivities. In general, the dominant contributions are electrons and phonons (naturally, electrons do not play a role in electrical insulators); all other carriers of thermal energy such as magnons will be neglected in the following discussion. A result for the electronic thermal conductivity has been found previously as the Wiedemann-Franz law Eq. 2.11 so that, therefore, this part of the section discussing thermal conductivity only considers phononic processes.

As in Eq. 2.36, thermal conductivity is defined as

$$\kappa = -\frac{Q}{\nabla T}, \tag{2.44}$$

where T is the temperature and Q is the heat flux perpendicular to a unit cross section. Following Debye's derivation, phonons can be approximated as a classical gas, so that kinetic theory yields an expression for the thermal conductivity, which is for consistency repeated from Eq. 2.7

$$\kappa = \frac{1}{3} C_{V,\mathrm{Ph}} v \lambda_{\mathrm{Ph}}. \tag{2.45}$$

Thermal resistance effectively is the consequence of phonon scattering with defects in the crystal structure and of phonons with each other. Even though ideally phonons do not couple to each other, real crystals include anharmonic effects such as three-phonon processes. These processes conserve energy and quasi-momentum up to the addition of a reciprocal lattice vector and are the reason for thermal resistance:

$$\hbar\omega_1 \pm \hbar\omega_2 = \hbar\omega_3 \tag{2.46}$$

$$\hbar\mathbf{k}_1 \pm \hbar\mathbf{k}_2 = \hbar\mathbf{k}_3 + \hbar\mathbf{G}. \tag{2.47}$$

Depending on the sign a phonon is created or annihilated; depending on the involvement of a

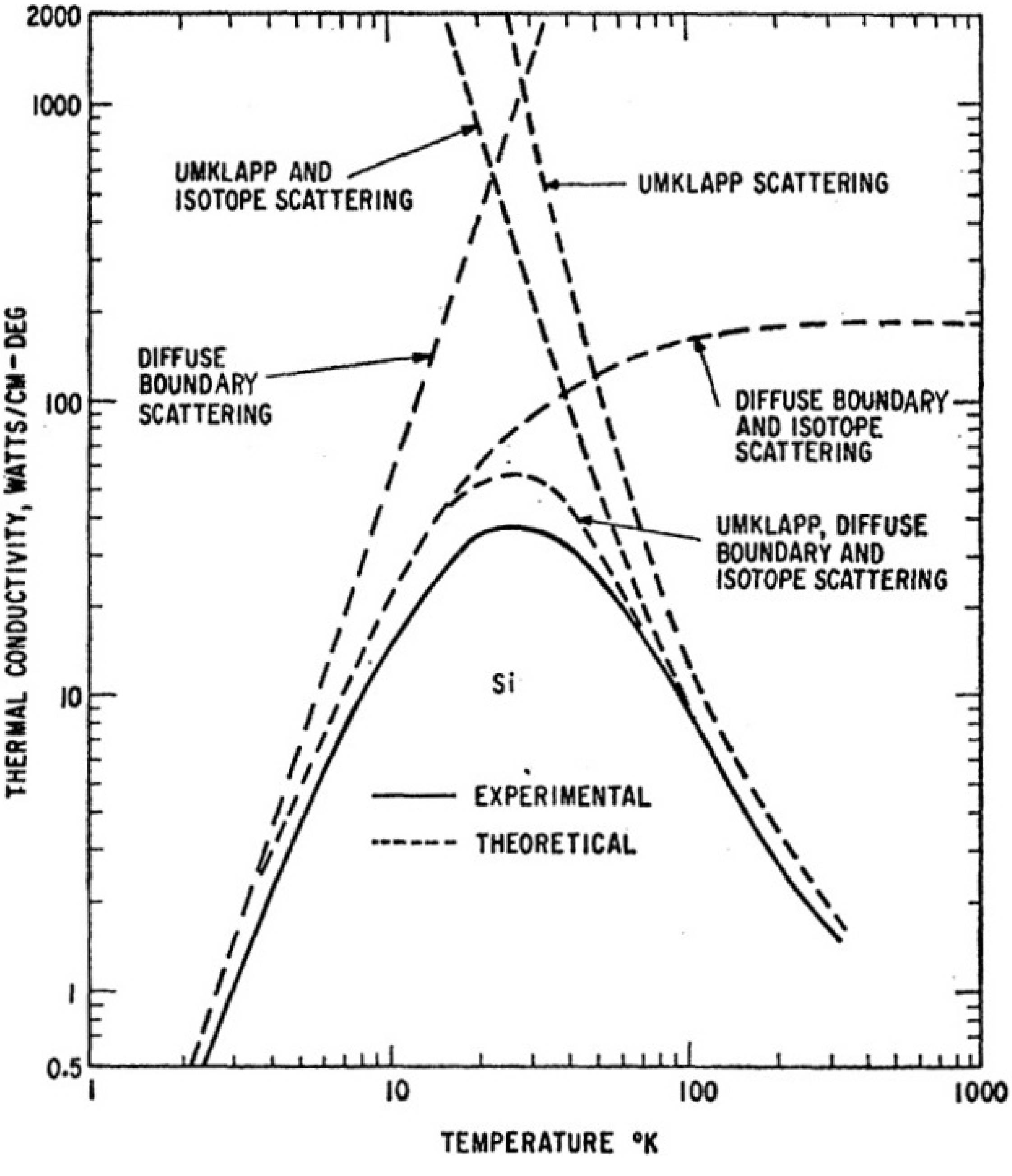

Figure 2.2.: Influence of Normal, Umklapp, boundary and defect scattering on the thermal conductivity of Si. Reprinted figure with permission from Glassbrenner and Slack (1964), copyright 1964 by the American Physical Society.

reciprocal lattice vector the scattering processes are termed Umklapp (U) process (including reciprocal lattice vector) or Normal (N) process, as the resulting wave vector lies outside of or within the first Brillouin zone, respectively. In normal processes the sum of all quasi-momenta is conserved, so that such processes only contribute to the thermal conductivity by interaction with Umklapp processes. To permit a finite thermal resistance, conservation of the sum of all quasi-momenta has to be violated. This is the case, if the resulting wave vector does not lie within the first Brillouin zone. Key to such Umklapp processes is that the group velocity of the created phonon has an opposite sign to that of the incoming phonons (hence the name). At high temperatures, Umklapp processes dominate, because the majority of the phonons have frequencies comparable to the Debye frequency, and their wave vectors are close to the boundaries of the first Brillouin zone.

Although the Debye model relies on very simple assumptions, it displays remarkable success describing the heat capacity and the thermal conductivity of materials with different unit cells (the simple Al_2O_3 required in the sample stack is represented as well as the much more complex $Y_3Fe_5O_{12}$ with 80 atoms in the unit cell (Cherepanov et al., 1993)). To qualitatively understand the temperature dependence of the thermal conductivity of an insulator, the following paragraph presents a simplified discussion of a simple monoatomic material on the basis of Eq. 2.45. At very high temperatures compared to the Debye temperature the thermal conductivity can be calculated from an estimation of the mean free path to follow

$$\kappa \propto \frac{1}{T}. \tag{2.48}$$

At intermediate temperatures, $T \leq \Theta_D$, the number of phonons contributing to Umklapp processes is strongly temperature dependent. Their energy needs to be at least $\frac{\hbar\omega_D}{2}$ for the created phonon to lie outside the first Brillouin zone. The probability for this to happen follows from Bose-Einstein statistics to be proportional to $e^{\Theta_D/(2T)}$. Because the mean free path and the specific heat capacity do not strongly depend on the temperature in this regime, the thermal conductivity can be approximated by

$$\kappa \propto e^{\Theta_D/(2T)}. \tag{2.49}$$

At low temperatures, Umklapp processes are disfavored and phonon scattering occurs entirely within the first Brillouin zone. The mechanism limiting the thermal conductivity is phonon scattering at the sample surface. Assuming a mean free path of the order of the sample size, Eq. 2.45 leads to

$$\kappa \propto T^3 d. \tag{2.50}$$

The thermal conductivity therefore does not only depend strongly on the temperature, but also

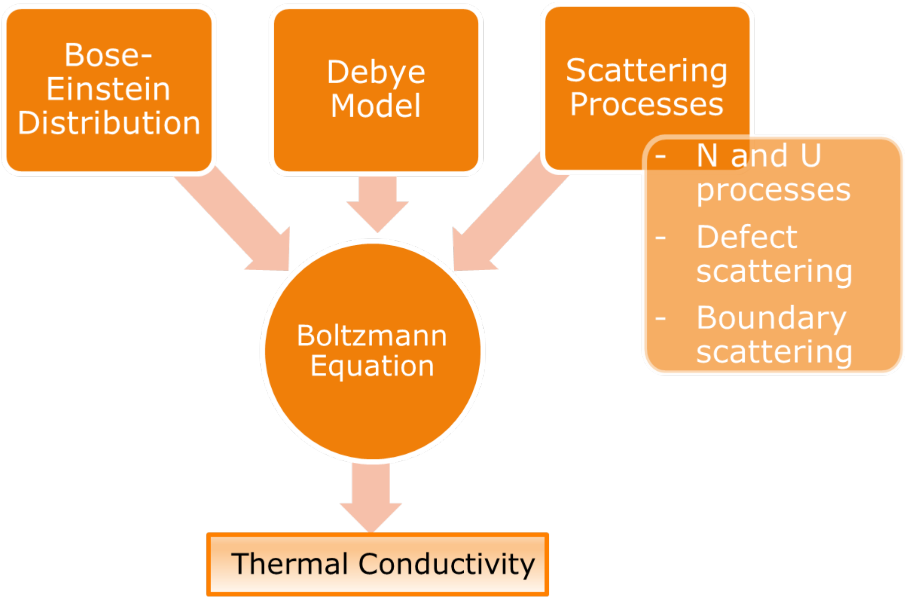

Figure 2.3.: Constituents of the Callaway model of thermal conductivity. The bosonic nature of phonons, the Debye approximation and a parametrization of the scattering processes in terms of relaxation times are inserted into the Boltzmann equation, which is solved to give a temperature and sample thickness dependent thermal conductivity.

on the geometry of the sample and the morphology of the surface. This finite size effect leads to a prominent maximum in the thermal conductivity, below which the thermal conductivity decreases with T^3 towards $T = 0$. Finally, phonons can be scattered at defects (e.g. different isotopes of the materials or point defects). The effect of defect scattering is most prominent in the vicinity of the maximum of the thermal conductivity. The influences of Normal, Umklapp, boundary and defect scattering are displayed in Fig. 2.2. In particular, the influence of scattering at isotopes plays an important role at high temperature, even though the principal driving force is Umklapp scattering. At low temperature the prominent boundary scattering reduces the thermal conductivity.

Furthermore, the influence of Umklapp and Normal processes as well as defect and boundary scattering needs to be formalized mathematically. The last part of this section therefore covers the model by Callaway (1959) (Fig. 2.3). This model is based on the three main constituents of phonon physics introduced above: The bosonic nature formalized by the Bose-Einstein distribution Eq. 2.32, the Debye model leading to Eq. 2.39, and scattering processes, which are described by the Boltzmann equation, Eq. 2.33. Scattering processes are divided into three classes: phonon-phonon scattering (U and N processes), scattering of phonons on defects and scattering of phonons at the sample boundaries. Higher order scattering processes are neglected in this model. The Boltzmann equation is then solved in the relaxation time approximation in which all scattering processes are attributed specific relaxation times τ. In particular, normal processes are given a phenomenological relaxation time of $\tau_N^{-1} = B\omega^2 T^3$, Umklapp processes that of $\tau_U^{-1} = \omega^2 T^3 \exp\left(\Theta_D/(CT)\right)$, point defect scattering that of $\tau_d^{-1} = A\omega^4$ and boundary scattering that of $\tau_b^{-1} = v_s/d$. In these equations ω is a phonon frequency, A, B and C are constants, v_s is the (temperature dependent) sound velocity, d is the sample thickness and Θ_D is the Debye temperature. The Callaway model is then capable of describing the temperature and thickness dependent thermal conductivity of any material, originally by a reformulated version of Eq. 2.39

$$\kappa(T) = \frac{k_B}{2\pi^2 v_s} \int\limits_0^{\omega_D} \frac{1}{\tau} \left(\frac{\hbar\omega}{k_B T}\right)^2 \frac{e^{\frac{\hbar\omega}{k_B T}} \omega^2}{\left(e^{\frac{\hbar\omega}{k_B T}} - 1\right)^2} d\omega \,, \tag{2.51}$$

where the relaxation time τ is given by the reciprocal sum of all component relaxation times and the integral is carried out for phonon frequencies up to the Debye frequency defined in Eq. 2.38.

In addition, in a ferromagnet it is necessary to take into account magnon phonon damping. The dispersion relation of magnons, quantized spin waves, can in principle be formulated by the same approach as in the derivation of Eq. 2.26. Following Kittel (2006, p. 364ff.), the cosine-shaped dispersion relation[3] is approximated by $\omega \propto k^2$. In particular, Gilbert damping arises from the phenomenological Landau-Lifschitz-Gilbert equation as a damping constant originating from the interaction of a spin that is misaligned with respect to the net magnetization. This damping constant α_G causes a phenomenological temperature dependent relaxation time (Schreier et al., 2013)

$$\tau_G = \frac{\hbar}{\alpha_G k_B T} \,. \tag{2.52}$$

Increasing the damping parameter effectively causes a suppression of the thermal conductivity by a decreased relaxation time τ_G (Fig. 2.4). However, as Gilbert damping is phenomenological, it implicitly considers arbitrary relaxation effects such as spin reorientation in moving domain walls, random size and orientation of crystal grains, crystal defects, impurities or strain (Gilbert, 2004). In a perfect ferromagnet the cause of relaxation would be the above mentioned spin magnetization interaction. As scattering of magnons and phonons could lead to additional thermal resistance, it can be critical for the numerical evaluation of the thermal conductivity data.

---

[3] In the phonon case, Eq. 2.21, the force between two atoms is linear in the defining parameter, x. In the magnon case, however, the exchange interaction depends on the product of the spins, so that for N spins the force between the nearest neighbors U is given by $U = -2J\sum_{p=1}^{N-1} \mathbf{S}_p \cdot \mathbf{S}_{p+1}$. Therefore, the equations of motion result in a $\sin q$ and $\cos q$ dependence of ω, which are approximated by a linear and parabolic dispersion relation, respectively.

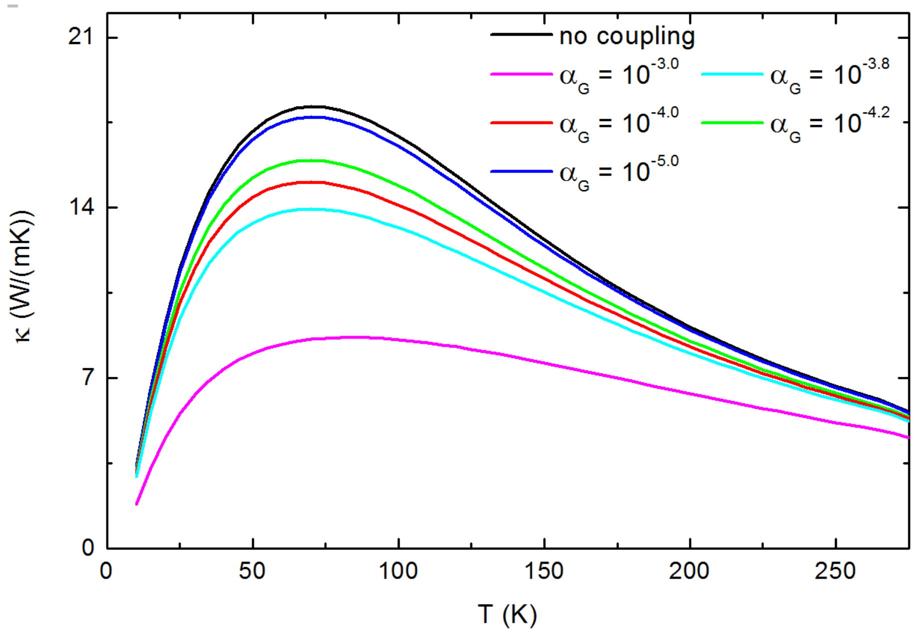

Figure 2.4.: Influence of Gilbert damping on the thermal conductivity of a hypothetical magnetic insulator. The suppressing effect of increased magnon phonon scattering on the thermal conductivity is clearly visible in comparison with the model, in which the damping term is not included (no coupling). Values around $\alpha_G = 10^{-4}$ are physical for $Y_3Fe_5O_{12}$.

If impurities (defects) are introduced, not only does phonon-defect scattering occur (as handled by τ_d), but also magnon-defect and thereby magnon-magnon scattering events. In particular magnon-phonon scattering could then be caused by magnon-defect scattering, so that effectively magnon-defect and phonon-defect scattering are linked by magnon-phonon scattering. It is only possible to quantitatively evaluate this effect, if the number of contributing processes to τ_G was known and all relaxation times were equal. Thus, defect scattering by phonons and magnons would be introduced in a duplicate fashion, and the introduction of a Gilbert relaxation time could lead to an overestimation of the defect contribution to the thermal conductivity. While Schreier et al. (2013) used a wave vector independent description of the Gilbert damping, Hankiewicz et al. (2008) developed a model of α as a function of the wave vector of the magnetic excitation and demonstrated that electron-electron and electron-impurity interactions can give rise to a k^2 contribution to Gilbert damping. However, the Gilbert theory defines magnetization as 'the expectation value of the magnetic moment per unit volume due to the spins and orbital motion of unpaired electrons averaged over a few lattice cells' (Gilbert, 2004). In a magnetic insulator as will be studied in chapter 6 no electron-electron interactions exist, but only a contribution originating from defect interaction. The Gilbert theory relies on the description of the magnetization **M** in terms of a spin **S** and the gyromagnetic ratio γ as

$$\mathbf{M} = \gamma \mathbf{S} \tag{2.53}$$

and furthermore converts any discrete description of local magnetization into a continuous field equation. At no point of the argument presented it is necessary to assume that the magnetism actually stems from electronic imbalance, but a generalization to arbitrary atomic spins is possible so that the Gilbert model is applicable also in magnetic insulators[4]. In that case, i.e. in the case of spin-defect interactions and neglected spin-spin interactions, Hankiewicz et al. (2008) arrive at a linear relation between $\log \alpha$ and $\log \frac{1}{\tau_d}$. Therefore, it can be useful to introduce Gilbert relaxation into the Callaway model as an additional (phenomenological) term to the defect scattering relaxation time.

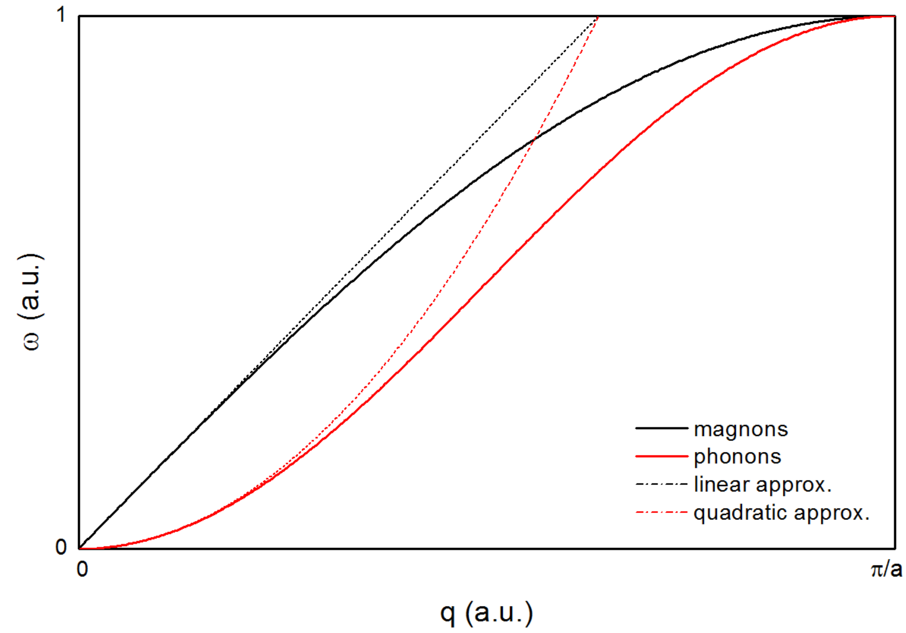

Figure 2.5.: Phonon (black solid line) and magnon (red solid line) dispersion relations normalized to unity at π/a and the respective fits to leading order (dotted lines).

The sine and cosine shaped dispersion relations of phonons and magnons, respectively, are depicted in Fig. 2.5. Particularly noteworthy is the fact that for small q the phonon energy by far exceeds the magnon energy, which leads to the conclusion that magnon phonon interactions are unlikely to cause phonon Umklapp scattering, that is, thermal resistance. In addition, caution is necessary, as in the new description the Gilbert damping is a temperature dependent quantity, because the defect scattering relaxation time is temperature dependent. As this discussion does not allow a reliable quantitative evaluation of the data taken, in agreement to the negligible magnonic contribution to the thermal conductivity measured in chapter 6, the magnon phonon relaxation times will not be included into the Callaway model for use in this thesis.

---

[4] In the process of converting the discrete equations into field equations Gilbert (2004) 'assumes a model for which the spins are in a lattice array and that electrons with unpaired spins can be assigned to localized orbitals in the lattice cells'. This assumption is a strong argument for the validity of the transition to arbitrary atomic spins.

CHAPTER 3

BAYESIAN DATA EVALUATION SCHEME FOR THE 3ω METHOD

The thermal conductivity of a material, κ, is a bulk property describing the efficiency of the transport of thermal energy through a material. While in the previous chapter the theoretical foundations of thermal transport were introduced, this chapter considers experimental techniques. Measurements of the thermal conductance in particular possess the special difficulty that heat flux within a material needs to be measured by means of a noninvasive method. In principle, this is possible by attaching a temperature sensor to two sides of a material sample and measuring the temperature increase upon heating one of the sides. However, challenges emerge in thin film systems, polycrystalline materials with inhomogeneous grain structure or anisotropic systems such as superlattices. This leads to different approaches concerning measurements of the cross-plane and the in-plane thermal conductance. Frequently applied methods for thin films can be classified into electrical, optical and hybrid techniques as is expanded on below. The only available electrical measurement technique for cross-plane thermal conductance is the 3ω method (Tritt, 2004), while there is an abundance of available methods to measure the thermal conductivity using other techniques:

- **Time domain thermoreflectance** studies the temperature dependent reflectivity of the sample surface. If the surface is illuminated by a laser pulse of known power and intensity, the time dependent temperature decay on the sample surface is a measure of the amount of energy transported away. In a pump-and-probe experiment a second laser measures the sample reflectivity as a function of the time, that can then be converted into the thermal conductivity, since the refractive index is temperature dependent. In order to prevent substrate induced influences on the measurement the laser pulse is required to be shorter than 10^{-7} s. Generally, lasers with repetition frequencies of around 100 MHz are used to achieve sufficient sampling rates. (Paddock and Eesley, 1986, Capinski et al.,

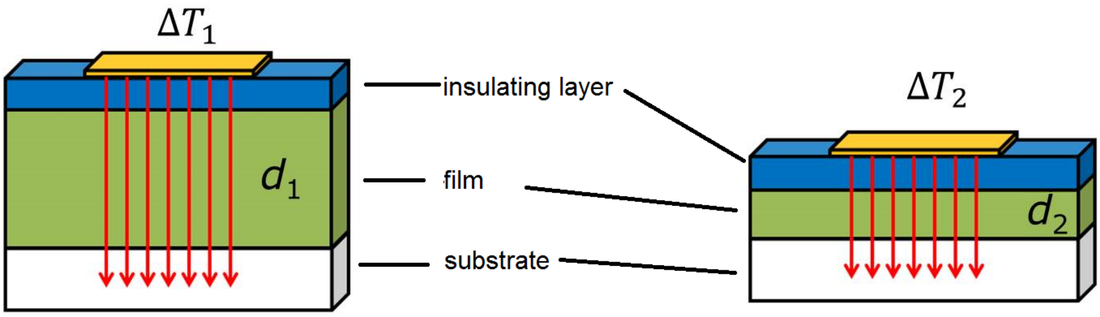

Figure 3.1.: The one-dimensional (original) 3ω method assumes thermal transport parallel to the sample surface. Information about the thin film is obtained from the difference between sample (left) and reference sample (right). The gold layer on top is used as a measuring device for the temperature increase ΔT.

1999, Goodson et al., 1995, Tritt, 2004).

- **Frequency domain thermoreflectance** on the other hand is a method that exploits the frequency space instead of the time domain. Here, the photothermal response is detected in the probing signal. A continuous laser with a certain modulation frequency illuminates the sample. The reflected probe laser beam is subject to modulations caused by the modulation of the temperature on the sample surface. By scanning the probing beam across the surface, amplitude and phase maps are generated, that are evaluated to result in a value of the thermal conductivity. (Tam, 1986)

- **AC calorimetry** is a hybrid method that combines optical heating with electrical detection. The temperature profile on the sample induced by a laser beam is measured by thermocouples patterned directly onto the sample. If the distance between laser spot and sensor is varied, the thermal diffusivity $\alpha = \frac{\kappa}{\rho c_s}$ can be calculated. Here, ρ is the material density and c_s the specific heat (Sullivan and Seidel, 1968, Rosencwaig et al., 1985, Pottier, 1994, Langer et al., 1997). Alternatively, the sample can be heated electrically and the reflectance change is then evaluated to infer the thermal conductivity (Tritt, 2004).

The 3ω method relies on a thermal wave[1] introduced into a material by an AC current of angular frequency ω and a response voltage at the third harmonic, which is a measure of the temperature increase in the sample caused by the thermal wave. Based on the idea of heat flow strictly perpendicular to the sample surface (Fig. 3.1) and through a set of assumptions the original derivation manipulates the solution of the heat diffusion equation. This one-dimensional method (section 3.1) takes two forms (Fig. 3.2). In one case the slope of the response voltage with the natural logarithm of 2ω is inversely proportional to the thermal conductivity (slope method). In the second form the difference between the respective temperature rise in two samples with different thicknesses but otherwise identical setup is considered to determine κ (differential method).

---

[1] The periodical heating of the sample technically does not cause a thermal wave in the sample but rather an exponential decay of the temperature profile. Nevertheless ‘thermal wave’ is the term generally used in the literature to describe this concept.

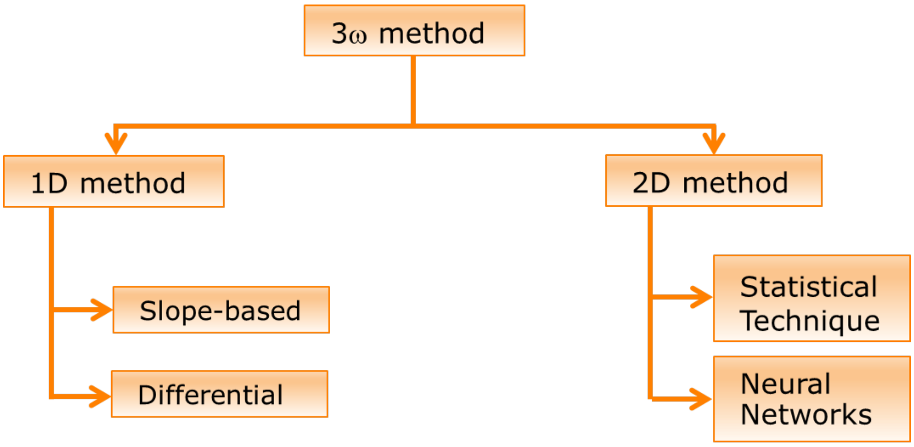

Figure 3.2.: Overview of the main options for 3ω measurements.

However, the one-dimensional approach is subject to several drawbacks, which restrict the applicability of the method to very specific cases and are specified in Section 3.2. Therefore, a two-dimensional approach is reviewed that eliminates the need for the approximations required in the one-dimensional case and presents a novel data evaluation scheme (Fig. 3.2; Section 3.3). The last section of this chapter discusses the measurement setup and experimental uncertainties.

While the relationship between frequency f and angular frequency ω is $\omega = 2\pi f$, which is relevant for data evaluation, in the text both 'frequency' and 'angular frequency' will be used synonymously, as the physical information content in an equation is not modified by the prefactor of 2π. Parts of this chapter were published as publication [P4][2].

3.1. The Original 3ω Technique

This section focuses on the measurement of the cross-plane thermal conductivity. In the following the mechanism of the 3ω method will briefly be explained (everything required to evaluate data taken) before the section goes into more detail in a strict derivation beginning at the basic level of the heat conduction equation.

---

[2] Although the content of this and the other publication has been adapted to fit the flow of the thesis, it is, for reasons of scientific honesty, to be pointed out that congruence in wording cannot be excluded in every case.

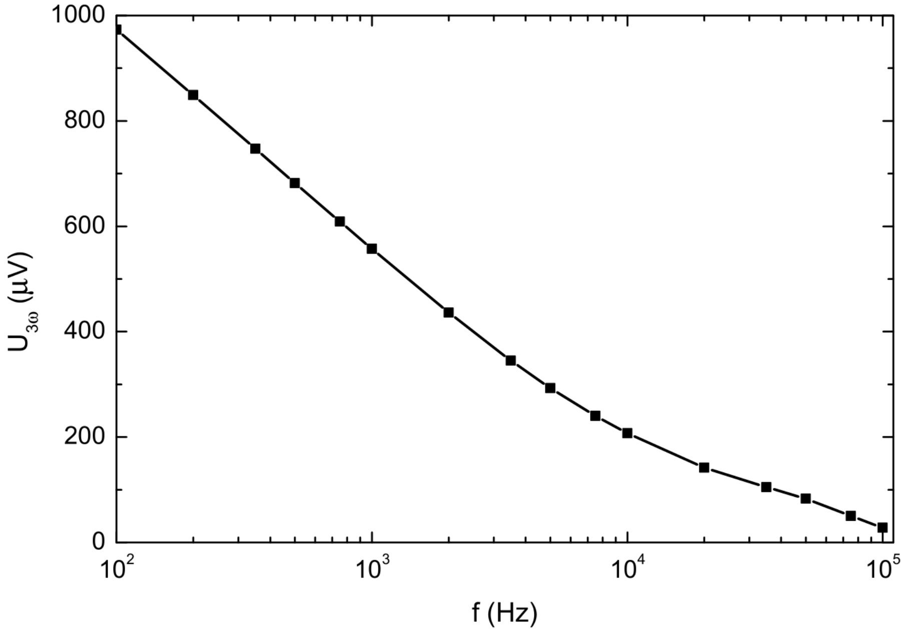

Figure 3.3.: Measured frequency dependency of $U_{3\omega}$ of a 2.1 μm thick film of Y$_3$Fe$_5$O$_{12}$ on a Gd$_3$Ga$_5$O$_{12}$ substrate. The frequency-dependent transition between a penetration depth larger than the film thickness to smaller than the film thickness is clearly visible at approximately 10^4 Hz.

In short, the thermal conductivity is measured by the differential 3ω method (Cahill and Pohl, 1987, Cahill, 1990), which uses a micrometer sized metallic (in this case: gold) structure simultaneously as a heater and as a measurement device for the thermal resistivity of the sample. An alternating current $I(t) = I_0 \sin(\omega t)$ with a frequency ω is applied to the heater structure heating the sample with a frequency of 2ω. This heating causes the resistance R of the heater itself to oscillate periodically with 2ω around an equilibrium value, since the electrical power is proportional to the square of the current. The temperature dependency of the resistance is linearized to $R(T) = R_0 + \frac{dR}{dT}\Delta T$. Inserting this into Ohm's law and simplifying the expression using trigonometric identities results in an expression for the measurement voltage with a 1ω and a 3ω contribution:

$$U = R_0 I_0 \cos(\omega t) + \frac{I_0 \Delta R(\Delta T)}{2}\left[\cos(3\omega t + \phi) + \cos(\omega t + \phi)\right]. \tag{3.1}$$

Here, ΔT is the temperature oscillation within the heater structure, ϕ is a phase, and ΔR is the amplitude of the resistance change caused by the heating. Following the derivation of Cahill (1990) and the corresponding erratum (Cahill, 2002), the temperature oscillation in the film is related to the response voltage $U_{3\omega}$ by

$$\Delta T = \frac{2}{\frac{dR}{dT}} R \frac{U_{3\omega}}{U_\omega} \tag{3.2}$$

and depends on the heater's temperature coefficient of resistance $R/(dR/dT)$ and on the electric heating power applied via U_ω. In addition, $U_{3\omega}$ is frequency dependent through Eq. 3.1 (Fig. 3.3).

To determine the thermal conductivity of the sample material, the heat resistance of the film is compared to that of a reference sample with a smaller film thickness (differential method). The difference between sample and reference sample in temperature oscillation, $\Delta T_{\mathrm{df}} = \Delta T_{\mathrm{film}} - \Delta T_{\mathrm{ref}}$, then relates to the thermal conductivity of the thin film by

$$\kappa = \frac{Pd}{2bl\Delta T_{\mathrm{df}}}\,, \tag{3.3}$$

with P being the heating power, d the thickness of the film, $2b$ the heater width, and l its length.

Concerning the detailed derivation that will follow now to provide a more detailed understanding one again needs to begin at the AC heating current $I(t) = I_0 \sin(\omega t)$ applied to the measurement structure. Assuming that the induced resistance changes are small ($\frac{\Delta R(t)}{R_0} \ll 1$), the time dependent heating power can be expressed by

$$P(t) \approx I_0^2 R_0 \cos^2(\omega t) = \frac{I_0^2 R_0}{2}(1 + \cos(2\omega t)). \tag{3.4}$$

The first term of this equation refers to a temperature gradient caused by average heating, whereas the second term describes temperature oscillations $\Delta T = \Delta T_0 \cos(2\omega t + \phi)$ around the average temperature. The physical process causing the heating power to be transformed into temperature oscillations is elegantly described (Kimling, 2013) in terms of a convolution with a transfer function $Z(\omega)$ by

$$\Delta T(t) = P(t) \wedge \mathcal{F}^{-1}[Z(\omega)], \tag{3.5}$$

where $\mathcal{F}^{-1}$ denotes the inverse Fourier transform and $\wedge$ the convolution. Applying this to Eq. 3.4, Kimling (2013) obtains

$$\Delta T(t) = \frac{I_0^2 R_0}{2}[Z(0) - \mathcal{R}\{Z(2\omega)\}\cos(2\omega t) + \mathcal{I}\{Z(2\omega)\}\sin(2\omega t)]. \tag{3.6}$$

Here, $\mathcal{R}$ and $\mathcal{I}$ denote the real and imaginary parts of a function, respectively. Assuming then that second order contributions to the Taylor series of $R(T)$ can be neglected, $R(t)$ can be expressed as

$$R(t) = R_0 + \frac{dR}{dT}\Delta T. \tag{3.7}$$

Multiplying this linearized expression for the resistance by $I(t) = I_0 \sin(\omega t)$ leads to an expression for the time dependent voltage:

$$\begin{aligned} U(t) &= R_0 I_0 \sin(\omega t) \\ &\quad + \frac{dR}{dT} I_0^3 R_0 \left[\left(\frac{Z(0)}{2} + \frac{\mathcal{R}\{Z(2\omega)\}}{4} \right) \sin(\omega t) + \frac{\mathcal{I}\{Z(2\omega)\}}{4} \cos(\omega t) \right] \\ &\quad - \frac{dR}{dT} I_0^3 R_0 \left[\frac{\mathcal{R}\{Z(2\omega)\}}{4} \sin(3\omega t) + \frac{\mathcal{I}\{Z(2\omega)\}}{4} \cos(3\omega t) \right]. \end{aligned} \tag{3.8}$$

It is therefore possible to determine the transfer function either by the first or by the third harmonic of the excitation frequency, provided knowledge of $P(t)$. The 1ω method (Völklein et al., 2009), however, is vulnerable to large uncertainties, as both the driving voltage signal and the measurement signal are on the same harmonic.

The 3ω method is immune to this problem. Its derivation begins at the heat conduction equation, which can be written in the form

$$\frac{\partial}{\partial t} u(\mathbf{x}, t) - \alpha \Delta u(\mathbf{x}, t) = 0 \tag{3.9}$$

where $u(\mathbf{x}, t)$ is an arbitrary field of position and time and Δ is the Laplace operator. If u is taken to be the temperature, in analogy to the Einstein diffusion equation, α is usually termed 'thermal diffusivity'. Assuming that the velocity of a heat wave through a material is independent of its frequency (i.e. there is no dispersion), the temperature oscillation ΔT within the material is given by Carslaw and Jäger (1959) as

$$\Delta T = -\frac{P}{l\pi\kappa} K_0(qr) e^{i2\omega t}, \tag{3.10}$$

with $K_0(qr)$ the zeroth-order modified Bessel function, l the length of the measurement structure, κ the thermal conductivity, and q^{-1} the wavelength of the thermal diffusive wave[3]. Eq. 3.10 then is the key to the mathematical evaluation of the transfer function (Dames and Chen, 2005). By separating out the real part to

$$\mathcal{R}\{\Delta T(\mathbf{r}, t)\} = -\frac{P}{l\pi\kappa} [-\mathcal{R}\{K_0\} \cos(2\omega t) + \mathcal{I}\{K_0\} \sin(2\omega t)] \tag{3.11}$$

and comparing it to Eq. 3.6, Kimling (2013) finds

$$Z(\omega) = \frac{1}{l\pi\kappa} K_0(qr). \tag{3.12}$$

As described above, the 3ω method applies a sinusoidal current to heat the sample periodically. The heating power therefore oscillates at $P \propto \sin(2\omega t)$ around an average value. The above-average contribution heats the sample, while the below-average contribution results in net heat transport away from the heater and thereby effectively cooling it. The amplitude of the thermal oscillation is therefore proportional to the integral of the heating power above the average for half a period:

---

[3] Cahill (1990) termed this property 'thermal penetration depth', even though it actually refers to the distance to the heat source, at which the Bessel function has decreased to $1/e$.

$$\Delta T \propto \Delta Q \propto \int_0^{\pi/(2\omega)} \sin(2\omega t)\,\mathrm{d}t = \frac{1}{\omega}. \tag{3.13}$$

Therefore, the temperature oscillation measured in the heater structure is reduced with the frequency ω with $\frac{1}{\omega}$ behavior.

The factor q scaling Eq. 3.10 is related to the drop of the Bessel function. As heat is transported away in spherical half-shells with radius r, the energy density is reduced as $\frac{1}{r^2}$, so that

$$\Delta T \propto \frac{1}{q^2}\,. \tag{3.14}$$

In combination with Eq. 3.13 this implies a frequency dependency of the thermal penetration depth of

$$q^{-1} \propto \frac{1}{\sqrt{\omega}}\,. \tag{3.15}$$

Similar reasoning leads to the conclusion that the thermal penetration depth is proportional to the square root of the thermal diffusivity α (Cahill and Pohl, 1987), so that

$$|q^{-1}| = \sqrt{\frac{\alpha}{2\omega}} = \sqrt{\frac{\kappa}{2\omega\,\rho c_\mathrm{s}}}\,. \tag{3.16}$$

Here, κ is the thermal conductivity, ρ the density, and c_s the specific heat capacity of the material.

In the above derivation the finite width of the heater line has not yet been considered. The derivation by Cahill (1990) only takes into account temperature oscillations on the surface of the sample stack, as the heater is used as the measurement device. Convolving the geometry of the heat source with the temperature oscillation is required to resolve this issue and mathematically is equivalent to multiplication in Fourier space. In regions sufficiently far away from the heater, the Bessel function approaches exponential decay as

$$K_0(x) \rightarrow \sqrt{\frac{\pi}{2x}} e^{-x} + \mathcal{O}(\frac{1}{x}), \tag{3.17}$$

so that the Fourier transform becomes

$$\Delta T(k) = \frac{P}{2l\kappa}\frac{1}{\sqrt{k^2+q^2}}. \tag{3.18}$$

Multiplication with the Fourier transform of the geometry of the heater line ($\frac{\sin(kb)}{kb}$ with $2b$ the width of the heater) and inverse Fourier transform of the result leads to an expression for the temperature oscillation. This expression needs to be averaged over the entire heater, because the measurement quantity in the 3ω method is the average temperature oscillation within the heater. Thus, the resulting expression describing the temperature change to be measured is

$$\Delta T(x) = \frac{P}{l\pi\kappa} \int_0^\infty \frac{\sin^2(kb)}{(kb)^2\sqrt{k^2+q^2}}\, dk. \tag{3.19}$$

Eq. 3.19 can now be approximated, if $|qr| \ll 1$ is assumed; the requirement can be fulfilled by adjusting the size of the heater structure. This results in

$$\Delta T(r) = \frac{P}{l\pi\kappa}\left(\frac{1}{2}\ln\frac{\alpha}{r^2} + \ln 2 - 0.5772 - \frac{1}{2}\ln(2\omega) - \frac{i\pi}{4}\right), \tag{3.20}$$

which has the property and advantage that the frequency dependent (real) part and the imaginary part are separated (Cahill and Pohl, 1987). Both the in-phase and out-of-phase components can be used to determine thermal conductivity, and in particular the slope of the real part with respect to $\ln(2\omega)$ can be evaluated ('slope method'). The in-phase contribution, however, has proven to give more reliable results (Cahill, 1990).

The combination of the third-harmonic contribution to Eqs. 3.7 and 3.8 results in an approximation of the voltage at the third harmonic and therefore to

$$\Delta T = \frac{2}{\frac{dR}{dT}} R \frac{U_{3\omega}}{U_0}. \tag{3.21}$$

This temperature oscillation is equal to that described by Eq. 3.19 or Eq. 3.20, respectively, and therefore permits the observation of the temperature oscillation by measuring the first and third harmonic of the voltage drop over the heater structure.

Finally, the magnitude of the thermal penetration depth compared to the sample thickness needs to be considered. At frequencies below 10 kHz the thermal penetration depth generally exceeds the film thickness (Fig. 3.3), so that any measurement would contain a dominant substrate contribution. To avoid this, thin film thermal conductivities are frequently measured by means of a differential method. To obtain the thermal conductivity of a thin film, two samples are measured with different film thicknesses, but otherwise identical setup. The additional material in the thick film sample causes additional thermal resistance. In analogy to Ohm's law $I = \sigma\frac{A}{l}U$, which describes the electrical current caused by a voltage U through a material with electrical conductivity σ and geometry $\frac{A}{l}$, the heat flow $\dot{Q}$ through a material with thermal conductivity κ caused by a temperature difference ΔT can in the same way be described by

$$\dot{Q} = \kappa \frac{A}{d} \Delta T. \tag{3.22}$$

If ΔT_{film} is the difference between the temperature oscillations in the sample and the reference sample caused by the change in thermal resistance, using the fact that the heat flow is caused by power oscillations and that the area below the heater is $A = 2bl$, the result is an expression for the thermal conductivity of the additional material in the sample compared to the thin reference sample:

$$\kappa = \frac{P d_{\mathrm{film}}}{2bl \, \Delta T_{\mathrm{film}}}. \tag{3.23}$$

3.2. The Two-Dimensional Expansion

The differential 3ω method (Cahill and Pohl, 1987, Cahill, 1990) uses a patterned structure on a sample simultaneously as a heater and as a measurement device for the thermal resistivity of the sample. In general, the solution of the heat diffusion equation for a film on a substrate is an integral equation for the temperature increase in the heater structure ΔT as will be demonstrated below. However, fitting the equation to measurement data is difficult because of the complexity of the equation. Therefore, techniques such as a 'differential material properties search algorithm' (Olson et al., 2005) or neural networks (Feuchter, 2014) are implemented to find a meaningful fit. In principle it may also be possible to use the Monte Carlo technique to obtain a fit, which, however, does not need to be unique. In particular, the algorithm presented by Olson et al. (2005) lacks stability and the results dramatically depend on the initial conditions of the fit.

Therefore, due to these difficulties, the equation generally is approximated to one-dimensional heat transport assuming that the thermal conductance of the substrate by far exceeds that of the film and that the thermal penetration depth is larger than the film thickness. The first requirement imposed to approximate the integral equation can be met by a suitable choice of the substrate, while the second requirement can only be met by choosing an adequate heater structure and measurement frequency, which restricts the thermal penetration depth. This requires careful electron beam lithography and a high-frequency (> 1 MHz) lock-in amplifier. Both setups are not available in many institutes, so that a powerful alternative is required. The differential method can then be employed to determine the thermal conductance of the film. The slope-method, however, is inapplicable at low temperatures, as the slope of ΔT with respect to $\ln(2\omega)$ approaches zero with decreasing temperature (Fig. 3.4). The two assumptions can, nontheless, be obliterated by instead extending the integral equation for the temperature increase in the heater to a model of two-dimensional heat transport, which allows heat to flow in the in-plane direction.

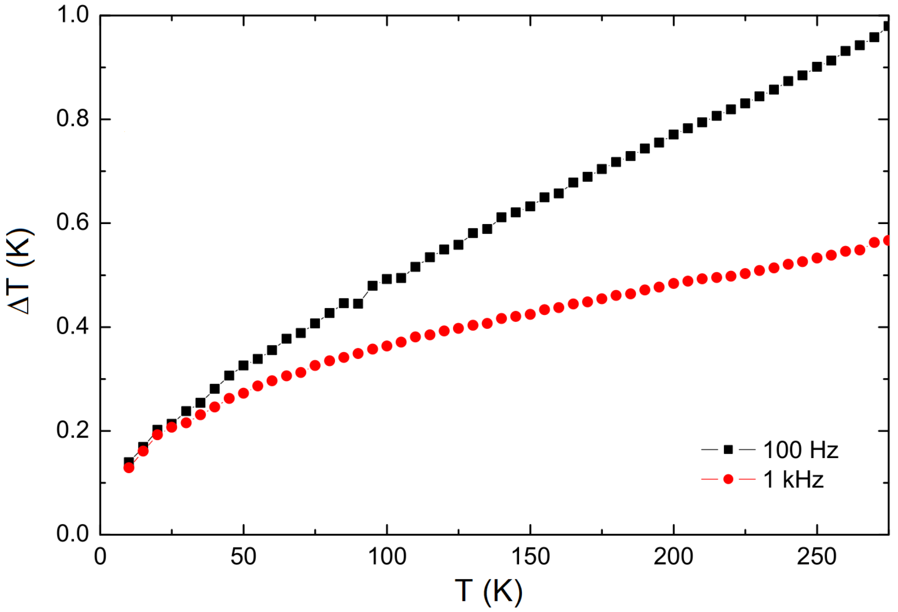

Figure 3.4.: Temperature oscillations measured at frequencies 100 Hz and 1 kHz in a sample of 6.7 μm thick YIG ($Y_3Fe_5O_{12}$) grown on GGG ($Gd_3Ga_5O_{12}$). The difference of the temperature oscillations clearly approaches zero for low temperatures.

Following the treatment of Feldman (1996), which builds on the matrix formalism of Carslaw and Jäger (1959, p. 110 ff.), an iterative model can be constructed, that models two-dimensional heat transport through an arbitrary number of thin film layers and finally leads to Eq. 3.32. In general, the heat equation, Eq. 3.9, is solved for a sample stack consisting of two media a and b, if heating in z direction is treated as a boundary condition, so that the temperature profile perpendicular to the film surface, $T(z)$ is given by

$$T(z) = T^+ e^{uz} + T^- e^{-uz}, \tag{3.24}$$

where $u^2 = -i\frac{\omega}{\alpha}$, α is the thermal diffusivity, and $T^\pm$ are constants. Vectorial treatment allows a formulation as

$$\mathbf{T}(z) = \underline{\underline{U}} \begin{pmatrix} T^+ \\ T^- \end{pmatrix} = \begin{pmatrix} e^{uz} & 0 \\ 0 & e^{-uz} \end{pmatrix} \begin{pmatrix} T^+ \\ T^- \end{pmatrix}, \tag{3.25}$$

where $\underline{\underline{U}}$ is the transport matrix describing the thermal penetration depth. At an interface $z = \zeta$ between the media a and b heat is taken to flow continuously, so that

$$T_a(\zeta-) = T_b(\zeta+) \tag{3.26}$$

$$\kappa_a \frac{dT_a}{dz}\bigg|_{z=\zeta-} = \kappa_b \frac{dT_b}{dz}\bigg|_{z=\zeta+} . \tag{3.27}$$

$\kappa_{a,b}$ are the thermal conductances of the media a and b. If heat was applied to the boundary, a complication not considered here, the right hand side would be increased by a factor depending on the heat flux.

Inserting Eq. 3.24 into Eq. 3.27, one obtains

$$\begin{aligned} T_a^+(\zeta-) + T_a^-(\zeta-) &= T_b^+(\zeta+) + T_b^-(\zeta+), \\ \gamma_a T_a^+(\zeta-) - \gamma_a T_a^-(\zeta-) &= \gamma_b T_b^+(\zeta+) - \gamma_b T_b^-(\zeta+), \end{aligned} \tag{3.28}$$

where $\gamma = u\kappa$. Formulating Eq. 3.28 as a matrix,

$$\mathbf{T}_b = \underset{=}{\Gamma_{ba}} \mathbf{T}_a \tag{3.29}$$

follows, where the transmittance matrix $\underset{=}{\Gamma_{ba}}$ is given by (Feldman, 1996)

$$\underset{=}{\Gamma_{ba}} = \frac{1}{2\gamma_b} \begin{pmatrix} \gamma_b + \gamma_a & \gamma_b - \gamma_a \\ \gamma_b - \gamma_a & \gamma_b + \gamma_a \end{pmatrix} . \tag{3.30}$$

The asymmetry in γ_b arises from the fact, that the transmittance from layer a to layer b is quantified by the ratio of the thermal conductances and therefore by the ratio γ_a/γ_b. An isotropic interface resistance R between two layers is taken into account by an additional transmittance matrix $\underset{=}{\Gamma_{\mathrm{R}}}$ (Carslaw and Jäger, 1959, p. 110 ff.)

$$\underset{=}{\Gamma_{\mathrm{R}}} = \begin{pmatrix} 1 & -R \\ 0 & 1 \end{pmatrix} . \tag{3.31}$$

The quantity R is analogous to the inverse thermal transmittance and is given in units $\left(\frac{\mathrm{W}}{\mathrm{m^2K}}\right)^{-1}$. As in the case of the 3ω method heating and sensing of the temperature takes place at the top of the sample, only the energy contribution not transported through the sample needs to be considered. Such transformations, as given by Eq. 3.29, are generalizable to the anisotropic case of a multilayer by matrix multiplication and allow the calculation of the temperature at each interface and at the top of the sample stack, respectively (Feldman, 1996, Borca-Tasciuc et al., 2001, Olson et al., 2005, Kimling, 2013). In principle, it is even possible to include Kapitza-type thermal interface resistances by Eq. 3.31 (Olson et al., 2005).

This generalized formalism was applied to the systems studied in this project. The integral equation Eq. 3.19 is in particular extended for the case of our setup consisting of an Al_2O_3

layer and a film (or superstructure) on a substrate, as was demonstrated by Borca-Tasciuc et al. (2001). If a transmission matrix $\underline{\underline{\Gamma}}$ is defined to be $\begin{pmatrix} A^+ & B^+ \\ A^- & B^- \end{pmatrix}$, and if one defines $A = c_1 A^+ + c_2 A^-$ and $B = c_3 B^+ + c_4 B^-$ with c_i being constants, the result neglecting interface resistance is given by

$$\Delta T = -\frac{P}{\pi l \kappa_{z,1}} \int_0^\infty dk \, \frac{1}{A_1 B_1} \frac{\sin^2(bk)}{(bk)^2}, \tag{3.32}$$

where A_1 and B_1 are given by the recursive sequence

$$\begin{aligned} B_i &= \sqrt{\frac{\kappa_{xy,i}}{\kappa_{z,i}} k^2 + \frac{2i\omega}{\alpha_{z,i}}}, \\ A_{i-1} &= \frac{A_i \frac{\kappa_{z,i} B_i}{\kappa_{z,i-1} B_{i-1}} - \tanh(B_{i-1} d_{i-1})}{1 - A_i \frac{\kappa_{z,i} B_i}{\kappa_{z,i-1} B_{i-1}} \tanh(B_{i-1} d_{i-1})}, \\ A_n &= -1. \end{aligned} \tag{3.33}$$

In this set of equations ω is the measurement AC angular frequency, i denotes the i-th layer counting from the top ($i = n$ labeling the substrate), $\kappa_{xy,i}$ and $\kappa_{z,i}$ denote the in-plane and cross-plane thermal conductance, respectively, $\alpha = \frac{\kappa}{\rho c_s}$ is the thermal diffusivity given by the thermal conductance, the density ρ and the specific heat c_s and d_i is the thickness of the i-th layer. The hyperbolic tangent is defined as the ratio of hyperbolic sine and cosine, which essentially are given by $e^x \pm e^{-x}$; both exponentials arise in the transport matrix $\underline{\underline{U}}$ (Eq. 3.25), and the full treatment of Carslaw and Jäger (1959, p. 110 ff.) analytically leads to the hyperbolic expression. Any interface resistance between layers i and $i-1$ could in principle be added as a constant factor to A_{i-1}. As arbitrary thicknesses d_i can enter the calculation, this method is independent of the thickness of the individual layers. However, as the thermal 'wave' decays exponentially within a layer, layers thicker than approx. 100 μm are difficult to analyze.

The real part of the temperature oscillation resembles an improved version of the one-dimensional approach by including the anisotropy of the thermal conductance $\frac{\kappa_{xy}}{\kappa_z}$. In addition, the real part depends on the density and the specific heat only by cross-terms introduced by the multiplication of complex numbers (e.g. $A_i \cdot B_i$). The imaginary part in particular includes an $\alpha_{z,i}^{-1}$ term and therefore is a measure for the density and the specific heat, but is also sensitive to the cross-plane thermal conductance. As the temperature approaches zero, B_i approaches infinity, which causes the frequency independence of the temperature oscillation at low temperatures.

3.3. Computational Implementation

For the case of an unknown set of material parameters $\{\kappa_{\mathrm{xy}}, \kappa_{\mathrm{z}}, \rho, c_{\mathrm{s}}\}$ of each layer Eq. 3.32 contains $4 \cdot N_{\mathrm{layers}}$ free parameters. The problem consisting of the set of equations and measurement data could theoretically possess a unique solution, if the measured set of frequencies was equal to or greater than the number of free parameters. As a result, the large number of parameters leads to a high degree of computational complexity and instability. Assuming that all properties of all layers except for the layer of interest are known from previous measurements (e.g. the differential method is applied and therefore all properties of the Al_2O_3 and the substrate are known), the number of free parameters can be reduced to four (the parameters for the film only).

The sensitivity of Eq. 3.32 to the material parameters κ_{xy}, κ_{z}, ρ and c_{s} allows further simplification. Fig. 3.5 displays the expected temperature oscillation ΔT and first derivatives of ΔT with respect to each material parameter for a range of in-plane and cross-plane thermal conductivities and thermal diffusivities. The other two parameters, respectively, were kept constant at an arbitrary value. The sensitivity s of the model to a change of a parameter p_i, displayed in Fig. 3.5, is approximately given by the derivative of ΔT with respect to that parameter multiplied by 1% of the parameter, so that

$$\mathrm{s(p_i)} = \frac{\partial \Delta T}{\partial p_i} 0.01 p_i. \tag{3.34}$$

In the cases of the thermal conductivities the sensitivity is of the order of $10^{-5} \ldots 10^{-6}$ K. The sensitivity to a change of the thermal diffusivity is of the order of 10^{-7} K. However, the thermal diffusivity is a function of both density and specific heat capacity, so that the sensitivity to these parameters is smaller by two and three orders of magnitude, respectively. The sensitivity to changes in ρ and c_{s} is of the order of 10^{-9} K at small parameter values ($\rho \approx 1000\ \mathrm{kg/m^3}$, $c_{\mathrm{s}} \approx 100\ \mathrm{J/(kg\,K)}$) and 10^{-7} at very large values ($\rho \approx 10000\ \mathrm{kg/m^3}$, $c_{\mathrm{s}} \approx 1000\ \mathrm{J/(kg\,K)}$). Because of the very small sensitivity of ΔT with respect to ρ and c_{s}, any determination by means of a fit of Eq. 3.2 to experimental data will therefore be prone to large uncertainties and is only possible for materials with a very large density and specific heat capacity. Consequently, determining the thermal conductivities can be simplified by assuming physically sound values for the film's density and specific heat capacity (e.g. by Hofmeister (2006) for the case of $Y_3Fe_5O_{12}$ in chapter 6) and determining κ_{xy} and κ_{z} only.

As explained in the previous section, it is generally possible to use fitting techniques to obtain a fit, which, however, do not need to be unique. In such a case the fit would converge towards a parameter set depending strongly on the initial parameters and possibly represents merely a local minimum. In the case of the 3ω method, the algorithm presented by Olson et al. (2005) lacks stability and the results dramatically depend on the initial conditions of the fit, as the

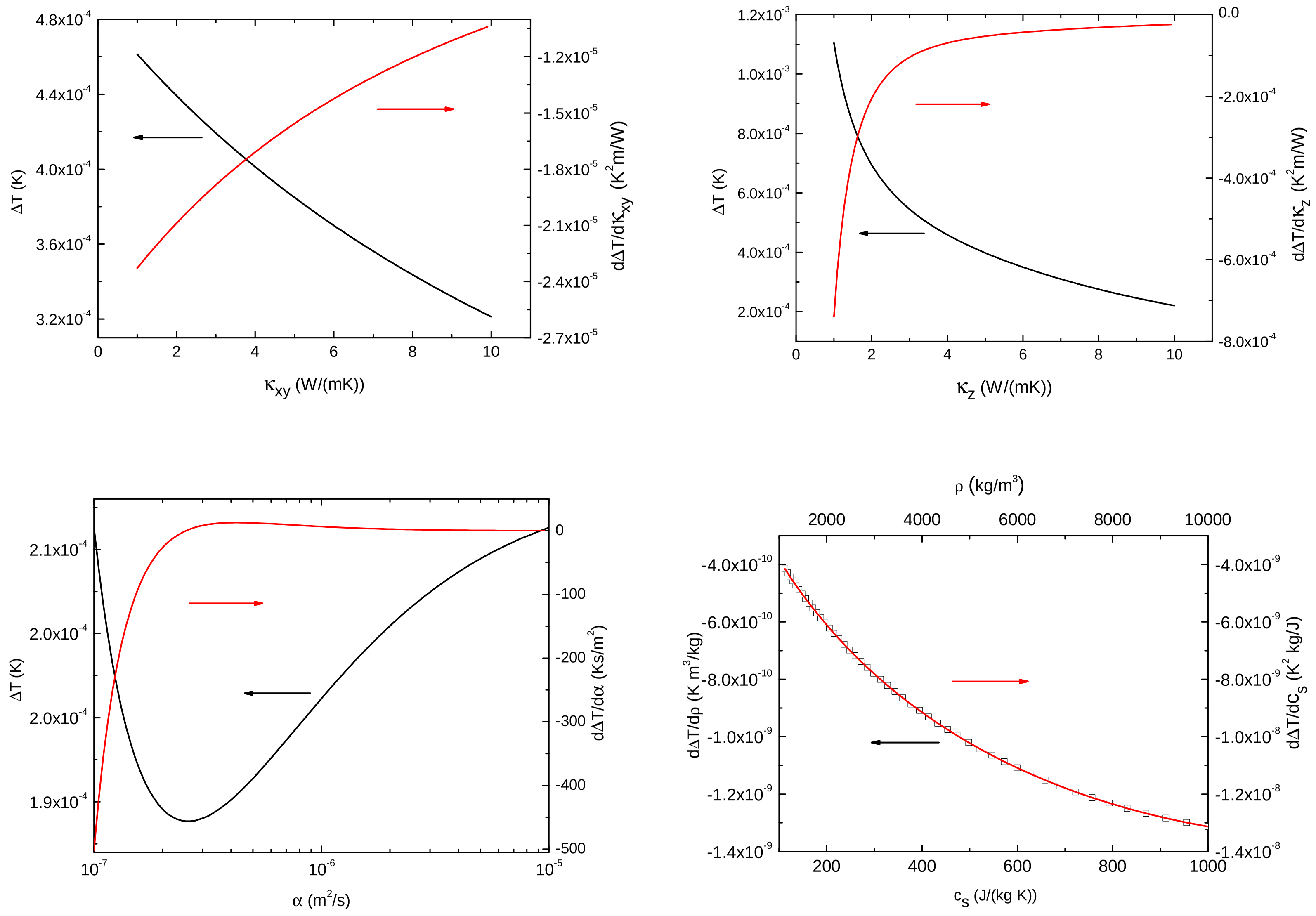

Figure 3.5.: Black lines: The temperature oscillation ΔT as a function of the in-plane thermal conductivity (top left), cross-plane thermal conductivity (top right), the thermal diffusivity (bottom left) and the specific heat capacity (bottom right). Red lines: The first derivatives of ΔT with respect to each material parameter on the x-axis as a function of this parameter. In each figure only the parameter given on the abscissa is used as a variable, while all others were kept constant at an arbitrary mean value.

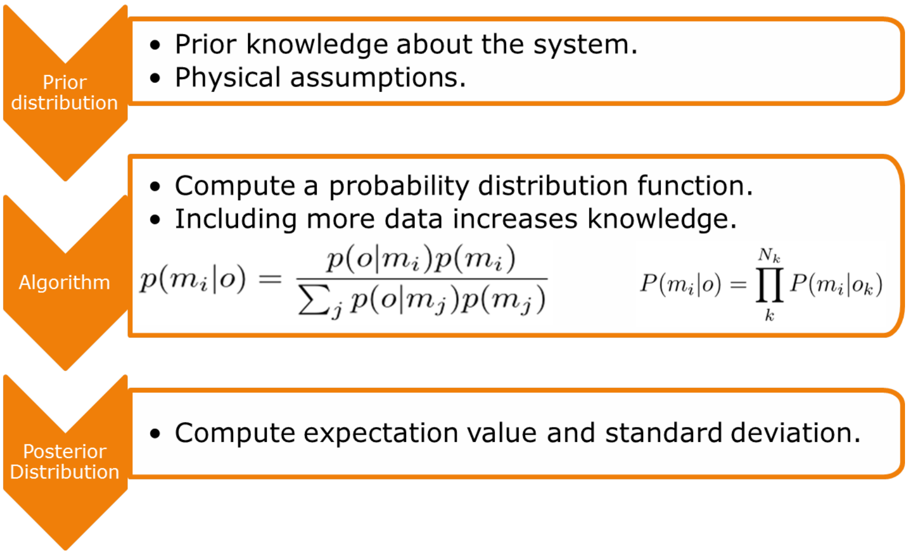
Prior distribution
• Prior knowledge about the system.
• Physical assumptions.
Algorithm
• Compute a probability distribution function.
• Including more data increases knowledge.
$p(m_i|o) = \frac{p(o|m_i)p(m_i)}{\sum_j p(o|m_j)p(m_j)}$
$P(m_i|o) = \prod_k^{N_k} P(m_i|o_k)$
Posterior Distribution
• Compute expectation value and standard deviation.

Figure 3.6.: Workflow of the Bayesian method implemented to solve the inverse problem of finding the thermal conductance from Eq. 3.32.

mathematical problem possesses features of an inverse problem (for an introduction see e.g. Stuart (2010)). To circumvent this difficulty, a new algorithm has been implemented for this research based on the expectation-maximization algorithm and its expansion, the variational Bayes method.

In frequentist statistics the underlying assumption is the law of large numbers, where the distribution of a sample will eventually approximate a Gaussian distribution determined by a mean μ and a standard deviation σ. In Bayesian statistics this is not the case and prior knowledge of the problem is used to determine an empirical probability distribution function (PDF). The workflow is illustrated in Fig. 3.6. In both cases the expectation value of the distribution can subsequently be calculated from the usual definition via the first moment of the distribution function,

$$E[X] = \sum_{i=1}^{\infty} x_i f(x_i), \tag{3.35}$$

assuming that the series converges absolutely (i.e. the series of the absolute values converges). In the case of all physical problems considered in this thesis this is fulfilled because of the restriction of $\mathbb{R}$ to an interval to be defined depending on the experiment and physical values being finite. Assuming that one attempts to compute the probability of an event m_i under the condition that event o occurs, the definition of conditional probability provides

$$P(o|m_i) = \frac{P(o \cap m_i)}{P(m_i)}, \tag{3.36}$$

where $P(o \cap m_i)$ is the unconditional joint probability of events o and m_i and

$$P(o \cap m_i) = P(m_i|o)P(o). \tag{3.37}$$

Inserting these two equations into each other and allowing for n possible outcomes leads to Bayes' theorem

$$p(m_i|o) = \frac{p(o|m_i)p(m_i)}{\sum_j p(o|m_j)p(m_j)}. \tag{3.38}$$

In this formulation m_i denotes the i-th model of a series of physical models, o denotes an observation (measurement) and $p(m_i|o)$ denotes the probability that model m_i is true provided the observation o. Vice versa, $p(o|m_i)$ is the likelihood that an observation o be made provided m_i is true. The denominator is the effective normalization of the probability to $[0,1]$. In the Bayesian framework $P(m_i)$ is the prior distribution of values m_i resembling previous knowledge (in the following termed 'prior' for brevity), $P(m_i|o)$ is the prior distribution assuming a set of data o. One of the strengths of the Bayesian approach to statistical analysis is that in contrary to frequentist statistics, which breaks down at small sample sizes, Bayesian statistics leads to reliable results also in that case, only requiring prior knowledge of the distribution. Even though usually the prior is unknown to some extent, a sufficiently meaningful data sample leads to very similar posterior PDF that are only marginally influenced by the choice of the prior. Therefore, the usual approach is to iterate the prior by using the posterior as a prior for a second repetition.

For a given posterior distribution a confidence interval can be constructed from the boundaries $L_{\alpha/2}$ and $H_{\alpha/2}$ satisfying

$$\int\limits_{L_{\alpha/2}}^{H_{\alpha/2}} P(m_i|o)\,dm_i = 1 - \alpha \tag{3.39}$$

and requiring that this interval be the shortest possible. Such an interval is commonly referred to as 'highest density region' in contrast to the classical term of the confidence interval used in frequentist statistics. The difference between a confidence interval and a highest density region comes from the fact that the existence of a prior leads to direct statements about m_i, whereas classical statistics only results in statements about m_i, if an experiment is repeated a sufficiently large number of times. Therefore, classical statistics interprets a confidence interval so that in a fraction of $1 - \alpha$ of all experiments the unknown parameter is found in the confidence interval. The Bayesian approach in contrast gives a probability $1 - \alpha$ that the highest density region actually contains the true value.

If it is assumed, for example, that an experiment is carried out to find some property and the

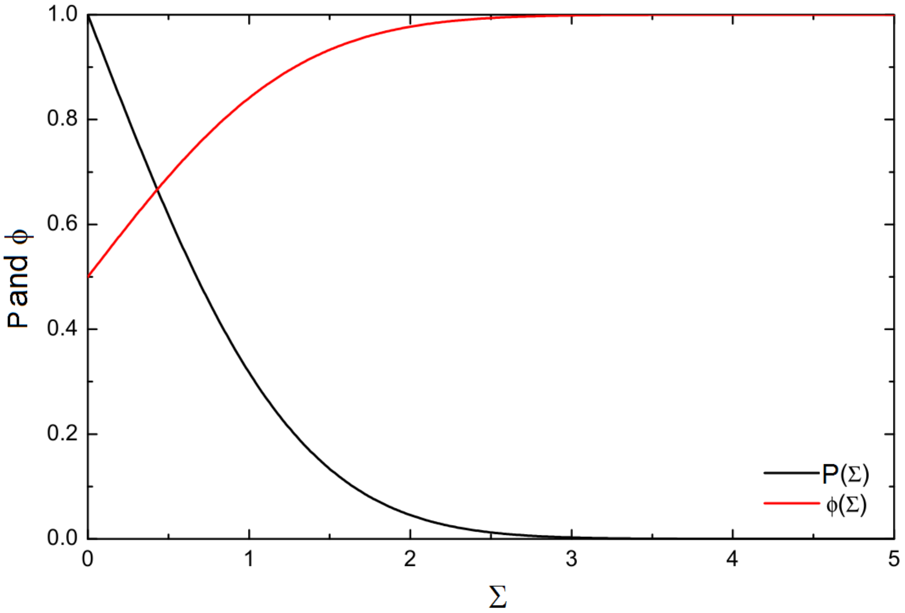

Figure 3.7.: Cumulative Gaussian distribution $\phi(\Sigma)$ (black line) and the following probability $p(\Sigma)$ of overlap between data o and model m_i (red line).

outcome is compared to N_m models of the process, then as a prior one could choose a uniform distribution. As a consequence the probability of the model m_i resulting in the observed value o is equal to $1/N_m$ for all models. The difference between model value m_i and observational value o can be expressed in terms of the uncertainty of the observation σ by $\Sigma = |\frac{m_i - o}{\sigma}|$. This number represents an approximation for the probability that the observed value actually does not come from that model: one finds (Boas, 2006, p. 547ff. and p. 763f.)

$$P(o|m_i) = 2 - 2\phi(\Sigma), \tag{3.40}$$

where $\phi(\Sigma)$ is the cumulative distribution function $\phi(\Sigma) = \frac{1}{\sqrt{2\pi}} \int\limits_{-\infty}^{\Sigma} e^{-\frac{1}{2}t^2}\, dt$ of the Gaussian distribution. If N_m models m_i and N_k observations (measurements, occurrences of event) o are combined to form a joint posterior distribution, Bayes' theorem can be applied to determine the probability that the model m_i describes the observation o

$$P(m_i|o) = \prod_k^{N_k} P(m_i|o_k). \tag{3.41}$$

For each combination of the parameters $\{\kappa_{\mathrm{xy}}, \kappa_{\mathrm{z}}, \rho, c_{\mathrm{s}}, \omega\}$ the expected ΔT is calculated to form an extensive catalogue of models. As a naive prior distribution a uniform probability distribution function (PDF) for κ_{xy} and κ_{z} is chosen. High anisotropic thermal conductances (ratios between in-plane and cross-plane thermal conductances) are unlikely to occur in nature (Boona and Heremans, 2014) and even the quasi-two-dimensional graphene has an anisotropy

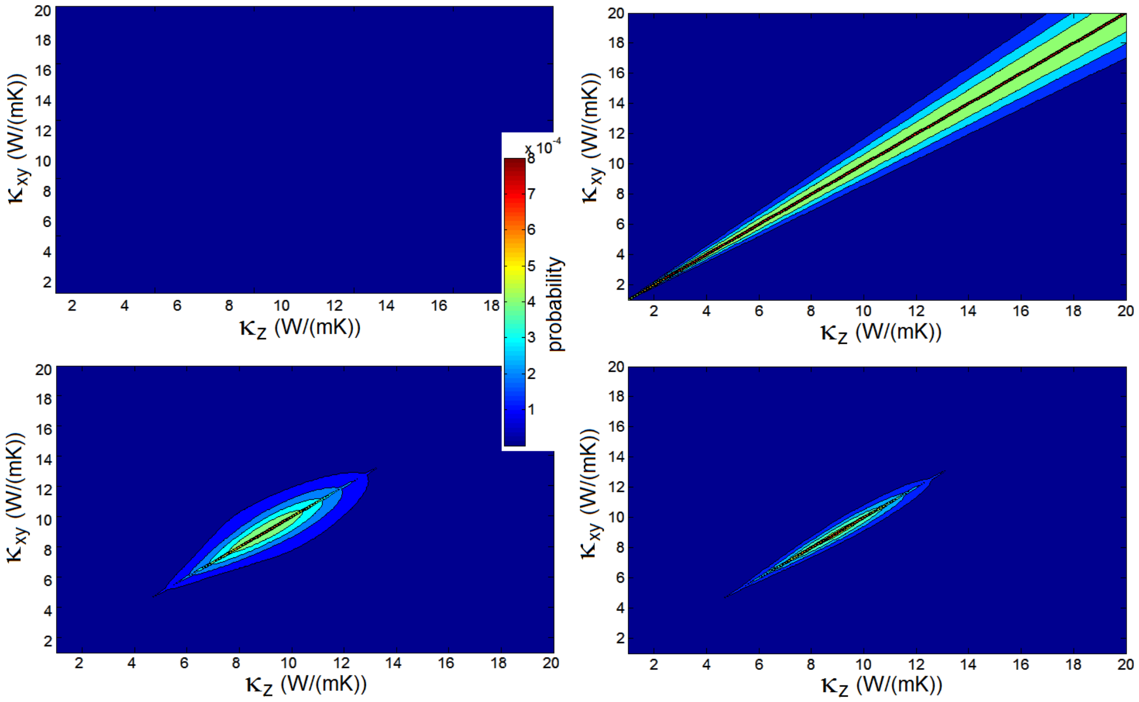

Figure 3.8.: Visualization of the PDF computation process. Top left: Uniform prior. Top right: Anisotropy biased prior. Bottom left: Anisotropy biased prior with superimposed Gaussian around a previously known value $\{\kappa_{\mathrm{xy}}, \kappa_{\mathrm{z}}\}$. Bottom right: Posterior PDF.

of 0.8 (Tian et al., 2013). Therefore, the prior is transformed by assigning each matrix point an anisotropy prior given by the probability of the anisotropy occurring, if a maximum probability is assumed for no anisotropy and a standard deviation of 0.1. Finally, for the *n*-th frequency data set the results of the *n-1*-th data set is taken into account by convolving the so far generated prior distribution function with a Gaussian distribution around the point $(\kappa_{\mathrm{xy},n-1}, \kappa_{\mathrm{z},n-1})$ of the latest data with their respective uncertainties taken as Gaussian standard deviations. This process is displayed in Fig. 3.8.

Each experimental data point $\{\omega, \Delta T\}$ is compared to the entire $\kappa_{\mathrm{xy}}/\kappa_{\mathrm{z}}$ parameter space accessible for the respective frequency using Bayesian statistics. The algorithm compares measurement data to theoretical calculations taken from the two-dimensional model of heat transport described above and computes the probability that a model describes the data point. This results in an 'intermediate' PDF, which is recursively used as a prior for the next frequency data set and thereby improves the total PDF with increasing amount of data. The PDF determined after all data has been included represents the posterior PDF for κ_{xy} and κ_{z}, from which the expectation value and the variance are computed. The algorithm is set within a parameter range, which is assumed to cover possible material properties encountered in experiment. Finally, the density and specific heat could in principle be determined by a similar algorithm.

3.4. Experimental Setup and Error Estimation

The thermal conductance of a thin film sample is measured using a 50 nm thick gold structure patterned sputtered on top of the film and structured by optical lithography using ma-P 1215 photoresist and AZ 826MIF developer. In particular, the developer was preferred over ma-D 331, because metal ions contained in the latter affect the integrity of the Al_2O_3 barrier[4]. This heater structure consists of four contact pads from which the outer two are connected by a straight heater line with a width of 20 μm and a length of 2 mm (Fig. 3.9). The inner contact pads are contacted to the heater line from the side in a symmetric way around the center of the line so that the distance between their connectors to the line is 1 mm. The connections of all four pads to the heater line are of trapezoid shape in order to reduce spurious heating effects of the leads. In the case of electrically conducting samples the gold heater is separated from the film by a sputtered polycrystalline 200 nm Al_2O_3 layer to prevent shortcuts between the contacts.

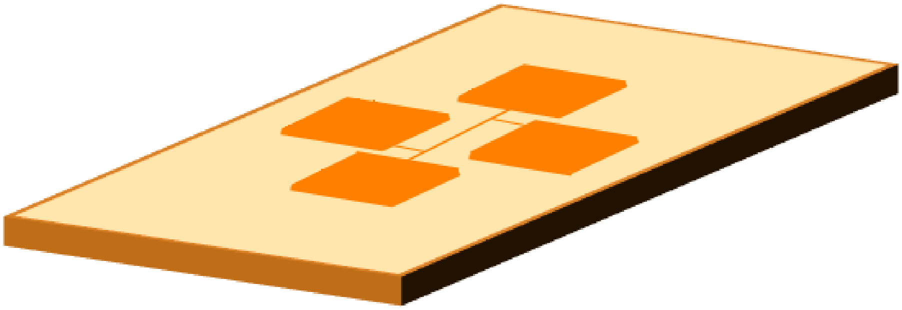

Figure 3.9.: Schematic of the 3ω structure layout (not to scale). The two outer pads are used to apply the AC current to the system, while the inner contact pads are used to measure the third harmonic of the voltage drop $U_{3\omega}$.

Using conductive silver the sample is glued to a contact chip with 12 contacts, four out of which are connected to the sample and to the measurement setup. The contacts of the chip are connected to the heater pads by thin copper wires, which are soldered to the contact chip and glued to the sample by conductive silver. Alternatively, the connection can be established using gold bond wires. No significant signal difference between the two possibilities was found, however, bonded contacts are more easily destroyed at low temperatures than glued contacts. Attaching several bonds to one contact improved the reliability. Due to the simplicity and

---

[4] Generally, the stoichiometry of the barrier will differ slightly from the ideal composition. The description Al_2O_3 is maintained for clarity.

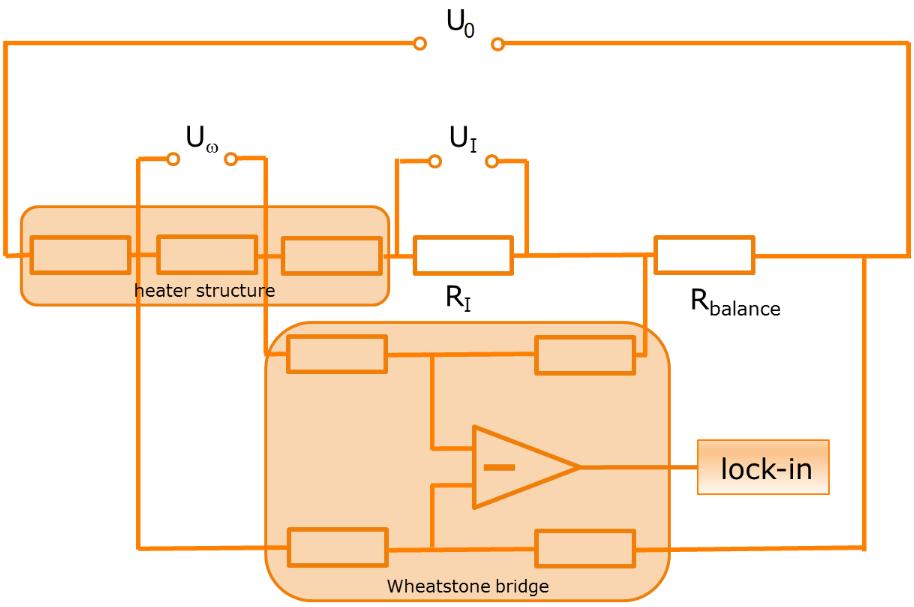

Figure 3.10.: Layout of the Wheatstone bridge used to eliminate the U_ω combination from the total signal and thereby facilitate the isolation of the 3ω component in the lock-in.

cleanliness of bonding, all experiments were performed on samples with bonded contacts. In the case of electrical transport measurements carried out simultaneously to a 3ω measurement the contacts required in four point geometry need to be bonded through the insulating Al_2O_3 layer, which can only be done using aluminum bond wire instead of gold. However, bonding through 200 nm of Al_2O_3 causes unstable bond contacts and increased noise. To resolve this difficulty the corners of the sample are covered with conduction silver prior to sputtering Al_2O_3 and Au. Subsequently the silver is removed using acetone in order to preserve a sufficient area of bare film for bonding.

The mounted sample is attached to a sample stick inserted into the variable temperature insert (VTI) of a ^{4}He cryostat to enable measurements between room temperature and 4.2 K. Direct contact between helium and the sample leads to signal distortions through thermal losses of the heater bar to the helium. Evacuating the sample area of the sample stick to less than 10^{-5} mbar or simply sealing the sample area with teflon strips to reduce helium flow in the sample area gives similar results. The helium pressure usually is stabilized between 80 and 110 mbar. Only direct contact of liquid helium with the sample is to be avoided. The caveat of both solutions is a reduction in thermal coupling between the sample and the helium flow, which restricts temperature sweep rates to 1 K/min and less.

Isolating the thermally induced voltage $U_{3\omega}$ from the total signal is achieved by a Wheatstone bridge (Fig. 3.10) that artificially isolates the U_ω contribution and eliminates it from the total

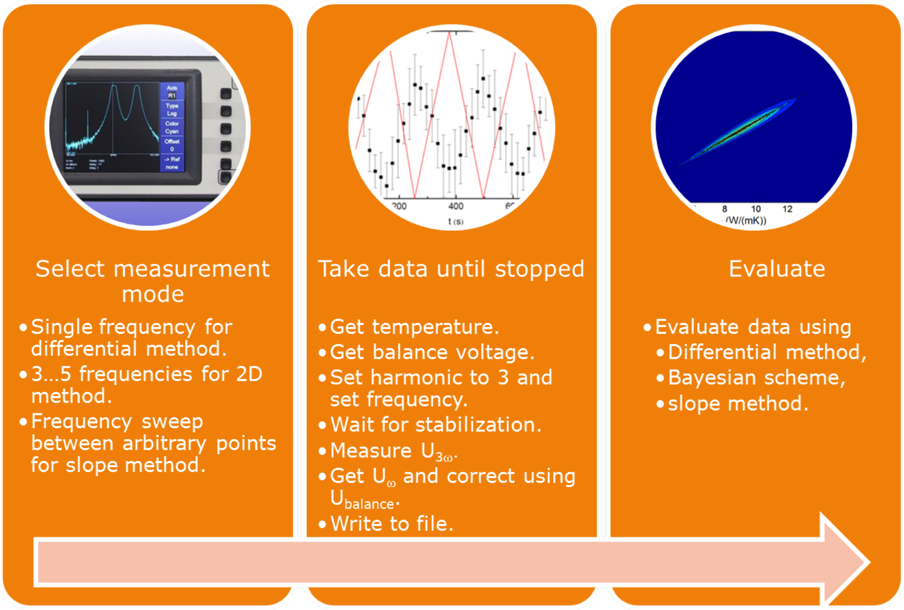

Select measurement mode

- Single frequency for differential method.
- 3...5 frequencies for 2D method.
- Frequency sweep between arbitrary points for slope method.

Take data until stopped

- Get temperature.
- Get balance voltage.
- Set harmonic to 3 and set frequency.
- Wait for stabilization.
- Measure $U_{3\omega}$.
- Get U_ω and correct using $U_{balance}$.
- Write to file.

Evaluate

- Evaluate data using
  - Differential method,
  - Bayesian scheme,
  - slope method.

Figure 3.11.: Measurement workflow as carried out for all experiments. The left image of an Anfatec elock-in amplifier is printed by courtesy of the Anfatec AG.

signal. Such a step proved necessary (Mix, 2010), because available lock-in amplifiers (Stanford Research SR850 and Anfatec eLockIn 502) were incapable of isolating the signal at 3ω otherwise, which is approximately three orders of magnitude smaller than the signal at ω. The balance of the bridge is performed by a temperature independent variable potentiometer, which can be adjusted manually or using a step motor. The remaining voltage at U_ω after the balancing process is denoted as U_{balance} and its magnitude is of the order of microvolts. The quality of the experimental result increases with decreasing balance voltage.

The measurement is finally controlled and automatized by an Agilent VEE program setting the input voltage U_0 and reading the temperature, U_ω, $U_{3\omega}$, and the balance voltage U_{balance}. It produces an output file containing the temperature, the magnetic field, the balance voltage, and the 3ω voltage at a specified number of frequencies. Data evaluation is performed using Matlab scripts. The workflow of the data taking and evaluation process is schematically shown in Fig. 3.11.

Uncertainties in the results can arise from a variety of sources, the most important being the deposition process, the lithography step, the measurement setup, and the data evaluation scheme.

The ability to control the deposition process has a crucial effect on the quality of the samples. Mastering deposition results in homogeneous samples with low surface roughness, which decreases uncertainties caused by the interface thermal resistance (Kapitza, 1941). The effect of interface roughness leads to a systematic error in the data, as the thermal conductance measured in rough samples effectively appears smaller than that of smooth samples. To minimize this effect each sample pair consisting of sample and reference sample was deposited simultaneously to exhibit identical interface structures. While reference samples without the film of interest consisting of substrate, Al_2O_3 and gold would in principle suffice, the interface structure is best matched by a sample containing an approximately 25 nm thick film layer. As the data evaluation procedure is differential, interface resistances can therefore be ignored. Secondly, deposition rates, exemplarily given for the case of LCMO (Chapter 4), are of the order of 0.1 $\frac{\text{nm}}{\text{s}}$. Considering the total film thicknesses of between 100 nm and 400 nm control of the film thickness below 1% is possible.

Furthermore, the thickness of the heater line contributes to the result (cf. Eq. 3.23). The lithography step creates the principal measurement device (the heater line) and the accuracy of measurement is mainly generated by the ability of the lithographer to fabricate identical structures reliably. The edge roughness of the heater line affects the resistance, but not the temperature coefficient of resistance, of the heater line. To correct for variabilities in the production process the heater width was corrected for the true heater width and power applied to the sample in Eq. 3.23 by measuring the heater width in an optical microscope and evaluating the width from the pixel size of the microscope camera.

The length of the heater line is an additional a potential source of error. However, because of the large length of the heater line, the relative uncertainty would be minimal and can, to first order, be neglected. In addition, the geometry of the leads contacted to the heater line could compromise the validity of the assumptions leading to Eq. 3.23. Comparing results obtained from straight and trapezoid lead geometries verified this approach and led to the conclusion that the contact structures have no significant effect on the experimental outcome. The error introduced by the heater geometry is therefore neglected in the following process to avoid accounting for the source of error twice.

Concerning the measurement setup the main sources of error are the accuracy of the temperature stabilization, the stability of the ambient helium pressure, the accuracy of the resistance balance, the determination of voltages (U_ω and $U_{3\omega}$), and the accuracy of the determination of resistance and temperature coefficient of resistance of the heater. The influence of these parameters are tested in the following. All data obtained for this analysis of measurement uncertainties are exemplarily taken at a temperature of 250 K and at a AC frequency of 750 Hz. The results do not vary quantitatively with temperature. Any temperature can be set to an accuracy of 0.05 K below 140 K and 0.09 K above 140 K. The frequency used affects the scatter in almost all data recorded between 100 Hz and 1 MHz. Measurements of highest precision and reliability seem to be possible at 750 Hz in the range below 10 kHz and in the range between 10 kHz and 100 kHz. Data were taken at logarithmically spaced frequency

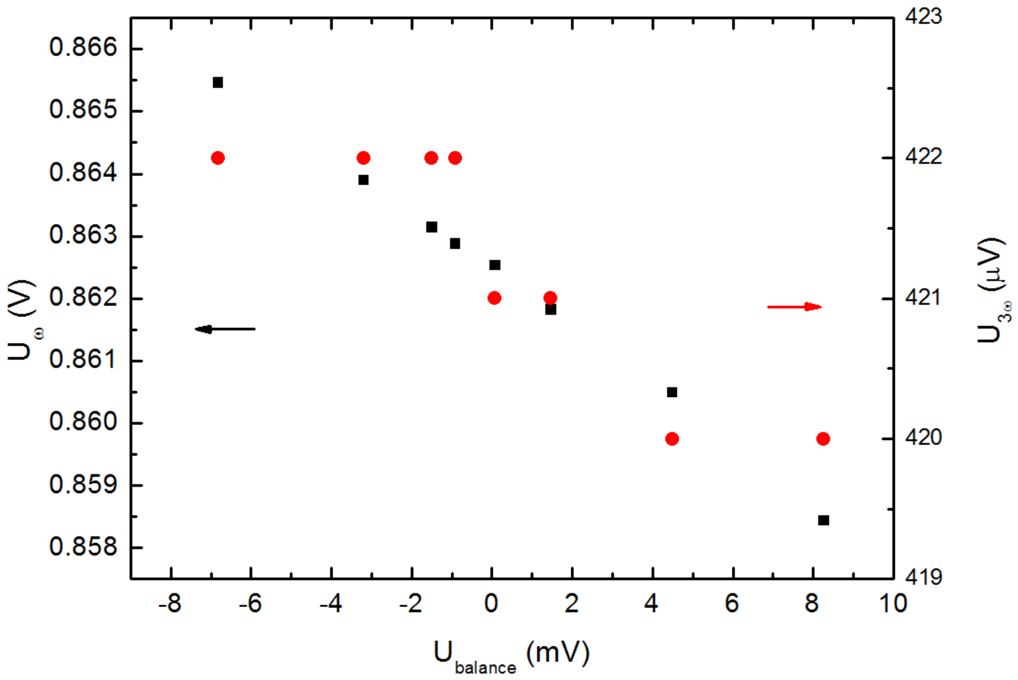

Figure 3.12.: The effect of the balance voltage on U_ω (black squares) and $U_{3\omega}$ (red circles).

points to avoid any effect of the 50 Hz grid, even though measurement at frequencies that were integer multiples of the net frequency did not display a significant difference to data taken at harmonics of 50 Hz.

To determine the credibility of the Bayesian analysis method, data taken on $La_{0.67}Ca_{0.33}MnO_3$ (chapter 4) were re-evaluated, which had been evaluated using the conventional differential 3ω method. Our results agree very well within the experimental uncertainty and reproduce the results obtained in the cited reference.

In addition, a sample consisting of Au/Al_2O_3/MgO was compared to a second sample Au/MgO to determine possible interface contributions. The results reproduce literature values of the thermal conductivity of Al_2O_3 without the need for an additional thermal interface resistance and therefore Kapitza resistances can be neglected. In addition, the influence of an erroneous substrate thermal conductance requires attention. Fig. 3.13 displays the thermal conductance of a YIG/GGG thin film sample (chapter 6) and the influence of a 1% and 10% error in the substrate thermal conductivity. The data points at $x = 1.01$ and $x = 1.10$ show that the difference in substrate thermal conductance between 1% and 10% error is substantial in particular in the vicinity of the maximum of the thermal conductivity, but negligible otherwise. The solid lines represent the relative change with respect to the original substrate thermal conductivity. While an uncertainty of one percent results in a relative change of less than 2% in the film thermal conductivity, a change by 10% in the substrate thermal conductivity

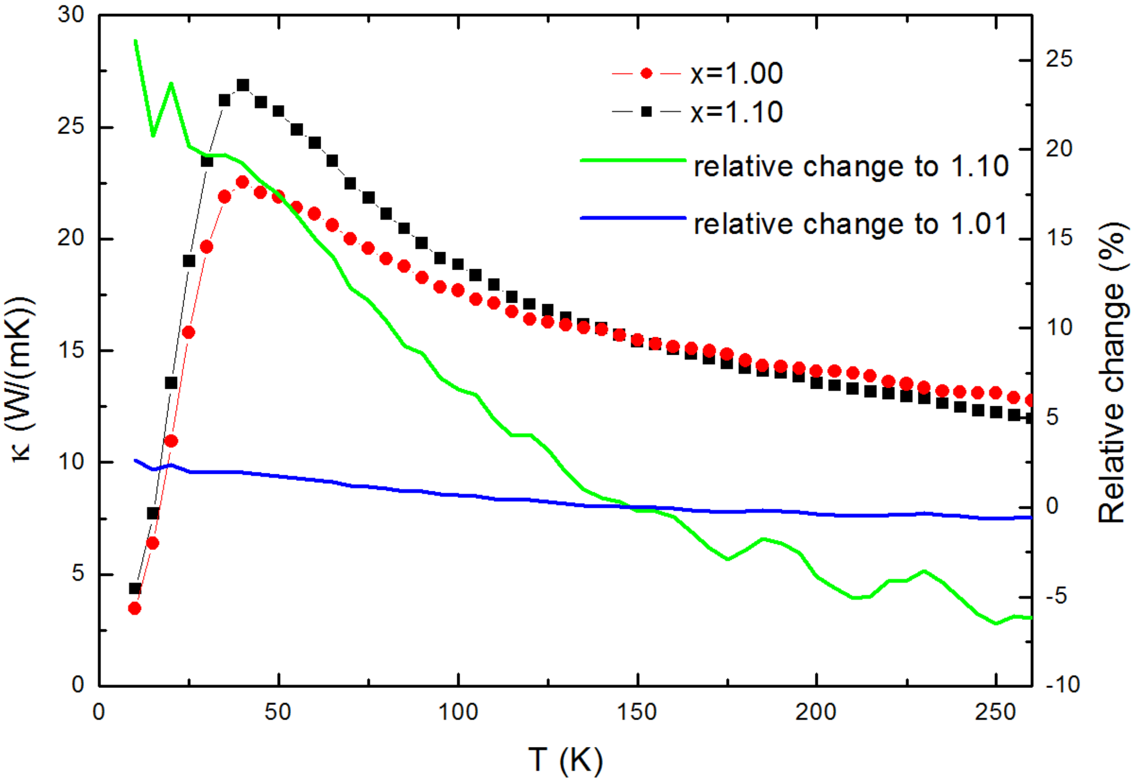

Figure 3.13.: Influence of erroneous values of the substrate thermal conductivity. The red circles correspond to the thermal conductivity of a YIG film on a GGG substrate with a certain thermal conductivity, while the black squares represent that regarding a substrate thermal conductivity increased by 10%. The blue and green solid lines represent the relative change after a manipulation of the substrate thermal conductivity by 1% and 10%, respectively.

causes deviations by more than 25% at low temperatures. As the thermal conductivity of the substrate can be given to approximately 1%, because the slope method is very reliable at high frequencies, a relative uncertainty of at most 3% is to be expected.

The Bayesian algorithm explained in the two previous sections compares measurement data to theoretical calculations taken from the two-dimensional model of heat transport described above. The algorithm is set within a parameter range, which is assumed to cover possible material properties encountered in experiment (Fig. 3.8). The outcome of the algorithm is very stable concerning a modified prior, as altering the ‘previously known thermal conductance’ by 200% leads to changes in the posterior distribution, but after two iterations the difference amounts to less than 5%.

The quality of the resistance balance given by the balance voltage U_{balance} displayed in Fig. 3.12 affects $U_{3\omega}$ in the vicinity of $U_{\mathrm{B}} \approx 2$ mV, where it changes $U_{3\omega}$ by approximately 0.5%. Below and above there is no significant effect. The effect of the balance voltage on U_{ω} is approximately

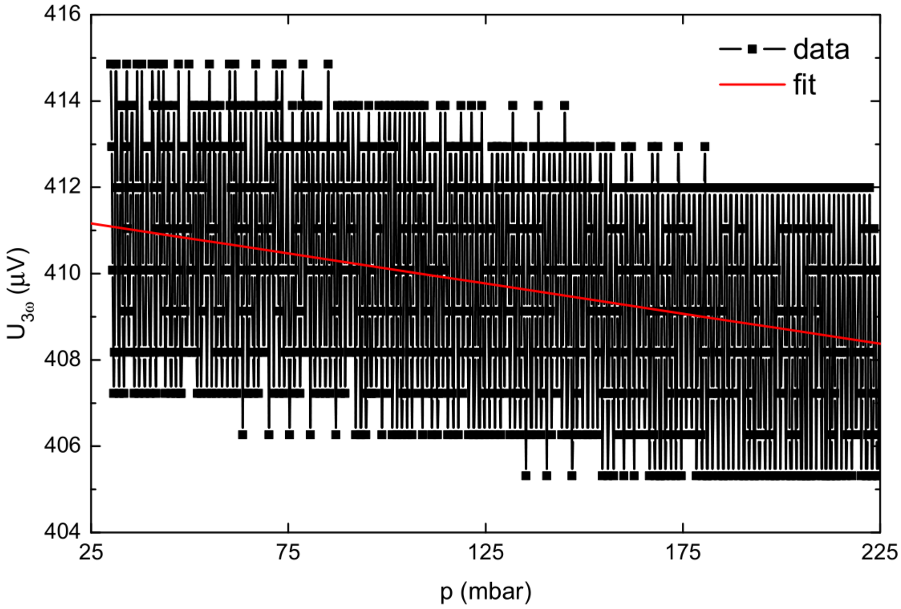

Figure 3.14.: Effect of ambient helium pressure on $U_{3\omega}$.

given by $\Delta U_\omega \approx 0.5\ \frac{\mathrm{mV}}{\mathrm{mV}} |U_{\mathrm{balance}}|$. The reason for the linear dependency of the balance voltage on U_ω is given directly by the layout of the circuit, which acts as a voltage divider between the balance and the sample sub-circuits.

The ambient helium pressure displayed in Fig. 3.14 shows no clear influence on the measurement of the voltage at the 3ω level, even though a systematic trend is apparent. In fact, the scatter seen here is even lower than that seen in the data taken during the experiment determining the accuracy of the determination of voltage ($U_{3\omega}$), which amounts to a relative uncertainty of 1.6% from a sample of 80 data points. Here, a linear fit reveals a slight drift with pressure and a scatter of 1% around the linear fit. The difference between the fit curve value at 225 mbar (408.3 μV) and at 30 mbar (411.1 μV) amounts to 2.8 μV. As the pressure during all measurements never exceeded 110 mbar and never dropped below 40 mbar, it follows that any pressure change during the measurement leads to a non-significant deviation in $U_{3\omega}$ and causes a maximum systematic uncertainty of 0.5%.

The resistance of the heater is linear with temperature between room temperature and 50 K. Exemplarily, Fig. 3.15 shows the evolution of the temperature dependent resistance between 265 K and 235 K. Linear fitting yields $\frac{dR}{dT} = (0.07953 \pm 0.00176)\frac{\Omega}{\mathrm{K}}$, i.e. an uncertainty of the temperature coefficient of resistance of $\frac{\Delta\frac{dR}{dT}}{\frac{dR}{dT}} \approx 2.2\%$. From this slope it is possible to extract the scatter around the linear dependency as an error estimate for the resistance itself. The standard deviation around the linear dependency implies a relative uncertainty of less than 1% over the temperature range down to 25 K. The linear dependency of the resistance on the

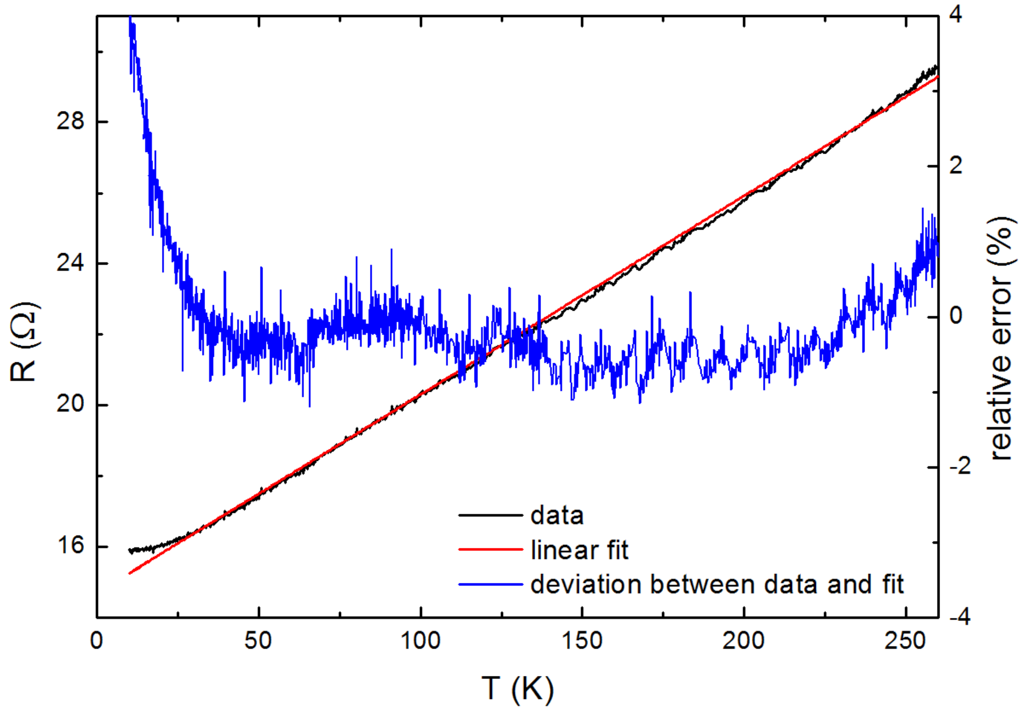

Figure 3.15.: Linear relation of resistance and temperature of the heater structure (data: black line, fit: red line). The blue line represents the relative error of the data with respect to the linear fit.

sample temperature leads to an uncertainty of the resistance that is calculated by Gaussian error propagation to

$$\Delta R = \sqrt{\left(T\Delta\frac{dR}{dT}\right)^2 + \left(\frac{dR}{dT}\Delta T\right)^2 + (\Delta R_0)^2}. \tag{3.42}$$

Error propagation for Eq. 3.21 and Eq. 3.23 results in

$$\Delta(\Delta T) = \Delta T\sqrt{\left(\frac{\Delta\frac{dR}{dT}}{\frac{dR}{dT}}\right)^2 + \left(\frac{\Delta R}{R}\right)^2 + \left(\frac{\Delta U_{3\omega}}{U_{3\omega}}\right)^2 + \left(\frac{\Delta U_\omega}{U_\omega}\right)^2}; \tag{3.43}$$

$$\Delta\kappa = \kappa\sqrt{\left(\frac{\Delta P}{P}\right)^2 + \left(\frac{\Delta d}{d}\right)^2 + \left(\frac{\Delta(\Delta T_{\text{film}})}{\Delta T_{\text{film}}}\right)^2}, \tag{3.44}$$

with $\frac{\Delta(\Delta T_{\text{film}})}{\Delta T_{\text{film}}} = 2\frac{\Delta(\Delta T)}{\Delta T}$ and $\Delta P = P\sqrt{\left(\frac{2\Delta U_\omega}{U_\omega}\right)^2 + (\Delta R)^2}$.

The relative error introduced by the power term amounts to 0.5 to 1% at low (< 100 K) and high (> 200 K) temperatures, respectively, and leads to a relative uncertainty of the temperature oscillation of between 2 and 4% and a relative uncertainty of the thermal conductance of between 3 and 6% in the respective temperature regimes. Using longer integration times and higher sampling rates the uncertainty is further reduced to below 1% (chapter 5).

CHAPTER 4

MAGNETOTHERMAL RESISTANCE PERPENDICULAR TO THE FILM PLANE

In the 1950s, the calcium doped lanthanum manganites La$_{1-x}$Ca$_x$MnO$_3$, x being the doping fraction, drew considerable attention due to their unusually strong resistance changes in the presence of a magnetic field (Fig. 4.1). These so called colossal magnetoresistive properties (CMR, e.g. Jin et al. (1994), Ramirez (1997)) are accompanied by a transition from a ferromagnetic to a paramagnetic state. The physical origin of the CMR and the magnetic phase transition was unclear until the late 1990s, when new experimental insights allowed a deeper understanding of the phenomena within the material class. In particular, an explanation of the transport properties is possible in a setting of strong electron-lattice coupling and the phase diagram in terms of doping (Schiffer et al., 1995, Westerburg et al., 1999b). In the case of $x = 0.33$ the compound displays a metal-insulator transition at $T_{\mathrm{MI}} = 230$ K and a ferromagnetic-to-paramagnetic phase transition at the slightly higher Curie temperature T_C (for a thorough review of the transport properties see Bebenin (2011)). The reason for these almost coinciding phase transitions lies within the temperature dependent interactions between the Mn atom in the center of the unit cell, the oxygen octahedron surrounding it, and the neighboring Mn atoms. The interaction causes a dynamic interplay between the spin state of the Mn atom and the degeneracy of the conduction band (for reviews see e.g. Ramirez (1997), Salamon and Jaime (2001)). These interrelations have consequences concerning the crystal structure. Finally, epitaxial strain adjusts the shape of the crystal structure and can lead to changes in the transition temperature and in the magnitude of the CMR (Siwach et al., 2006). These concepts are discussed in more detail in section 4.1.

The simultaneous electrical and magnetic phase transitions observed in CMR materials are controlled by electron-phonon coupling (Moshnyaga and Samwer, 2011), which makes the material class interesting concerning research on thermal transport. While the magnetoresistive transport mechanism is well understood in single crystalline thin films, the magnetocaloric implications are not extensively studied, since e.g. Visser et al. (1997) solely studied polycrystalline manganites. The CMR effect is usually expressed as a magnetoresistive value and can be defined as $\mathrm{CMR} = \frac{R_{\mathrm{B}=0} - R_{\mathrm{B}\neq 0}}{R_{\mathrm{B}\neq 0}}$. This definition yields positive values that can be larger than 100%.

The CMR effect should contribute to the thermal conductance, since any change in electric resistivity provokes an adjustment of the electronic contribution to the thermal conductivity by virtue of the Wiedemann-Franz law. This effect is in the following termed magnetothermal resistance (MTR) and is defined in analogy to the CMR as the ratio between thermal conductances κ to

$$\mathrm{MTR} = \frac{1/\kappa_{\mathrm{B}=0} - 1/\kappa_{\mathrm{B}\neq 0}}{1/\kappa_{\mathrm{B}\neq 0}} = \frac{\kappa_{\mathrm{B}\neq 0} - \kappa_{\mathrm{B}=0}}{\kappa_{\mathrm{B}=0}}. \tag{4.1}$$

The heat conductivity is usually decomposed in a phononic and an electronic contribution as $\kappa = \kappa_{ph} + \kappa_e$. For the latter in simple metals the Wiedemann-Franz law, Eq. 2.11 is valid, i.e. the electronic thermal conductivity is in this case expected to relate to the electrical conductivity σ, the specific resistivity ρ and the temperature T as

$$\frac{\kappa}{\sigma} = \kappa_e \rho = L_0 T. \tag{4.2}$$

Here, the Lorenz number L_0 is assumed to be constant with temperature as was originally expected from Drude theory (see section 2.1). In order for the Wiedemann-Franz law to be valid the electron scattering processes that reduce the electrical conductivity need to be largely elastic, which is an assumption not necessarily fulfilled for materials with strong electron phonon coupling such as doped perovskites. Additionally, the mechanism of conductivity changes at the metal-insulator transition from metallic at low temperatures to thermally activated at high temperatures, so that the applicability of the Wiedemann-Franz relation is questionable in general. Furthermore, the Wiedemann-Franz relation is not fulfilled in the vicinity of the Debye temperature, which, however, lies at approx. 400 K (Okuda and Tomioka, 2000) and therefore outside of the measurement realm considered here. Nevertheless, the Wiedemann-Franz law provides the most commonly used relation between electronic thermal and electrical conductance and since it clearly demonstrates deviations from free-electron behavior, it was chosen to apply this relation for the discussion in spite of its deficiencies.

While the decrease of the electrical resistivity, the CMR, can be of the order of several hundred percent (Westerburg et al., 1999b), the size of MTR is limited by the phononic contribution to the thermal conductance. As the latter can by far exceed the electronic part (Salamon and Jaime, 2001) an effect on the thermal conductance caused by the CMR is potentially difficult to measure. Despite this, strong electron-phonon coupling should influence the phononic

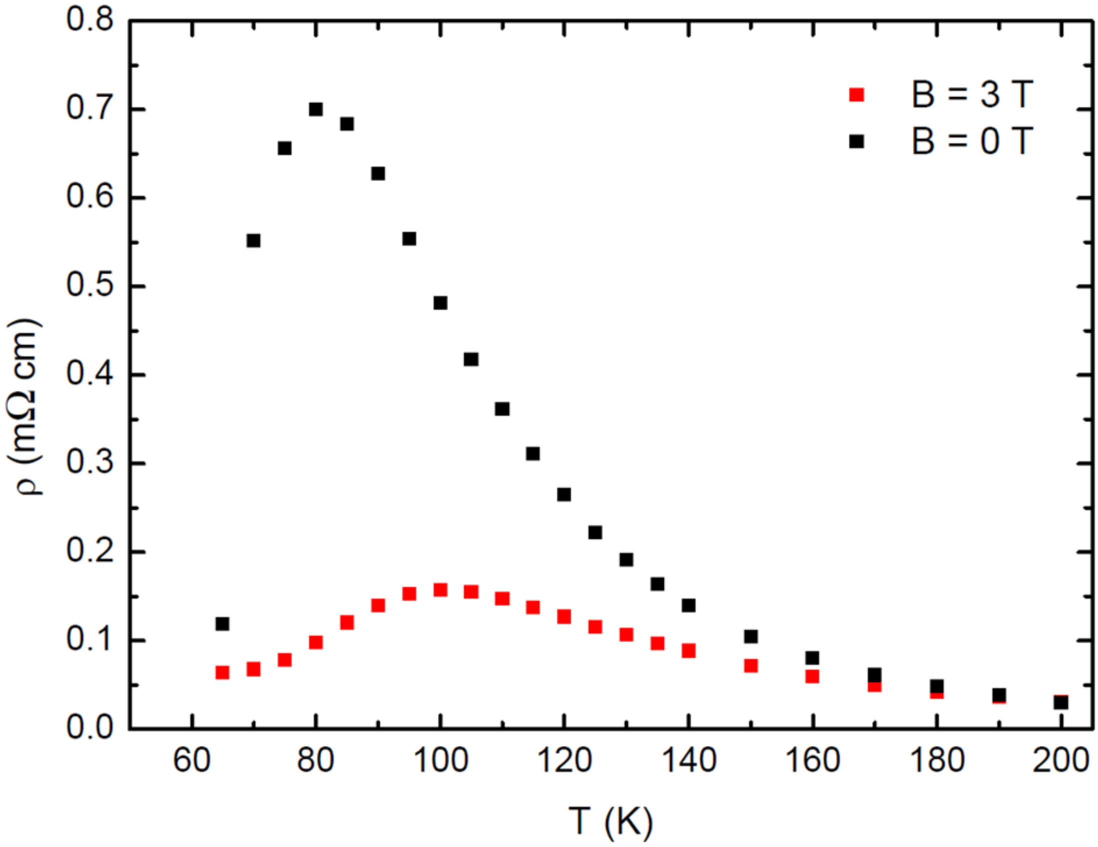

Figure 4.1.: Electrical resistivity of an as-grown $400\ \mathrm{nm}$ thick LCMO sample as a function of temperature for magnetic fields of 0 T (black squares) and 3 T (red squares). The resulting maximum magnetoresistance amounts to approx. 700%.

contribution and therefore increase the MTR above the Wiedemann-Franz expectation (Visser et al., 1997) and thus allows interesting research on a magnetic field mediated manipulation of the phonon structure.

This chapter presents research carried out on the influence of a magnetic field on the thermal conductance of $La_{0.67}Ca_{0.33}MnO_3$ (LCMO). It is discussed why such an effect is to be expected due to the interrelation between thermal and electrical transport and it is demonstrated that the measured quantity by far exceeds the expectations based on a simple model. The first section goes into detail and systematically defines the concepts mentioned in the introduction. Furthermore, in the first section relevant previous research conducted on LCMO is then reviewed to allow a better understanding of the results. The second section briefly introduces the applied deposition and characterization techniques before describing the deposition process of LCMO and the characterization of the material. Using the differential 3ω technique the low-temperature out-of-plane thermal conductance of heteroepitaxial thin film LCMO is measured. Results

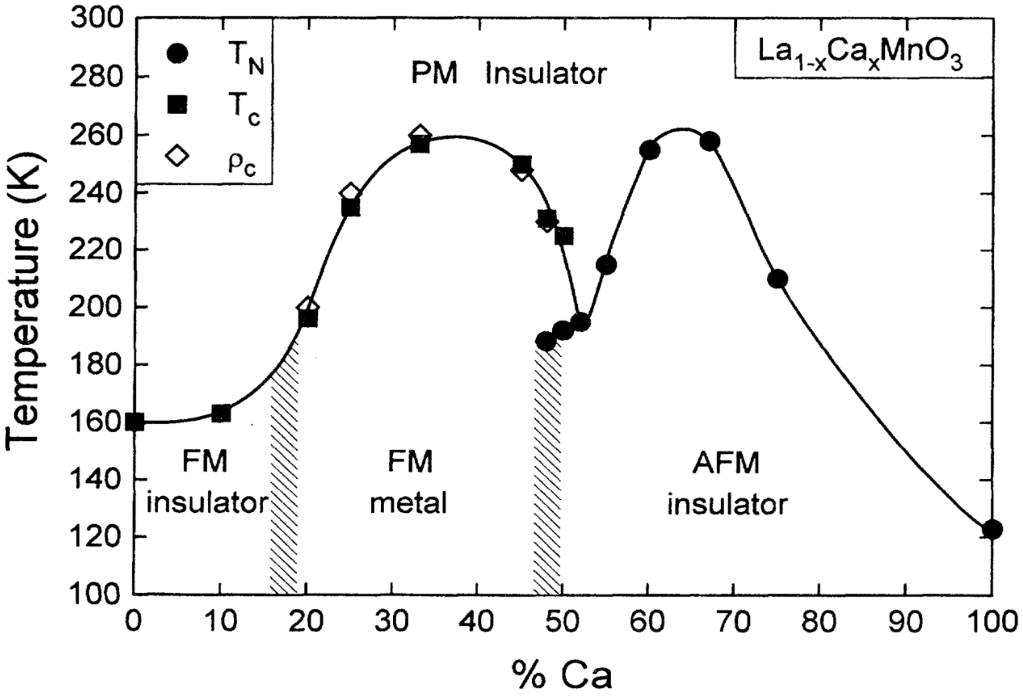

Figure 4.2.: Phase diagram of $La_{1-x}Ca_xMnO_3$ based on Schiffer et al. (1995). The denominations PM, FM and AFM abbreviate paramagnetic, ferromagnetic and antiferromagnetic, respectively. Reprinted figure with permission from Schiffer et al. (1995). Copyright 1995 by the American Physical Society.

are presented in the third section of this chapter. The final section of the chapter discusses an interpretation of the results by means of Raman spectroscopy. Parts of this chapter were published as publication [P2].

4.1. The Colossal Magnetoresistive Manganite LCMO

This section introduces the material $La_{0.67}Ca_{0.33}MnO_3$ (LCMO) and the parent compounds, $LaMnO_3$ (LMO) and $CaMnO_3$ (CMO) in more detail. The section describes structure and electronic transport and gives an overview of the phenomenology of LCMO.

The colossal magnetoresistance (CMR) is defined as a negative, isotropic magnetoresistance (Jonker and van Santen, 1950), which can display resistance changes by up to 127,000% at 77 K or 1,300% at room temperature in a magnetic field of 6 T in LCMO (Jin et al., 1994). The CMR is seen in rare-earth doped manganites $Re_{1-x}A_xMnO_3$ (Re-site: rare earth elements such as La, Nd or Pr; A-site elements: Sr, Ca, Ba, Pb; x is the doping concentration; Paranjape and Raychaudhuri (2002)). These materials possess a strong correlation between the spin, charge and orbital degrees of freedom (Moure and Peña, 2013). In the following this interaction will be explained at the example of LCMO by the trivalent and divalent natures of rare earth elements and the A site atoms, respectively. The charge exchange between the tri- and divalent sites causes the magnetoresistance effect through the spin-alignment dependent double exchange (Zener, 1951).

Phenomenologically, the strongest effect in Ca doped $\mathrm{LaMnO_3}$ is seen between Ca doping levels of $x = 0.2$ and $x = 0.4$ (Schiffer et al., 1995, Ramirez, 1997). Interestingly, the CMR transition is accompanied by a simultaneous phase transition between a ferromagnetic metallic and a paramagnetic insulating phase. Other phase transitions, such as charge ordering or structural transitions, are additionally possible (Moshnyaga and Samwer, 2011), but are beyond the scope of this thesis. This variety of states eventually gives rise to a rich phase diagram of LCMO (Fig. 4.2).

Transitions between the phases can be controlled by changing the charge carrier density by chemical doping, laser excitation, by electrical fields (Moshnyaga and Samwer, 2011) and by oxygen isotope effects (Zhao et al., 1996). The latter shift $\mathrm{T_C}$ by $21\mathrm{K}$ towards lower temperature by using $\mathrm{O_{18}}$ instead of $\mathrm{O_{16}}$ in $x = 0.8$ LCMO; the isotope effect, however, was negligible in $\mathrm{SrRuO_3}$, which has negligible Jahn-Teller effect, which led to the conclusion that the Jahn-Teller effect and the oxygen environment are strongly linked (Zhao et al., 1996). This information will prove useful in the discussion of experimental data in the following sections. A-site substitutions and doping, as utilized in this project, manipulate T_{MI} via the ionic radius and therefore the shape of the unit cell (Moshnyaga et al., 2006), as will be explained in more detail following Eq. 4.3. A second factor influencing phase transition temperatures, that competes with the Jahn-Teller effect, is chemical disorder through statistical distribution of the divalent (Ca) cation between the A sites, which is enhanced for large cations (La or Ba) (Moshnyaga and Samwer, 2011).

The physical origin of these simultaneous phase transitions was under debate until the Jahn-Teller effect (Jahn and Teller, 1937, Ruch and Schönhofer, 1965) was brought into context with the theory of double exchange (Zener, 1951).

The double exchange mechanism is now explained at the example of $\mathrm{La_{1-x}Ca_xMnO_3}$ (see Fig. 4.3). The doping concentration x gives rise to a relative abundance of $\mathrm{Mn^{3+}}$ to $\mathrm{Mn^{4+}}$, as La and Ca are tri- and divalent. The double exchange model assumes that electron transport is facilitated by the oxygen atoms within the crystal (see Fig. 4.4 for the unit cell structure). Assume that initially the electronic configuration is $\mathrm{Mn^{3+}}$ $\mathrm{O^{2-}}$ $\mathrm{Mn^{4+}}$ so that there is a single electron located at the $\mathrm{Mn^{3+}}$. If then an electron moves from the $\mathrm{O^{2-}}$ to the $\mathrm{Mn^{4+}}$, the oxygen changes into a $\mathrm{O^{1-}}$ state and the manganese atoms both are in an (itinerant) $\mathrm{Mn^{3+}}$ state. An electron of the initial manganese atom is then occupied by the oxygen atom causing it to return to the $\mathrm{O^{2-}}$ state, while the manganese returns to the $\mathrm{Mn^{4+}}$ state. By virtue of Hund's

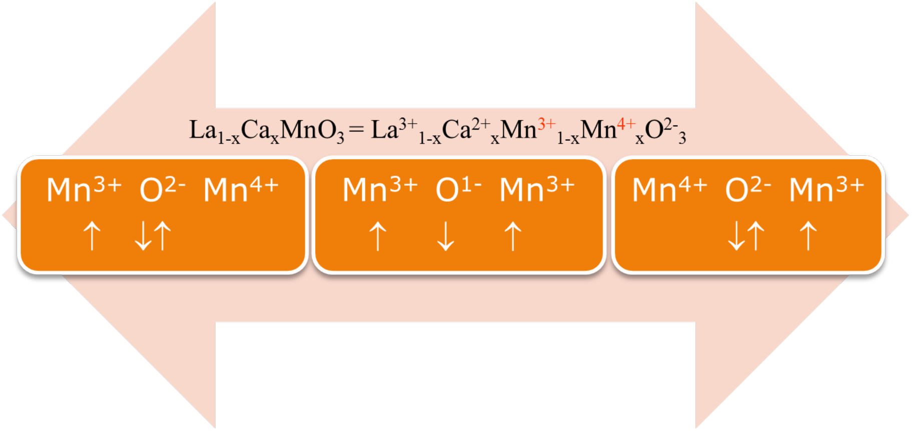

Figure 4.3.: Illustration of the double exchange mechanism by the example of $La_{1-x}Ca_xMnO_3$.

rules[1] this transition is greatly facilitated, if the manganese spins are aligned, which is the case in the ferromagnetic state of the material. Therefore, electronic conduction is associated with spin order, as it is the case, if the aligned state is artificially introduced by an external magnetic field. Thus, a magnetic field leads to reduced resistivity, that is, negative magnetoresistance. Phrased differently, the strong spin coupling within the 3d shells leads to charge transfer given a non-zero parallel component of the ion spins. Thus, a magnetic field or ferromagnetic coupling favor electron delocalization and thereby lowers resistivity (Jakob et al., 1998a).

However, double exchange alone cannot explain the CMR, and a second mechanism, the cooperative Jahn-Teller effect, is required. Its description is closely linked to the research on the ferromagnetic Curie temperature within the perovskite and thereby the crystal structure of the material, so that, before introducing the Jahn-Teller effect, the crystal structure and generic properties of LCMO will briefly be introduced. The perovskite stoichiometry is described by the expression ABO_3, where atoms of type B are located in the center of the unit cell and are surrounded by an octahedron of oxygen atoms, and those of type A are located in the corners of the pseudo-cubic unit cell (Fig. 4.4). $LaMnO_3$ and $CaMnO_3$ generally are electrical insulators, but doping can cause interesting effects in terms of electrical and magnetic properties, which is evident from a rich phase diagram in terms of doping. The material class was first studied by Jonker and van Santen in 1950 who showed that different perovskite oxide samples with

---

[1] The Hund's rules are:

1. The total spin S has the largest possible value permitted by the Pauli principle.
2. The orbital angular momentum L adopts the maximum value permitted under consideration of the first rule.
3. The total angular momentum J is equal to $|L - S|$, if the shell is less than half filled, equal to S when half filled and $L + S$ otherwise.

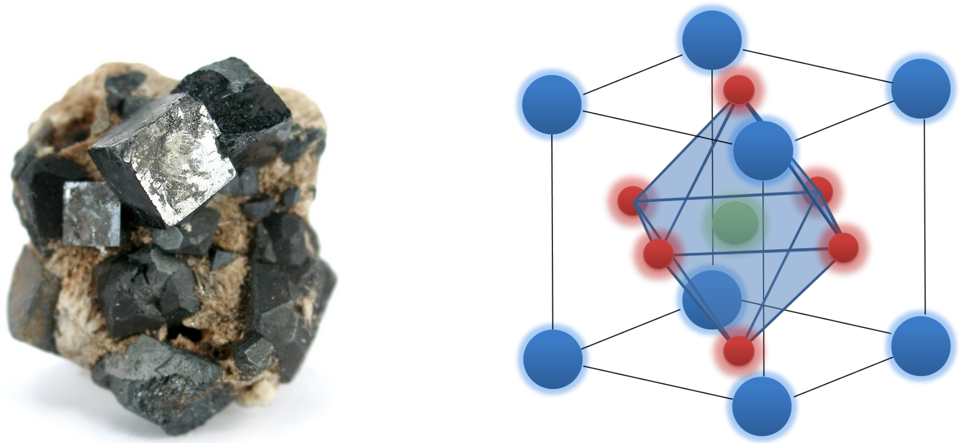

Figure 4.4.: Left: $CaTiO_3$ perovskite crystal found in Magnet Cove, Hot Spring County, Arkansas (USA) (Wikimedia, 2015). Right: Perovskite crystal structure. The blue circles depict atoms located at the A site (e.g. La or Ca), the red circles correspond to oxygen atoms and the green atom at the center of the unit cell corresponds to an atom at the B site (e.g. Mn).

different doping, but identical lattice constants had different Curie temperatures T_C. Their experiments demonstrated that the magnetic exchange interaction was not sufficient to explain the value of the ferromagnetic Curie temperature. An improved explanation was given by an analysis of the Mn-O-Mn bond angle parametrized by the Goldschmidt tolerance factor

$$t = \frac{r_A + r_O}{r_B + r_O}\sqrt{2}\,, \tag{4.3}$$

which relates the effective radii of atoms in A and B positions, r_A and r_B, respectively, and the oxygen atom radius r_O to the distortion of the crystal. A cubic crystal is characterized by a tolerance factor of $t = 1$, and the Mn-O-Mn bond angle consequently is reduced, as the tolerance factor is decreased. Accordingly, an increased distortion through a change of the ionic radii implies a decreased t, and the resulting strength of the electron-phonon coupling then is proportional to $1 - t$ (Moshnyaga and Samwer, 2011). The structure of a manganite can in principle be classified by the tolerance factor into large cations (La,Ba) or (La,Sr) ($0.98 < t < 1$), middle-size cations (La,Ca) or (Nd,Sr) with $0.96 < t < 0.98$ and small cations (Pr,Ca) with $t < 0.96$. $La_{1-x}Ca_xMnO_3$ is almost cubic (with a theoretical tolerance factor of one) for a doping of $x = 0.33$ (Paranjape and Raychaudhuri, 2002). Since also the parent compound of LCMO, $LaMnO_3$, is a perovskite crystal, the atoms within a unit cell are ordered in Mn-O layers separated by La-O layers (or Ca-O layers in the case of Ca doping) and the structure is distorted by doping of the crystal with Ca (Jin et al., 1994, Moshnyaga et al., 2006).

In $LaMnO_3$ crucial electronic properties are given by the half-filled $3d$ bands. Large Coulomb repulsion therein leads to a Mott-Hubbard insulating[2] ground state (Moshnyaga and Samwer, 2011). Doping furthermore manipulates the MnO_6 superstructure by creating Mn^{4+} ions[3]. In a crystalline environment, the energy levels are split and form the crystal field split e_g and t_2g levels (Fig. 4.5). The subscript 'g', which occurs in contrast to the subscript 'u' (from German 'gerade', even, and 'ungerade', odd), is assigned to an orbital, if it is symmetric, or antisymmetric, respectively, with respect to inversion symmetry. Since the electronic configuration of LMO is [Ar]$3d^4$, according to Hund's rules the electrons populate t_2g levels and possess parallel spins. However, if the electronic configuration caused by Mn^{3+} ions leads to an additional electron, it can be either included as an opposite spin electron in the t_2g level at the cost of Hund's rule energy or with parallel spin in the e_g level. In the case of LaMnO_3 and CaMnO_3 the latter is energetically favored.

Nevertheless, in an octahedral environment a priori it is unclear which e_g state is to be populated. According to the Jahn-Teller theorem the crystal is unstable against distortion (Jahn and Teller, 1937). The theorem states that a molecule that possesses a degenerate electronic state is geometrically unstable, unless the atomic configuration is collinear, or the degeneracy is described by Kramer's theorem (Kramers, 1930). Kramer's theorem in turn states that every energy level is at least twice, and in any case even numbered, degenerate in a time-reversal symmetric environment with half-integer total spin, e.g. in a magnetic field free environment. In LCMO, this therefore causes a geometrical instability due to the half-filled $3d$ (half-integer spin) orbitals and their Coulomb interaction. In the case of cubic manganites this distortion is realized by an elongation by a factor of 2α in z direction and of α in the x and y direction, thereby leading to a Coulomb preferred state and degeneracy-lifted bands $d_{x^2-y^2}$ and d_{z^2}. This distorting Jahn-Teller effect is phenomenologically understood by the overlapping orbitals, since neighboring manganese atoms share the intermediate oxygen atom. In order to overcome the repulsive Coulomb force, the oxygen octahedron is shrunk in the plane and elongated perpendicular to it.

The Jahn-Teller distortion finally lowers T_MI depending on α by lowering the energy of the system by

$$E(\alpha) = -A\alpha + \frac{B\alpha^2}{2} \tag{4.4}$$

with A and B constants. The first term represents level splitting caused by the perturbation

---

[2] In the electronic band model electrons are considered to move independent of each other in a periodic (Bloch) potential. As, however, electrons are subject to mutual Coulomb repulsion, the potential an electron is exposed to changes so that electrons no longer move freely, but are localized. (Czycholl, 2008)

[3] The material then actually cannot be called manganite any longer, because that term is only valid for 100% Mn^{3+} ions. However, as manganite is commonly used in cases deviating from this rule, the term is understood as a generalization in the following.

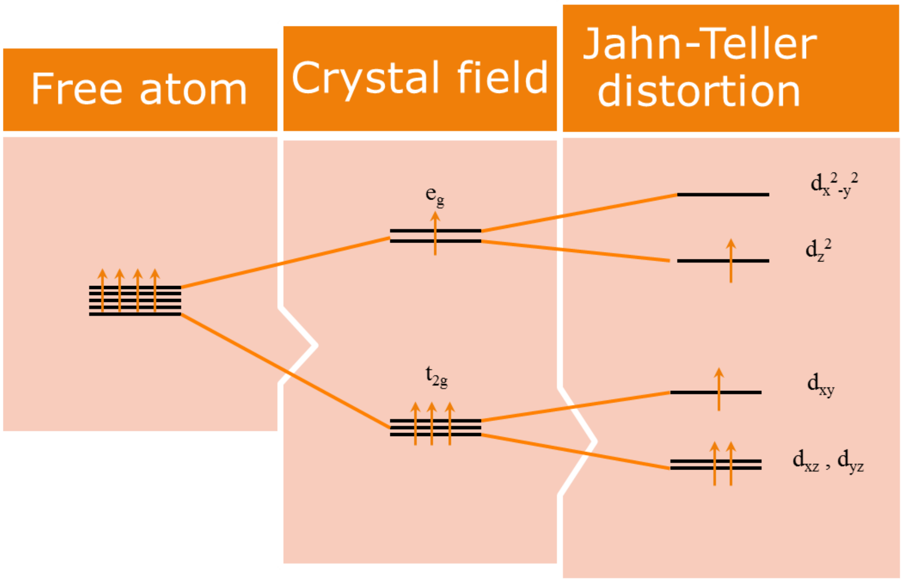

Figure 4.5.: Crystal field effect on the electronic energy levels in La^{3+}Mn^{3+}O$_3^{2-}$ leading to a degeneracy in the e$_g$ orbitals, which is lifted by the Jahn-Teller distortion, i.e. an elongation in the z direction. The states e$_g$ and t$_{2g}$ are degenerate in the middle section ('crystal field') and their splitting is only shown as a simplification.

and the second term elastic (harmonic) deformation energy. If a large number of Jahn-Teller elongated unit cells are considered, they are no longer energetically independent. The filled 3d$_{z^2}$ orbitals then form an energetically favored zig-zag pattern in the $x-y$ plane leading to an expansion of the a_0 and b_0 unit cell vectors by the cooperative Jahn-Teller effect. A number of other distortions are possible and will be introduced in section 4.4.

As explained above, the physical properties of the manganites, and in particular the behavior of resistance with temperature, are generally caused by the presence of a mixed-valence Mn atom in the center of the unit cell, which occurs as Mn^{3+} and Mn^{4+}. The Mn^{4+} content is given by the La and Ca stoichiometry (Salamon and Jaime, 2001). Within a large range of Ca doping, LCMO is semiconducting at a high resistance above a metal insulator transition temperature T_{MI} and metallic below (Jin et al., 1994). For $T < T_{\mathrm{C}}$ the resistivity behaves as $\propto T^{4.5}$ due to electron-magnon scattering. A better fit is given by $\rho(T) = \rho_0 + \rho_1 T^{4.5} + \rho_2 T^2$, where ρ_i are constants. The last term is introduced for electron-electron scattering (Westerburg et al., 1999a,b). There, however, is no linear term.

In the case of $T > T_{\mathrm{C}}$ the resistivity is activated and relies on polarons, which are quasiparticles forming due to local charging effects in a crystal lattice (Jakob et al., 1998a, Salamon and Jaime, 2001). Charge transport is affected particularly, as a moving electron modifies its charge environment because of the Coulomb repulsion of other negative charges. The double exchange mechanism leads to an exponential suppression of the T^2 contribution to $R(T)$ and favors polaronic transport described by $\rho(T) = cT^a \cdot \exp(E_A/k_BT)$ with a and c constants, k_B the Boltzmann constant and E_A the activation energy.

The high temperature region is not simply described by thermal activation, but by nonadiabatic small polaron hopping, while variable range hopping does not describe the data well. Small polaron models are still feasible up to magnetic fields of 8 T, but appear to break down above that field strength. Generally, the transport theory depends strongly on the angle between the cluster of magnetic ions and the paramagnetic ions around, which leads to a cluster size of approximately four ions (Jakob et al., 1998a,b,c).

The magnetoresistive peak caused by the metal-insulator transition on the high temperature side of the resistivity peak lies at a temperature at which the resistance is about half to two thirds of its peak value (Jin et al., 1994). The metal insulator transition temperature T_{MI} differs slightly from the temperature of peak magnetoresistance and is very close to the maximum resistivity temperature (the difference is caused by microscopic inhomogeneities (Salamon and Jaime, 2001)). Hole-doping x and average A-site cation radius are key to control T_{MI} and a doping of $x = 0.2 \ldots 0.5$ is needed to stabilize the ferromagnetic phase (double exchange between $\mathrm{t_{2g}}$ electrons on adjacent Mn ions mediated by $\mathrm{e_g}$ electrons, Fig. 4.3). Rodriguez-Martinez and Attfield (1996) studied samples with $x = 0.3$ and a mean A-cation radius of r but a radius variance σ^2. T_{MI} is largest at small spreads, which imply microscopic homogeneity, and is empirically found to decrease linear with σ^2 until it stays constant at approximately 100 K. Mean field treatment by Röder et al. (1996) gives a similar result for thin films based on the assumption that strain energy changes T_{MI}.

In addition to the experimental perspective, also the theory viewpoint is required to consider the three components charge, spin and orbital degrees of freedom, as theories considering only one of them fail to provide a description that is consistent with data (Salamon and Jaime, 2001). However, a full review of theoretical effort is not required in the scope of this thesis so that the reader is referred to the literature (Zener, 1951, Anderson and Hasegawa, 1955, Holstein, 1959, de Gennes, 1960, Kubo and Ohata, 1972, Varma, 1996).

4.2. LCMO: Deposition and Characterization

Thin films are of interest in materials science not only because of their technological applicability, but even more, because their properties often differ from those of bulk material. This section first introduces to the techniques used to deposit crystalline films with nanometer thickness and secondly to the methods applied to characterize LCMO thin films in the course of this thesis. The second subsection presents the results of the characterization.

4.2.1. Applied Techniques

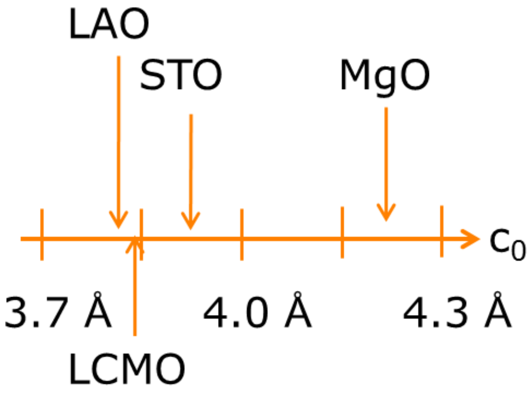

Figure 4.6.: The out-of-plane lattice constants of LCMO and the available substrates, STO, LAO and MGO.

Crystalline thin films with thicknesses of below 1 μm can only be produced on top of a crystal substrate, which possesses - or is close to - the targeted lattice constant so that there is small or no lattice mismatch. If the material is deposited on top of such substrates in single crystalline form, it is termed epitaxially grown. If the film and substrate materials are of identical composition, the sample is termed homoepitaxial, otherwise heteroepitaxial. In particular, in the heteroepitaxial case, the lattice constants of substrate and film usually do not fully agree. Such a lattice mismatch can lead to strain within the film. Unless strain is the matter of interest it is to be avoided by the choice of a suitable substrate, even though it cannot be circumvented completely. Concerning LCMO the substrates $SrTiO_3$ (STO), $LaAlO_3$ (LAO), MgO (MGO), and others are available (Martin et al., 1999, Siwach et al., 2005). Their lattice constants in relation to that of LCMO are displayed in Fig. 4.6.

The thermodynamic deposition environment and material specific properties such as lattice constant, film thickness and others additionally lead to differences in the growth process. The particle nucleation and film forming process have a direct impact on the surface morphology, so that processes such as interatomic diffusion, island growth and layer structuring occur during deposition. In the experiment three growth modes are mainly of interest: van-der-Merwe, Volmer-Weber and Stranski-Krastonov growth (Fukuda and Scheel, 2003, Cai et al., 2013). The van-der-Merwe growth mode is characterized as layer-by-layer growth, so that a new layer is formed after the layer below has fully been completed. This growth mode generally leads to high-quality films with a low defect density and long range order. However, large film thicknesses often lead to dislocations and cracks in the film, especially, if the first layers are strained. Volmer-Weber growth is described by islands, not necessarily of only one atomic layer that grow and gradually merge. Finally, Stranski-Krastonov growth is located in the transitional regime between the previous two growth modes and generally occurs at a large lattice mismatch between film and substrate material. While the first layer is atomically smooth and grows by van-der-Merwe mode, with increasing deposition time Volmer-Weber growth takes over and creates an array of islands on top of a continuous film (Völklein and Zetterer, 2006). The LCMO thin films deposited here the surface morphology was observed by atomic force microscopy (AFM).

Films are generally grown by molecular beam epitaxy (MBE), liquid phase epitaxy (LPE), sputtering, pulsed laser deposition (PLD) and others (Martin et al., 2010). The method of choice for the growth of LCMO thin films here was PLD (Hawley et al., 1997, Martin et al., 1999), which is described in detail by Krebs et al. (2003) and Venkatesan (2014), and only the most important basics are given here. PLD is based on the concept of the interatomic work function. A pulsed laser beam is focused on a ceramic target of the material to be deposited. In the target atoms are fixed into a solid polycrystalline form. The electric field of the laser disrupts the surface, frees atoms from the solid surrounding and thereby produces a plume of free target atoms that moves towards the substrate on which the film is to be deposited. In order to avoid droplets and other large disturbances on the film surface and to erode the target in a controlled and homogeneous manner, the target is rotated permanently and the laser beam scans the target surface.

A major advantage of PLD is almost stoichiometric transfer of the target material to the substrate. Additionally, there is a possibility to heat the substrate to achieve optimal growth conditions and to perform the deposition process in a low pressure atmosphere. In this case, the film deposition was carried out by a 248 nm KrF laser in an O_2 atmosphere with pressures between 0.05 mbar and 0.2 mbar and a pulse rate of 5 Hz at 2 J/cm^2. The substrate was heated by means of a resistive heater block that was able to administer power of up to 140 W, which led to substrate temperatures of up to 800°C.

STO substrates consist of alternating SrO and TiO_2 planes. As LCMO growth proved to be best on TiO_2 terminated substrates (Ohnishi et al., 2004, Mix, 2013), the substrates were preprocessed in a buffered HF solution, to which SrO is particularly sensitive to, and subsequent annealing. The substrates were then glued to a substrate holder by conductive silver. The deposition of films of several hundred nanometers in thickness requires one to two hours. Considering the substrate temperature of 750°C, the conduction silver hardens up to the point at which the substrate cannot be retrieved in one piece. While indium as a replacement of conduction silver was feasible in some cases by exploiting the surface tension in the liquid state, it was difficult to fix the substrate on the holder, since the solid indium could not be distributed on the holder in such a way that in the liquid form adhesion was uniform. Conduction silver mixed with alumina powder proved to be the ideal solution, as its granularity provided a possibility to safely remove the substrate from the holder after the deposition. The film homogeneity was best when the substrate was glued to a copper plate that was attached to the heater in order to minimize temperature gradients on the substrate (see Appendix A). The oxygen stoichiometry is relevant for the magnetic and transport properties of LCMO films (Tripathi et al., 2009, Zhao et al., 2013) and was optimized by annealing in an oxygen atmosphere for two hours at a temperature of 950°C after the deposition at 750°C. Energy dispersive x-ray spectroscopy (EDX) confirmed stoichiometric films after annealing[4].

The crystal quality and thickness of the deposited films were analyzed by their x-ray diffraction (XRD) properties in Bragg Brentano geometry. In XRD, the x-ray source and the detector are positioned on a circle, in the center of which the sample is located. The angle at which the sample is tilted with respect to the incoming x-rays is denoted as ω, while the detector is, as the incident angle is equal to the emergent angle, positioned at $2\theta = 2\omega$. If the sample is now slowly rotated in ω, the incident x-rays are diffracted at different lattice planes of the crystal structure. Interference with the crystal structure causes stronger reflection at certain angles, which are characteristic of the material under consideration. The underlying physical reason is located within the reciprocal space layout of the sample's crystal structure[5], as constructive interference is only possible, if the momentum transfered $\Delta\mathbf{k}$ is equal to a reciprocal space vector $\mathbf{G}$ of the lattice, so that

$$\Delta\mathbf{k} = \mathbf{G}. \tag{4.5}$$

Assuming then that the crystalline planes are aligned in parallel, Bragg's law relating the distance of the lattice planes d_{hkl} and the scattering angle θ is given by

$$2d_{hkl}\sin\theta = n\lambda. \tag{4.6}$$

Here the Miller indices h, k and l denote the crystalline direction in reciprocal space, n is the order of the maximum in intensity and λ the wavelength of the incident x-rays, which is given by 1.5411 Å in the case of the average of the $\mathrm{K}_{\alpha1}$ and $\mathrm{K}_{\alpha2}$ lines of copper.

The sample thickness and roughness are investigated using x-ray reflectivity (XRR), during which the sample is tilted beginning at the angle of total reflection up to several degrees. After the angle of total reflection that depends on the electron density in the sample the intensity rapidly decreases and oscillations are modulated onto the decay due to interference between rays reflected at the interface between substrate and film and those reflected at the sample surface. These oscillations, the so called Kiessig fringes, depend on the electron densities in the film and substrate as well as the film thickness, which allows a precise determination of the thickness, roughness or density of the film.

The magnetic properties of the samples were analyzed by means of a superconducting quantum interference device (SQUID), which is based on one or more Josephson junctions, i.e. two superconductors brought into proximity, but separated by an insulating or metallic layer, so that Cooper pairs can tunnel. The phase difference of both superconductors, when in presence of a magnetic sample, leads to a flux that is an integer multiple of the magnetic flux quantum $h/(2e)$, where h is Planck's constant and $2e$ the charge of a Cooper pair. A DC SQUID consists of a current loop together with two Josephson junction. A magnetic field within the loop caused by the sample leads to a phase change in the junctions. This phase change induces a tunneling current that is indirectly measured as the DC voltage drop across the SQUID. The flux voltage characteristic of a SQUID is periodical with the flux quantum, so that the flux caused by the sample magnetization can be measured.

---

[4] In this technique, that has an information depth of several micrometers, electrons of $10\ldots20$ keV energy are accelerated towards the sample surface and cause x-rays that are characteristic for the material to be emitted.

[5] The reciprocal space is defined as the Fourier transform of the real space structure such that a vector (k,h,l)^T in reciprocal space is perpendicular to a family of lattice planes (hkl).

The transport properties (electrical, magnetotransport and thermal transport) measurements were carried out in a ^{4}He cryostat between 280 K and 4.2 K. A variable temperature insert (VTI) allows the sample temperature to be set with an accuracy of approx. 0.1 K. A superconducting magnet is employed to apply a perpendicular magnetic field of up to 8 T.

4.2.2. Results

The target plays a crucial role in pulsed laser deposition, as the stoichiometry and homogeneity of the polycrystalline material directly affects that of the film. In order to deposit high quality LCMO thin films by pulsed laser deposition the target requires careful preparation, mixing, pressing and sintering. In particular, in order to acquire a LCMO target with a stoichiometry of $La_{0.67}Ca_{0.33}MnO_3$ the constituents originally are available as La_2O_3, $CaCO_3$ and $MnCO_3$ and are mixed, milled and pestled. Before pressing the powder into the cylindrical target shape (diameter: 2.54 cm) the material is sintered at 950°C for 12 hours after a heating rate of 1 K per minute; the cooling process allows higher rates of up to 5 K per minute. A subsequent additional milling step is followed by the pressing step at a pressure of 100 kN/in^2. The target is finalized by a last sintering process at 1350°C for 24 hours. Generally, higher sintering temperature of target leads to improved sample quality in terms of magnetoresistance (Jin et al., 1994) and the temperature of 1350°C represents the highest temperature accessible by the equipment available.

In principle, growth is possible on LAO, STO and MgO (Paranjape and Raychaudhuri, 2002) and on Al_2O_3 (Jakob et al., 1998a). A series of LCMO samples with different thicknesses (25 nm, 100 nm, 200 nm and 400 nm) were grown heteroepitaxially on STO, MgO and LAO substrates in (100) orientation by KrF pulsed laser deposition at a pulse rate of 5 Hz with an energy density of 1.2 J/cm^2. Optimal growth conditions were found at a pure oxygen pressure of approximately 0.1 mbar and substrate temperatures between 850°C and 900°C, for which an increased substrate temperature generally improves the film quality in terms of crystallinity.

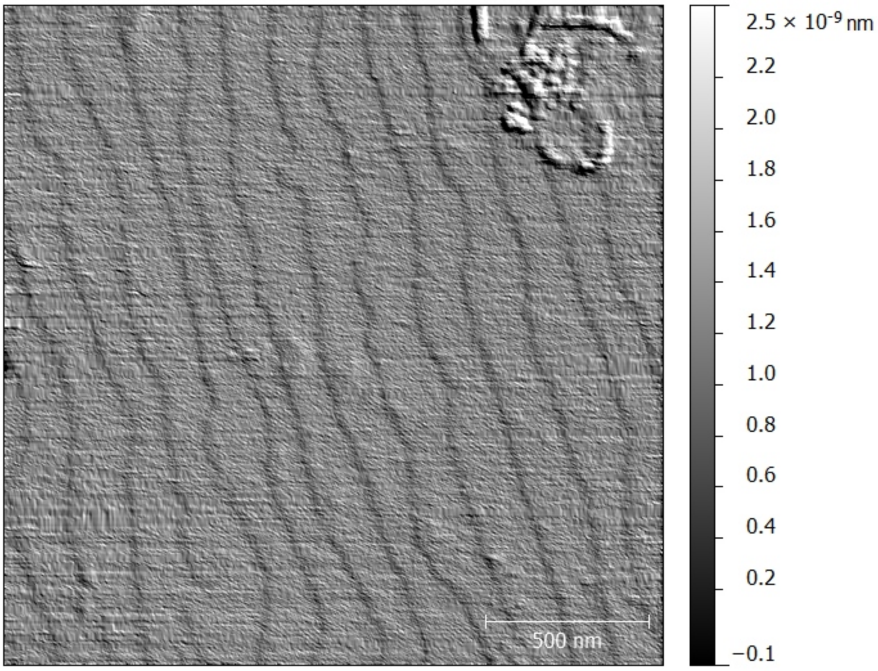

Figure 4.7.: AFM scan of a 400 nm thick LCMO sample grown on STO. Step flow growth mode is clearly visible.

Atomic force microscopy confirmed the high surface quality of the films. Even though, according to Paranjape and Raychaudhuri (2002), step flow growth mode is only observed at thicknesses below 150 nm and island growth above, step flow growth mode is observable in 400 nm thick samples grown on STO (Fig. 4.7), i.e. the film surface reproduces the steps of the substrate surface. The root-mean-square roughness was found to be 0.3 nm corresponding to less than one unit cell. The film crystallites extend over more than the average step size of 200 nm and along the terraces no grains are observable in the AFM scan region.

A high degree of epitaxial growth was demonstrated by an x-ray diffraction rocking curve full width at half maximum of 0.07° of the (002) reflex of a $400\ \mathrm{nm}$ thick LCMO film (top right panel in Fig. 4.8). Thus in-plane grain boundary contributions to the electrical and thermal resistivity are assumed to be negligible. The large intensity peaks in the top left panel correspond to the substrate (002) peak, which is twinned because of the natural splitting of the Cu Kα line, as the transitions from 2p$_{3/2}$ and 2p$_{1/2}$ to the 1s level are possible. The following peak on the large angle side of the substrate peak is the (002) reflex of LCMO.

In order to perform 3ω measurements a gold layer is required on top of the sample film. In the case of electrically conducting films this Au layer is separated from the film by a layer of Al$_3$O$_3$ with a thickness of 200 nm. A thickness of that magnitude is required in contrast to

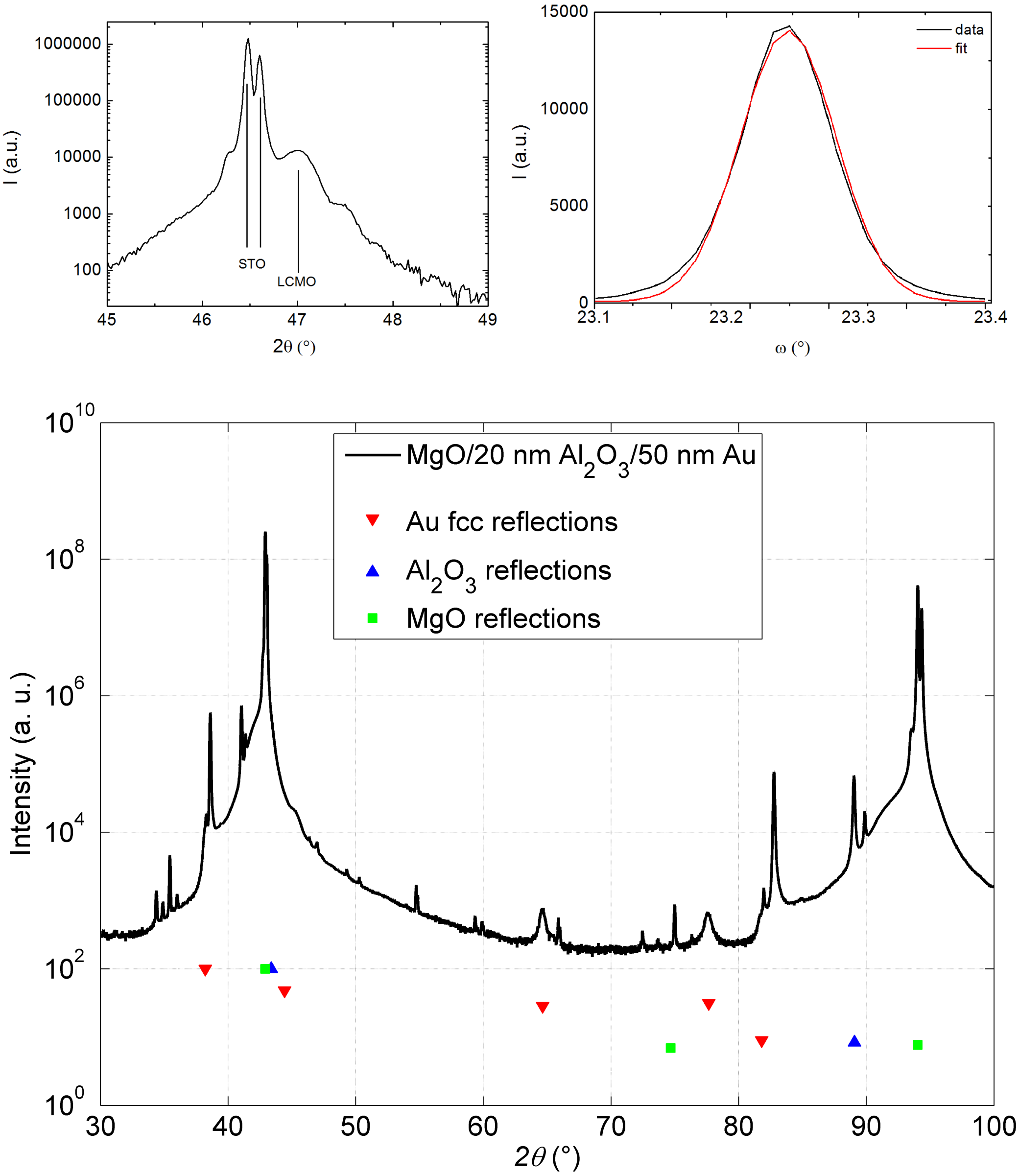

Figure 4.8.: Top: XRD spectrum including the STO substrate peak at 46.5° and the (002) LCMO peak at 47.3° with Laue oscillations on the right side of the peak (left) and rocking curve with a full width at half maximum of 0.07° (right) of the (002) peak of LCMO. Bottom: θ-2θ XRD scan of Al_2O_3 and Au grown on MgO and identified reflections of face-centered cubic (fcc) Au, Al_2O_3 and MgO. The analysis of this scan has been performed by Paulina Hołuj.

TMR tunnel barriers, which are thinner by two orders of magnitude, since the sample area is larger than that of a TMR barrier by several orders of magnitude, so that the probability to encounter a pinhole is increased. In addition, the voltages applied are larger in the 3ω experiment by one order of magnitude. The insulating properties were optimized by carefully

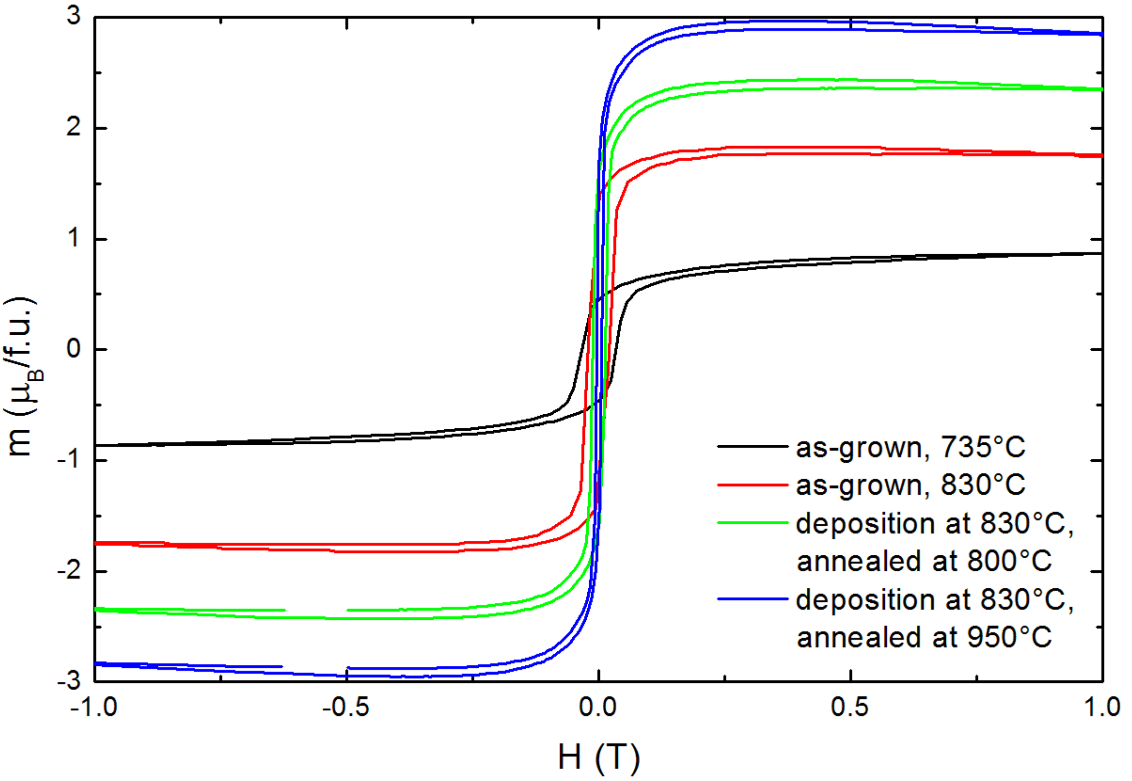

Figure 4.9.: Magnetization hysteresis of as-grown LCMO deposited at a temperature of 735°C (black) and 830°C (red), LCMO grown at 830°C and post-annealed at a temperature of 800°C for two hours (green) and post-annealed at 950°C for two hours (blue). The substrate contributions have been subtracted and geometry factors have been accounted for.

adjusting the stoichiometry by Jäger (2013) and Hołuj et al. (2015). The bottom panel in Fig. 4.8 displays a θ-2θ scan of a sample composed of 50 nm Au on top of 20 nm of Al_2O_3 grown on MgO. The scan demonstrates the crystallinity of the Au and identifies the crystal structure of the gold layer to be fcc. Additional lines related to the substrate caused by Cu K_β and W L_α radiation are visible.

Magnetization measurements using a superconducting quantum interference device (SQUID) allowed an estimation of the Curie temperature and the saturation magnetization of the material (Fig. 4.9). The theoretical saturation magnetization of 3.6 μ_B/f.u. was not reached, but approached (Tab. 4.1). In addition, it was found that while the coercivity of the magnetic material and thus the saturation field strongly decreased with increasing deposition and annealing temperature, the remanence magnetization increased. Further increasing the saturation magnetization would increase the metal-insulator transition temperature to even higher values. This needs to be avoided in the case of the setup available in the present lab, as the equipment is capable of measuring the thermal conductance below 270 K only and the entire transition peak was to be observed. A secondary reason to refrain from any further increase of the Curie temperature is that the thermal conductance measurements would be less sensitive to the electronic contribution, because, according to the Debye model, the dominant phononic contribution increases with T^3. Therefore, in LCMO with a metal insulator transition temperature of 240 K the most precise measurement of the entire transition peak is possible.

Deposition temperature (°C)	T_{MI} (K)	m (μ_B/f.u.)
735	80	0.78
830	100	1.6
800 (post-annealing)	220	2.2
950 (post-annealing)	240	2.7

Table 4.1.: Dependence of the metal-insulator transition temperature T_{MI} and the saturation magnetization per unit cell m on the deposition and, respectively, annealing temperature of a $400\ \mathrm{nm}$ thick LCMO film grown on a STO substrate. The deposition temperature of the post-annealed samples was 830°C. A clear increase in both saturation magnetization and phase transition temperature can be induced by post-annealing at a high temperature in an oxygen atmosphere.

The cryostat used for the thermal conductance measurements is also used to determine the temperature dependent resistance of the samples by a four-point technique. Electrical transport and the CMR is, in addition to the properties mentioned above, determined by transport through grain boundaries; in epitaxial thin films factors determining the grain size are strain, growth mode and microstructure (Paranjape and Raychaudhuri, 2002). As a consequence, the magnetic phase transition temperature and the metal-insulator transition temperature are increased by the quality of the film (Mukherjee et al., 2013). In addition, according to Paranjape and Raychaudhuri (2002), annealing of strain-relaxed (thick) films generally leads to grain growth and enhances the magnetoresistance properties. In order to test this hypothesis, some samples were post-annealed in an oxygen atmosphere at 950°C for two hours to improve oxygen stoichiometry and thereby adjust the metal-insulator transition temperature by altering the bond angle between two oxygen atoms and the intermediate manganese atom (Tab. 4.1). The result is a magnetoresistance of 130% to 700% for high and low metal-insulator transition temperatures, respectively (Fig. 4.1).

The thermal conductance values observed in as-grown LCMO agree in their magnitude with the values obtained for polycrystalline LCMO by Visser et al. (1997) and Fujishiro (2001) and are displayed in Fig. 4.10. The thermal conductance in zero field decreases slightly for decreasing temperatures above the metal insulator transition and increases thereafter. However, in contrast to the data taken in annealed films, the temperature of the minimum of the thermal conductance does not correspond to the metal-insulator transition temperature. This difference propagates into the behavior of the MTR with temperature. In the case of an applied field the

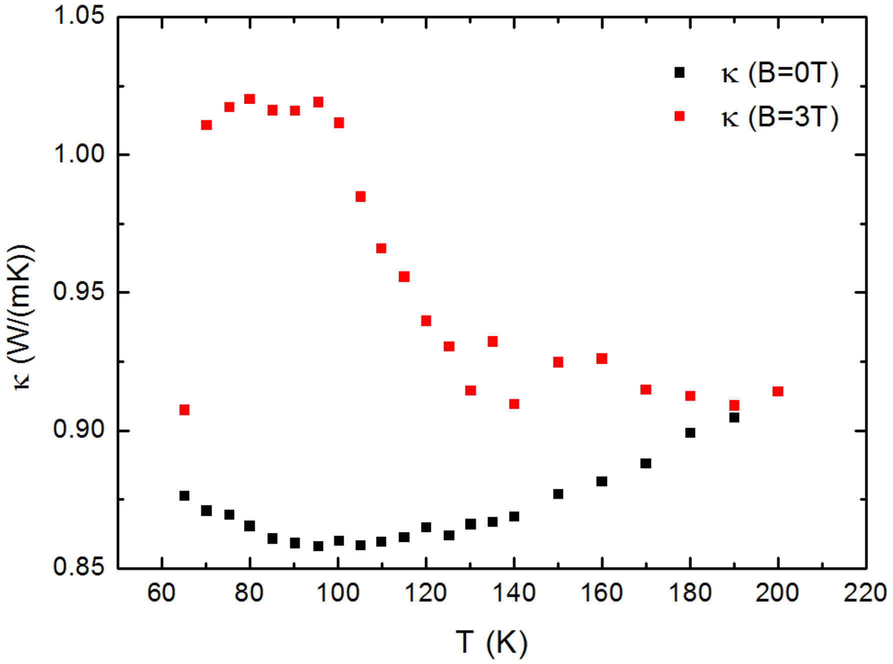

Figure 4.10.: Thermal conductivity as a function of temperature of an as-grown LCMO film of 400 nm thickness grown on STO.

thermal conductance stays constant and then increases to reach a plateau between 100 K and 70 K. In particular, the low temperature plateau is in disagreement with the Wiedemann-Franz law, as it is accompanied with decreasing resistivity. In general, single crystalline films should display a larger thermal conductance than their polycrystalline counterparts, as grain boundary scattering is less dominant. Our observation of a similar magnitude indicates that, compared to bulk material, the small thickness of the LCMO film causes a cut-off of long wavelength phonons at low temperatures.

4.3. Magnetothermal Resistance in LCMO

To continue the study of the magnetic field effect on the thermal conductivity in LCMO, the magnetothermal resistance (MTR), as defined in Eq. 4.1, is studied and brought into experimental context with the CMR. The MTR measured in the as-grown samples on STO reaches a maximum of 19.5% and is displayed in Fig. 4.11. While from 150 K towards lower temperature the MTR decreases, the temperature of maximum MTR remarkably does not correspond to the temperature of the maximum CMR. Instead, the MTR displays a broad maximum between 130 K and 70 K with a steep decline on the low-temperature side in agreement with the CMR behavior. On the high temperature side, the CMR gradually increases up to a rather pronounced maximum at 75 K.

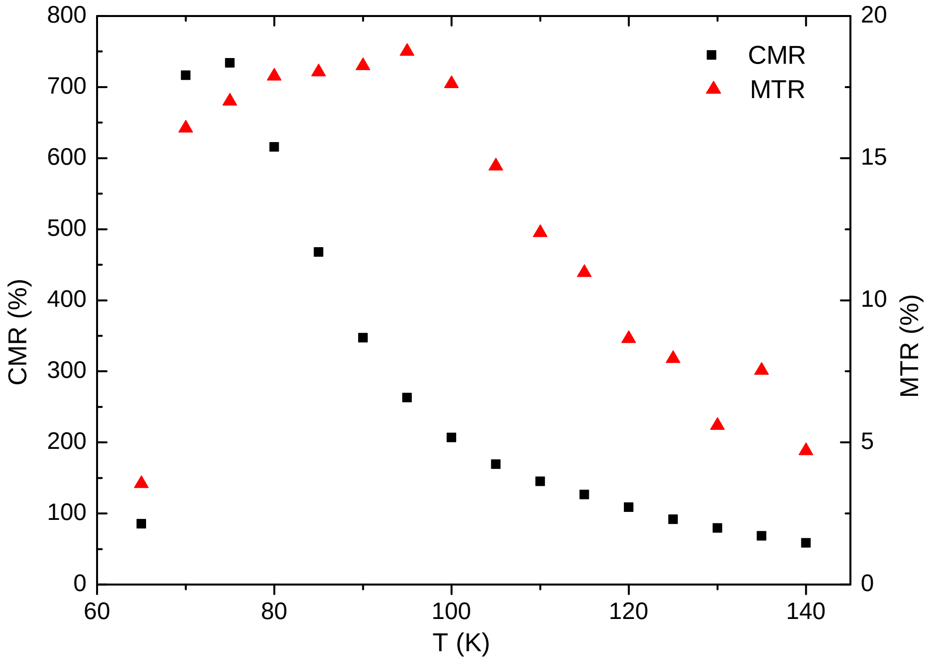

Figure 4.11.: Temperature dependent CMR (black squares) and MTR (red triangles) measured in an as-grown 400 nm thick sample on STO. The peak position of the MTR notably differs from that of the CMR.

In order to understand this phenomenon, the MTR is separated into an electronic (Wiedemann-Franz) and a phononic contribution (the difference between the total MTR and the electronic MTR). The phononic contribution is calculated by subtracting the expected electronic contribution determined from a CMR measurement and the Wiedemann-Franz law from the measured total MTR. The top panel in Fig. 4.12 shows the expected MTR calculated from the Wiedemann-Franz law from the measured CMR and the remaining phononic contribution. The difference in shape between the CMR and the electronic MTR curves originates from the $\kappa\rho \propto T$ relation of the Wiedemann-Franz law, which includes the temperature as a scaling factor. The phononic contribution clearly peaks at approximately 95 K. Generally, the phononic contribution displays values larger than the expected values by almost a factor of four. A possible reason for this much larger than expected effect is the contribution of electron-phonon scattering, as suggested by Visser et al. (1997), who reported similar results for unstrained polycrystalline bulk samples. Such strong electron phonon coupling in manganites is also evident in the electrical transport above the metal insulator transition temperature (Nelson et al., 2001, Jakob et al., 1998a). The following discussion below indicates that the magnetic field can influence the phononic contribution to the thermal conductance and thereby enhance the MTR.

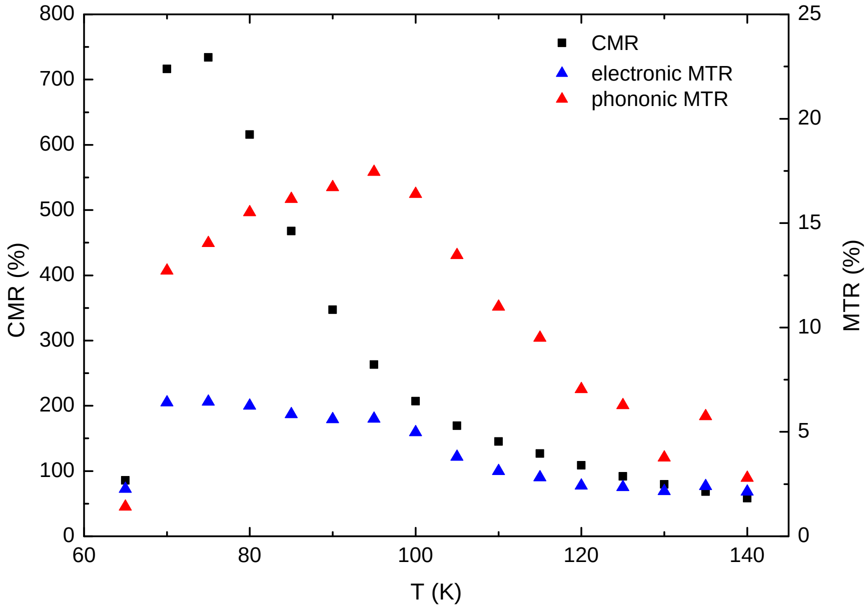

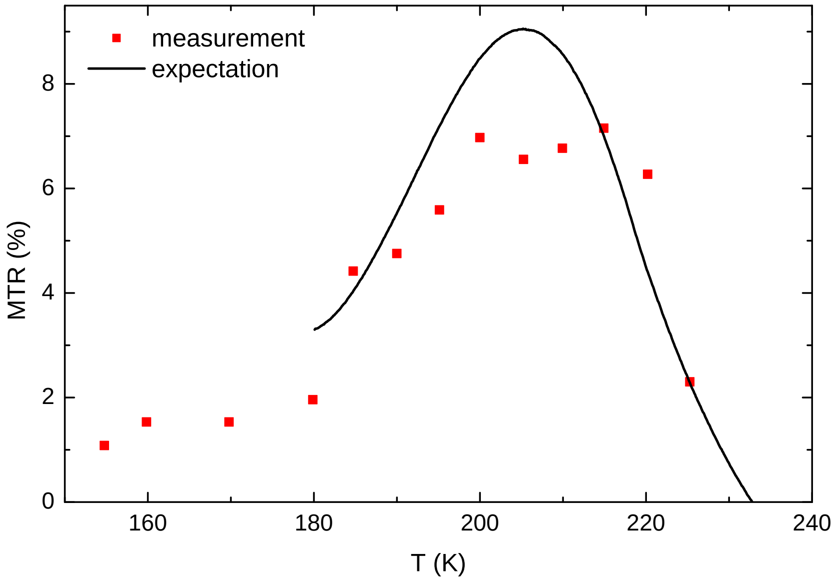

Figure 4.12.: Top: As-grown sample. Temperature dependence of the CMR (black squares) compared to the electronic contribution to the MTR (blue triangles) and the 'phononic' contribution to the MTR. Bottom: Temperature dependent MTR of an annealed sample of 400 nm thick LCMO grown on STO (red squares). Additionally, the expected MTR inferred from CMR data by the Wiedemann-Franz law is displayed (black line).

The assumption that the large effect in the as-grown samples is caused by electron-phonon scattering requires further investigation. Generally, the phonon spectrum of a crystal can be modified by changes in the atomic positions, or their interaction strength. Fig. 4.13 visualizes effects causing strain by their characteristic length scale. While Jahn-Teller distortions and local spin interactions operate on a scale mainly given by the lattice constant, O_2 (off-) stoichiometry is a film-wide phenomenon. Finally, substrate and thickness effects occur on scales of the film thickness and above. The first effect results in strain, which can be either substrate induced or thickness related (relaxation); the second is related to any change in atomic positions or to off-stoichiometry (in the case of LCMO especially to oxygen off-stoichiometry, which has consequences for the electronic conduction mechanism). Research on the general effect on strain has been carried out elsewhere for substrate induced strain (Campillo et al., 2001), thickness dependence and strain relaxation (Rao et al., 1999) or oxygen stoichiometry (Worledge et al., 1996).

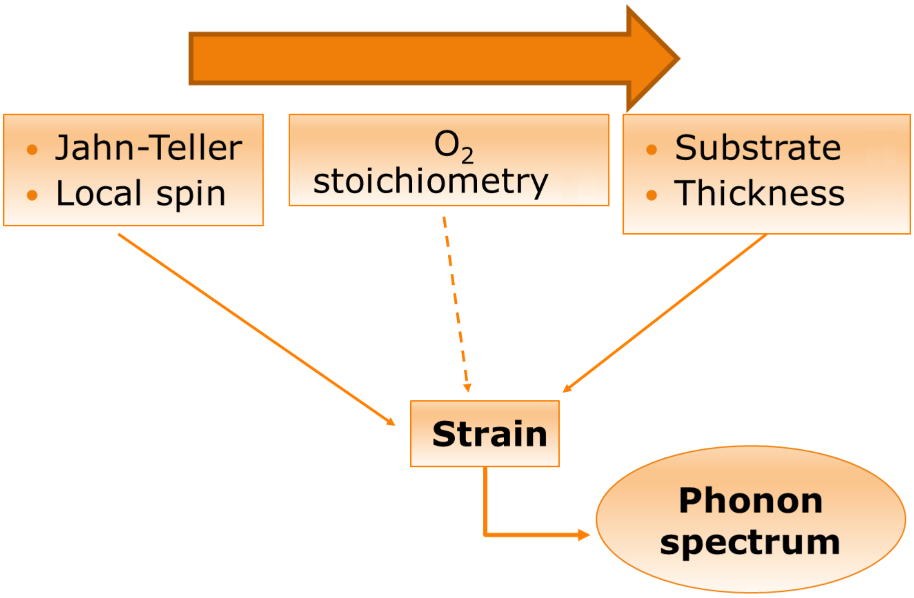

Figure 4.13.: Effect of phenomena sorted by their characteristic length scale from small (top) to large (bottom) on strain, which in turn affects the phonon spectrum through dislocations of atoms.

An annealed sample of 400 nm of LCMO on STO displayed in the bottom panel of Fig. 4.12, as well as other results taken from LCMO grown on LAO shown in the bottom panel of Fig. 4.14, only demonstrate an MTR of approximately 8% at a temperature of approximately 210 K. In addition, the data exhibit a small plateau between 200 K and 220 K. Additional data taken from annealed films grown on LAO show that the substrate has no influence on the agreement with the Wiedemann-Franz law, as the peak height of the MTR remains at approximately 8%. Only the peak temperature is shifted by 50 K from 205 K (STO) to 255 K (LAO), which

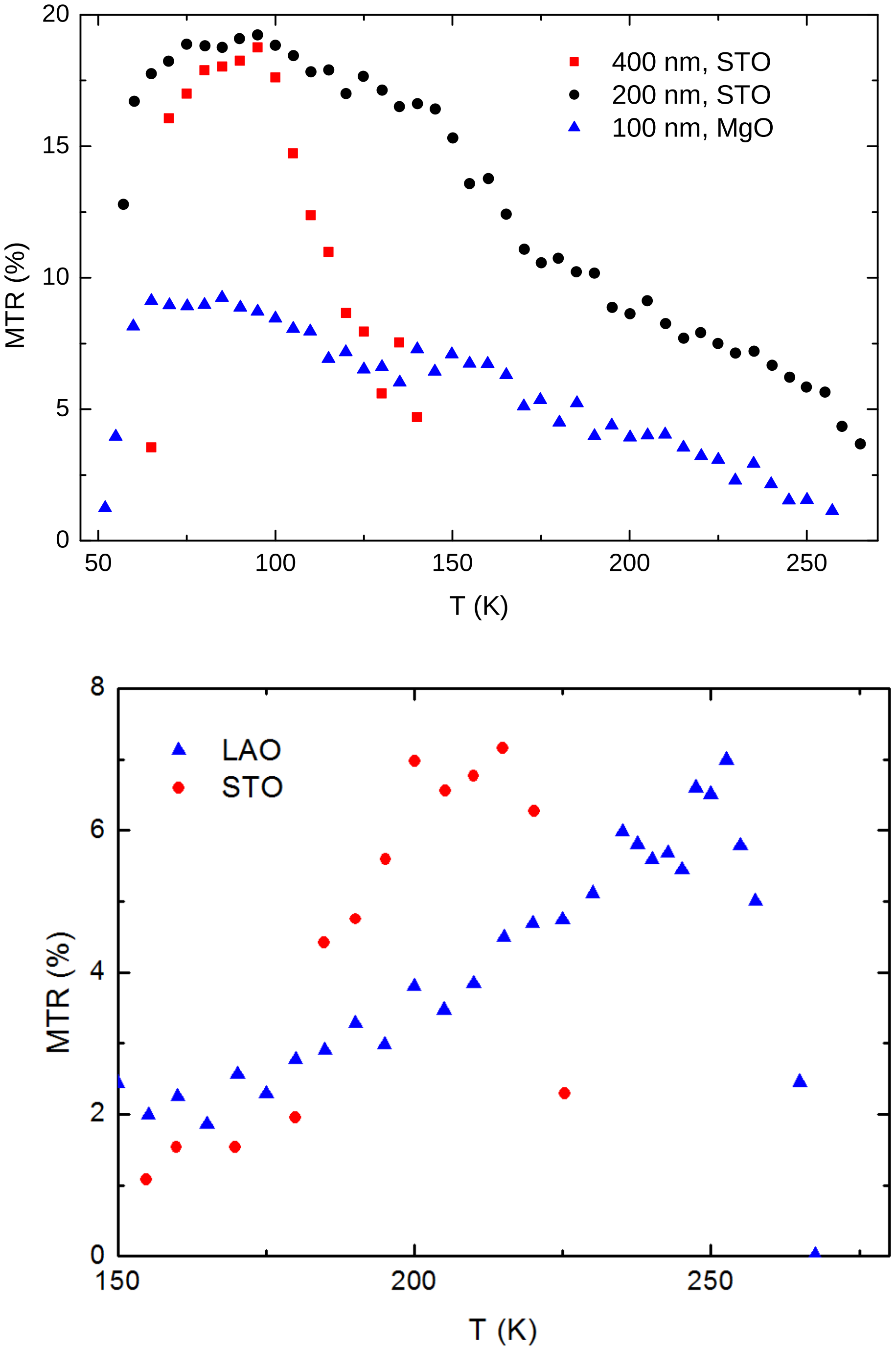

Figure 4.14.: Top: Temperature dependent MTR of as-grown samples of 400 nm and 200 nm LCMO on STO and 100 nm LCMO on MgO. Bottom: Annealed samples of 400 nm of LCMO grown on STO and LAO.

appears to be a substrate-induced effect, that could be related to strain. The comparably large thickness of these films implies that the LCMO is mostly relaxed (LCMO generally relaxes at thicknesses above approximately 200 nm (Ramirez, 1997)).

In addition, the temperature dependence of the MTR expected from CMR measurements in combination with the Wiedemann-Franz law is in reasonable agreement with the shape of the measured values, which is in contrast to the as-grown samples (bottom panel in Fig. 4.12). Specifically, the slope of increase and decrease before and after the maximum are consistent in measurement and expectation and occur at a comparable point in temperature. Moreover, the expectation slightly exceeds the measured MTR, so that the Wiedemann-Franz law overestimates the MTR in annealed samples, while it largely underestimates it in as-grown LCMO. In this context it needs to be kept in mind that the uncertainty of this variation of the 3ω method is prone to uncertainties of approx. 10%. As a consequence, the difference between measured and expected curves is not significant. Finally, the conclusion is reached that, while in the as-grown case there appears to be significant electron-phonon scattering, the effect is not significant in annealed films.

The data obtained from as-grown films on STO, LAO and MgO (Fig. 4.14) and at different thicknesses (400 nm, 200 nm and 100 nm) show the effect of strain and relaxation in oxygen deficient (as-grown) films. The decays of the MTR peaks towards high temperatures are very similar in the case of the 200 nm and 100 nm films, when normalized to the peak MTR value, even though they were grown on different substrates. The peak value of the MTR, however, differs by more than a factor of two. When compared to the results obtained in annealed samples, this indicates that the large lattice mismatch between LCMO and MgO results in a relaxed lattice at very small thicknesses and therefore in smaller peak MTR values. The violent relaxation process involved in films grown on MgO, on the other hand, leads to a slow build-up of the MTR towards T_C. A comparison between the samples grown on STO shows the expected relaxation above 200 nm thickness. Still a large peak MTR value is observed, because the film itself remains strained, as the smaller lattice mismatch between LCMO and STO causes a more continuous relaxation over a larger distance within the film, and complete relaxation in LCMO occurs only above 200 nm.

The raw thermal conductance values of the annealed and as-grown films differ significantly. The general shape of the thermal conductance of an as-grown film displayed in Fig. 4.10 is preserved after annealing, but an offset is observed between both cases. While the as-grown film shows a room temperature thermal conductance of 0.92 W/(m K), the annealed film possesses a thermal conductivity of 1.8 W/(m K) at room temperature and a minimum at 205 K at 1.65 W/(m K). The temperature of the minimum agrees with that of the MTR in Fig. 4.12, since the temperature of the extreme point of the thermal conductance curve does not change significantly with the magnetic field. This is not true for the as-grown film, that displays a broader peak and a significantly different thermal conductivity curve in a magnetic field. In the case of as-grown films, the choice of substrate and the film thickness does not significantly affect the zero-field thermal conductance. The broadness of the maximum at a field of 3 T, however, increases rapidly with decreasing film thickness and with increasing lattice mismatch. In annealed films, the maximum value of the thermal conductivity and the overall shape of the zero-field and full-field thermal conductance curves do not depend on the film thickness or choice of substrate and only the temperature of the maximum is shifted slightly. Therefore, annealed films are comparably robust against strain effects in terms of their thermal conductance.

Concluding, a strong indication of strain related effects in the context of the magnetic field dependence of the thermal conductivity of LCMO is observed. In order to demonstrate an influence on the phonon spectrum and to identify the origin of the effect, the following section expands the experimental spectrum to Raman spectroscopy.

4.4. Phonon Spectrum in LCMO

The analysis of the phononic contribution to the thermal conductance of LCMO is a key part of this chapter, as thorough understanding of the data presented in section 4.3 can only be achieved, if the lattice is well understood. Optical phonons are sensitive to a variety of lattice effects, such as small distortions in the perovskite-like structure (Iliev and Abrashev, 2001, Abrashev et al., 2002), which will prove useful in the discussion of the thermal conductance. On the basis of Lyubarskii (1960), Weber and Merlin (2000), Lewis and Edwards (2001), Smith and Dent (2005), Siebert and Hildebrandt (2008) and Powell (2010) this section introduces one of the main tools available to study this system, Raman spectroscopy, then briefly summarizes previous Raman studies on LCMO and finally presents results on LCMO obtained within the scope of this thesis.

4.4.1. Basics of Raman Spectroscopy

The task of Raman spectroscopy is the detection of scattered laser light irradiating a molecule or a crystalline solid at a frequency ν_0 and thereby shifting its frequency towards a frequency ν_m. As Raman spectroscopy is applied in a wide range of fields ranging from physics to life science, this section will only briefly introduce essential concepts.

Generally, atoms in the crystal are displaced by the laser's electric field

$$\mathbf{E} = \mathbf{E}_0 \cos(2\pi\nu_0 t), \tag{4.7}$$

so that a diplolar structure $\mathbf{P} = \alpha\mathbf{E}$ is formed, where α is the (symmetric) polarizability tensor.

This equation can be expanded by means of a Taylor series in terms of a generalized directional coordinate q, so that

$$\begin{aligned}P_i =&\alpha_{ij}E_{0,j}\cos{(2\pi\nu_0 t)}+\sum_{n=1}^{Q}\left(\frac{\partial\alpha_{ij}}{\partial q_n}\right)_0 q_{0,n}E_{0,j}\cos{(2\pi\nu_0 t)}q_{i,0}\cos{(2\pi\nu_i t)}+\mathcal{O}(q_0^2)\\ =&\alpha_{ij}E_{0,j}\cos{(2\pi\nu_0 t)}+\frac{1}{2}\sum_{n=1}^{Q}\left(\frac{\partial\alpha_{ij}}{\partial q_n}\right)q_{0,n}E_{0,j}\left[\cos{(2\pi(\nu_0-\nu_m)t)}+\cos{(2\pi(\nu_0+\nu_m)t)}\right],\end{aligned} \tag{4.8}$$

where $Q = 3N - 6$ is the number of modes in a nonlinearly coupled system. The first term corresponds to Rayleigh scattering, the second to Raman scattering. Specifically, the $\nu_0 \pm \nu_m$ terms correspond to Anti-Stokes (emitted frequency larger than absorbed frequency) and Stokes (emitted frequency smaller than absorbed frequency) scattering, respectively. A vibrational mode is Raman inactive, if either the derivative preceding the cosine terms is zero, or if the sum of the cosines is zero, or both. Phrased differently, a mode is Raman active, if one component of the polarizability tensor depends on atomic displacement and the intensity of the spectral peak is proportional to the directional derivative.

The selection rules can be formulated in a more elegant way by means of group[6] theory. Defined as a periodic structure subdivided into unit cells, each crystal is invariant under a group of geometric operations, that are standardized as the Schoenflies notation (Schönflies, 1891), such as

- the identity,
- $\mathcal{C}_n$: rotation around the axis with n permitted operations,
- σ: reflectional planes of symmetry,
- i: points of inversion symmetry,
- $\mathcal{S}_n$: Rotation and reflection.

Each of these operations can be represented in matrix form. Generally, a matrix acting on a vector space V can be reduced into sub-matrices each operating on mutually disjunct subspaces V_i, which as a direct product resemble V. A matrix composed of representations that can not be further reduced is termed an irreducible representation of the geometric operation. Intuitively, an irreducible representation can be diagonalized and the trace of the matrix χ

---

[6] A group G is defined as a set with an operation $\wedge$, which is closed under the operation, obeys associativity under $\wedge$ and possesses an identity element $E \in G$, so that for any $g \in G$ $g \wedge E = g$ and there exists an inverse element $g^{-1} \in G$ to each $g \in G$ such that $g \wedge g^{-1} = E$.

is named the character of the representation. Equivalent representations possess identical characters, as similar matrices[7] have identical traces. Hence it can be proven that there exists an isomorphism between the irreducible representation and its character. The characters of the representations acting on a crystal allow the determination of the polarizability tensor, as will be explained in the following paragraphs.

Based on this decomposition the available modes are then classified by their symmetries into A, B, E and T modes. A_1 modes are symmetric under rotation around the principal (in LCMO: C_4) axis. If additionally they are antisymmetric around the C_2 axis, they are denominated A_2. B modes are antisymmetric under rotation around the principal axis of rotation. If they are symmetric with respect to C_2, they are termed B_1, else B_2. E and T modes are double- and triple-degenerate, respectively. Finally, the letters are primed and double-primed, if the modes are symmetric or antisymmetric with respect to σ_h.

The symmetry of a vibration can easily be determined by depolarization measurements, during which the sample is illuminated along a crystallographic axis. The depolarization ratio ρ_p is defined as

$$\rho_p = \frac{I_{\text{perp}}}{I_{\text{parallel}}}, \tag{4.9}$$

where I_{perp} and I_{parallel} are the intensities measured in perpendicular and parallel geometry (with respect to the polarization of the incident light), so that $\rho_p = 0$ in the case of a polarized sample with $\alpha_{xx} = \alpha_{yy} = \alpha_{zz}$ and ρ_p in the case of a depolarized sample.

The experimental determination of the polarizability of a mode together with theoretical modeling of the applicable selection rules finally allow an identification of the observed modes with physical structures. Quantum mechanical treatment of the transition from a vibrational mode ν' to ν'' caused by a deflection of the lattice point by dq results in an expression for the transition coefficients

$$(\alpha_{ij})_{\nu'\nu''} = \int \psi^*_{\nu''}(q)\alpha_{ij}\psi_{\nu'}(q)\, dq. \tag{4.10}$$

If one of these coefficients is non-zero, the mode is Raman active in the respective component. This formulation, however, does not yet contain explicit physical information about a correspondence with the representations introduced above. By expanding the polarizability tensor into a Taylor series to first order as in Eq. 4.8, Eq. 4.10 becomes

$$(\alpha_{ij})_{\nu'\nu''} = \alpha_{ij,0} \int \psi^*_{\nu''}(q)\psi_{\nu'}(q)\, dq + \left(\frac{d\alpha_{ij}}{dq}\right) \int \psi^*_{\nu''}(q) q \psi_{\nu'}(q)\, dq. \tag{4.11}$$

---

[7] Let V be a vector space over a field K. $A, B \in V$ are termed similar, if there exists an invertible matrix S so that $B = S^{-1}AS$.

The first term is zero, because the ψ are mutually orthogonal. The second term is non-zero, if $\Delta\nu = \pm 1$. $\frac{d\alpha_{ij}}{dq}$ is non-zero, if its representation is totally symmetric.

As discussed in section 2.2 the optical branches of the phononic spectrum are caused by translational, rotational and vibrational degrees of freedom. The former two are located in the far IR spectrum and are not considered Raman modes. Vibrational Raman modes are located in the center of the Brillouin zone.

4.4.2. Previous Research

One of the earliest discussions of the importance of Raman scattering in the understanding of the many-fold interactions between subsystems of LCMO was presented by Podobedov et al. (1998) who studied epitaxial LCMO grown by PLD on $LaAlO_3$ (LAO) and $NdGaO_3$ (NGO). Their Raman spectra were obtained in a 90° geometry with the incoming beam perpendicular to the sample surface. In agreement with previous studies on manganites in general, their samples displayed the known vibrational modes A_g at approximately 200 cm^{-1} and B_{2g} at approximately 435 cm^{-1}, which they attribute to the phononic density of states (DOS). In addition, they noted a peak at 660 cm^{-1}, which they found to increase in intensity for films annealed in oxygen. They found no difference between the spectra of LCMO grown on NGO and LAO. Interestingly, the authors found the peak at 660 cm^{-1} to depend more strongly on the excitation wavelength than expected from penetration depth calculations, and found it to disappear after the sample was polished and therefore attributed it to surface degradation. Finally, temperature dependent Raman analysis resulted in the conclusion that the line width of the A_g mode is sensitive to lattice spin-phonon coupling, which is related to spin orientation below T_C.

Abrashev (1999) extended this research towards $SrTiO_3$, yttria-stabilized zirconia (YSZ) and MgO substrates. According to Iliev et al. (1998), the A_{1g} mode at 200 cm^{-1} is related to static tilting of the MnO_6 octahedra, and the modes at 450 cm^{-1} and 610 cm^{-1} need to be related to the dynamic Jahn-Teller effect. The samples were produced by sputtering; Raman analysis was carried out using a He-Ne laser. They claim their polarized Raman spectra showed the samples on MgO and YSZ to be polycrystalline, whereas those on LAO and STO were single-crystalline, as the Raman spectra of the former were shown to be insensitive to polarization changes. Furthermore, it was found it to be plausible that the mode found at 230 cm^{-1} is caused by oxygen vibrations caused by rotational motion of the oxygen octahedra. They agreed with Podobedov et al. (1998) on the conclusion of the Jahn-Teller origin of the 453 cm^{-1} and 610 cm^{-1} modes and found that in the case of single-crystalline LCMO the intensities of these lines increase with decreasing temperature until T_C, where they reach a maximum. In the polycrystalline case, however, they claim that the intensities increase monotonously with decreasing temperature, which they take as evidence that the lines do not, as assumed by Podobedov et al. (1998), correspond to lattice spin-phonon coupling. Instead, since the temperature dependence is found to be analog, Podobedov et al. determined the lines to be a marker of the sample resistance. However, they failed to interpret a mode at 437 cm^{-1} in the spectrum of LCMO on LAO, which increases in intensity with decreasing temperature, even though the claim was that in epitaxially grown films modes associated with the Jahn-Teller effect would decrease in intensity below T$_C$. Other research such as Iliev and Abrashev (2001), Pantoja et al. (2001), Abrashev et al. (2002), Xiong et al. (2004) are inconsistent about this feature. Interestingly, the paper by Abrashev et al. (2002) that summarizes phonon modes expected from lattice distortions does not contain this feature.

Abrashev (1999) interpreted the line width of the Jahn-Teller modes with respect to the phonon life time, which was found to predict the sample resistance with high accuracy. Applying this interpretation to the 230 cm^{-1} mode allowed the interpretation of line narrowing by an increased mean free path of the phonon system caused by decreased Jahn-Teller distortions. Iliev and Abrashev (2001) directly followed this path by considering Jahn-Teller bands in perovskite-like manganites in general. They subdivided Jahn-Teller distortions into small and large distortions and furthermore considered small perturbations to be caused mainly by the above mentioned life time effect. Large distortions posed the possibility of a complete structural transition, so that all phononic states that were previously forbidden are then Raman active. Thereby these modes were assigned to 'pure phonon density of state' defined by the energy dispersion of the oxygen phonon branches.

A more thorough approach was finally chosen by Pantoja et al. (2001) who presented mode assignments based on the symmetries of the Pnma space group. Out of the 60 allowed phononic modes 24 are Raman active (7×A$_g$, 5×B$_{1g}$, 7×B$_{2g}$ and 5×B$_{3g}$). Their study of the known phonon modes revealed the detail that the 610 cm^{-1} mode actually is a doublet. In addition, they found a mode softening in the above mentioned Jahn-Teller mode at 453 cm^{-1} below T$_C$, which they explained to be a consequence of magnetic ordering. The overall behavior between room temperature and 10 K, however, is explainable by thermal contraction in an anharmonic model. Interestingly, the authors revisit the problem of the correlation of the Jahn-Teller modes with either magnetization or electronic resistance. According to them 'this softening phenomenon is clearly related to the magnetic transition' (Pantoja et al., 2001) - thereby restoring an equilibrium of opinions.

Abrashev et al. (2002) went one step further to perform lattice-dynamical calculations according to Popov (1995) on the parent compound CaMnO$_3$ (CMO), in which the lattice is modeled as point charges Z interacting through Coulomb interactions. The corresponding electronic repulsion is described by a Born-Mayer-Buckingham interaction

$$V = a\,e^{-br} - \frac{c}{r^6}, \tag{4.12}$$

in which a, b and c are parameters and r is the interionic distance. The electron shells themselves are modeled by ions with reduced charge Z-Y coupled to shells with charge Y with a force constant k, so that the free ion polarizability is given by

$$\alpha = \frac{Y^2}{k}. \tag{4.13}$$

The resulting Raman intensities of active modes in CMO are then transformed into those of distorted structures as observed in LCMO. Specifically, as of the twelve atomic coordinates in LCMO five are fixed, there are seven degrees of freedom resulting in four types of distortion that Abrashev et al. (2002) refer to as 'basic distortions':

1. rotation around [101] into the Imma space group caused by a rotation or tilting of the MnO_6 octahedron,
2. rotation around [010] into P4/mbm caused by a deviation of the tolerance factor from unity,
3. Jahn-Teller distortion into P4/mbm caused by a difference between the distances of two Mn-O pairs inflicted by the population of the e_g orbital in Mn^{3+},
4. shift of the A-site atom into the Cmcm configuration caused by inhomogeneous bonding of oxygen to the A-site atom.

Using these basic distortions the authors calculated the expected frequencies of the corresponding modes and correlate them to measured spectra. The result indicates that the suggestion of Podobedov et al. (1998), attributing certain modes to purely phononic densities of state, was indeed valid.

4.4.3. Temperature Dependent Raman Spectroscopy

Even though the results in section 4.3 evidently underline the effect of strain on the MTR, a clear demonstration of the phononic nature of the enhanced MTR in as-grown films has not yet been given. Raman spectroscopy, as a method that is sensitive to the phonon spectrum of a material, is in this section used to clarify the origin of the anomalous phononic MTR. The physical origin of the MTR lies within the coupling of an external magnetic field to the Mn spin, which couples to electronic transport, which in turn couples to the distortion of the unit cell. Therefore, observing a difference in the magnetic field induced changes in the Raman spectra of as-grown and annealed LCMO would immediately prove the enhanced MTR to be of phononic nature. Unfortunately, magnetic field dependent Raman spectroscopy was not available to any collaboration partner.

Nevertheless, the comparison between Raman spectra of as-grown and annealed LCMO in zero field can provide useful information. In general, in LCMO electronic transport and the incoherent phononic DOS visible in the Raman spectra are coupled so that the temperature dependent increase of the phononic DOS implies an increased electrical and thermal resistance. The measurements and fits were carried out by Andreas Talkenberger at the Technische Universität in Freiberg.

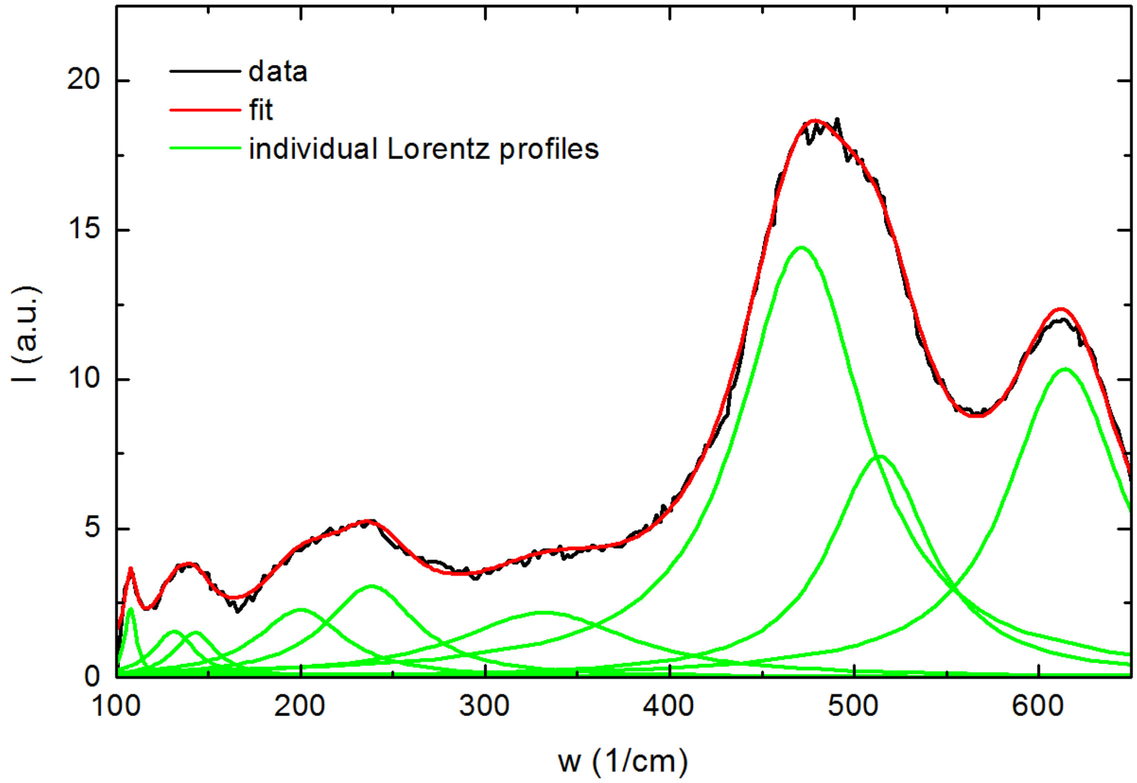

Figure 4.15.: Exemplary demonstration of a fit (red line) of individual Lorentz profiles (green lines) to a spectrum of Raman shift at 633 nm (black line).

Temperature dependent Raman spectroscopy at 633 nm of an as-grown 400 nm LCMO film on STO results in a spectrum (Figs. 4.15 and 4.16) with two prominent peaks at wavenumbers of 480 cm^{-1} and 610 cm^{-1} (in Fig. 4.16 the Raman spectra are shifted for clarity). Fig. 4.15 exemplarily demonstrates the fitting procedure of Lorentz profiles to the total spectrum. The general agreement of the fit (red line) with the data (black line) is convincing, even though there are small, but insignificant, differences e.g. between 250 1/cm and 300 1/cm and at the peak at 600 1/cm.

Data taken at an excitation wavelength of 442 nm, however, display a very low signal to noise ratio, so that the spectra were considered unsuitable. Measurements at an excitation wavelength of 633 nm proved to be much clearer. Modes at 242 1/cm, 480 1/cm and 610 1/cm are consistent with phonon modes given in the literature introduced in the previous section. Spectra taken at 532 nm show peaks at 235 1/cm, 470 1/cm and 612 1/cm. Compared

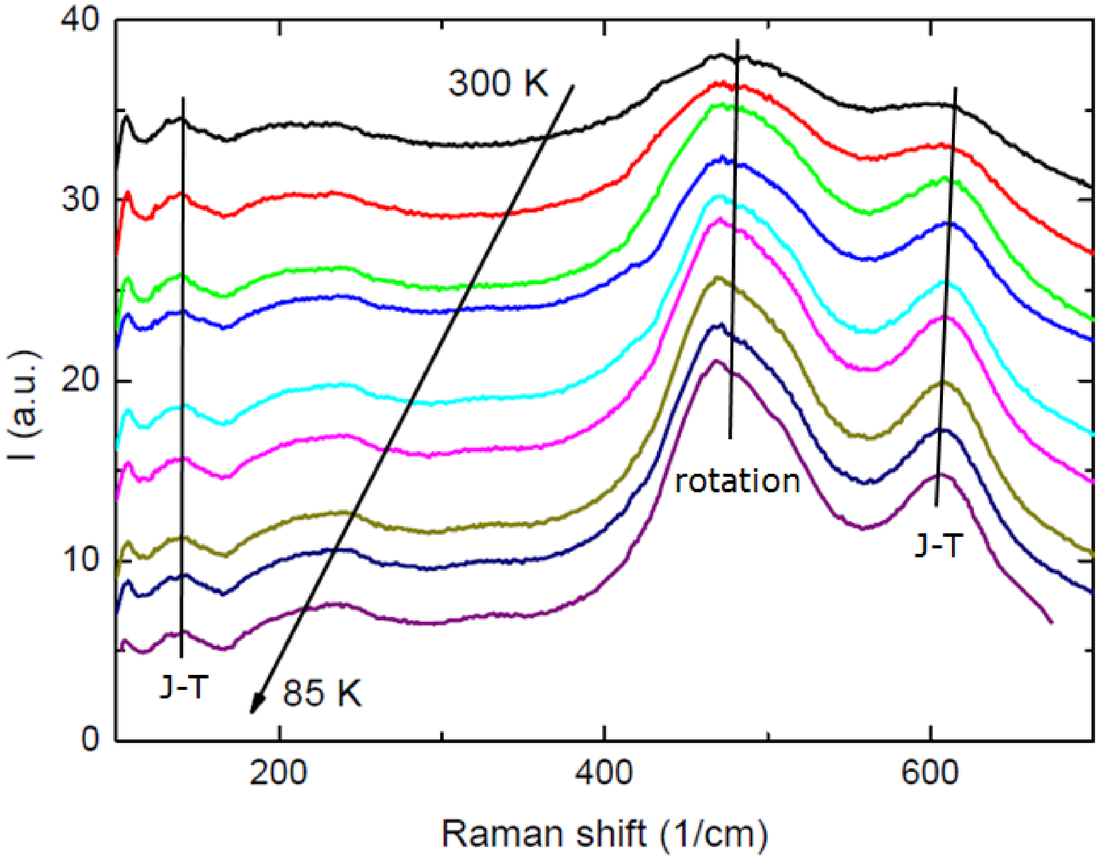

Figure 4.16.: Raw Raman spectra at 633 nm of as-grown 400 nm LCMO on STO. The STO signal is invisible due to the limited information depth of the setup. The identification of the Jahn-Teller associated lines ('J-T') and that caused by a rotation of the oxygen octahedron ('rotation') is based on Abrashev (1999). The temperatures of the spectra are 300 K, 250 K, 200 K, 150 K, 125 K, 115 K, 105 K, 95 K and 85 K and are shifted vertically for clarity.

to the spectra at 633 nm these peaks are slightly shifted. If any of the detected lines were measurement artifacts, they should remain at constant position in the spectrum. The measured lines shift with the excitation frequency, which demonstrates that the modes indeed are phonon modes and not signatures intrinsic to the measurement process.

All temperature dependent measurements were subsequently carried out at 633 nm. At 430 1/cm a shoulder in the peak appears, in particular at temperatures above 115 K. The mode at 610 1/cm (room temperature) shifts to slightly larger wavenumbers until 150 K and then shifts back to 605 1/cm at 85 K, the lower temperature limit of the experiment. The absolute intensities of the lines at approx. 480 1/cm and 610 1/cm decrease with temperature, whereas those between 100 1/cm and 250 1/cm remain at a constant intensity.

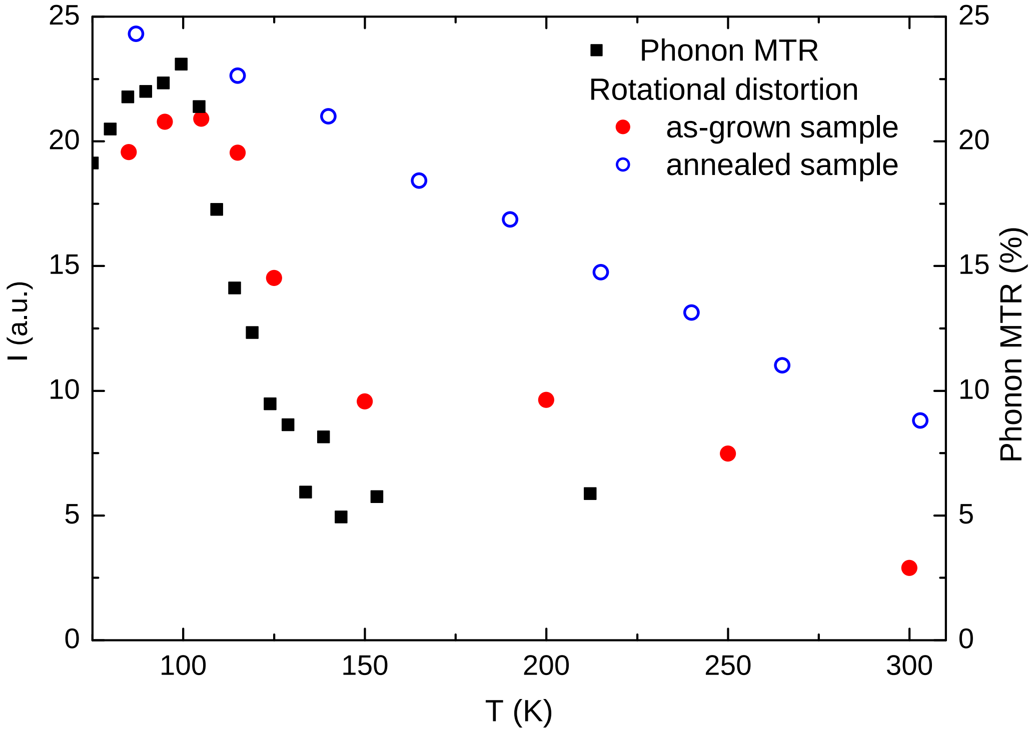

Figure 4.17.: The temperature dependence of the intensity of the 480 cm^{-1} Raman line in as-grown 400 nm LCMO grown on STO (red circles) in comparison to the phononic contribution to the MTR (black squares). Open blue circles represent the intensity of the 480 cm^{-1} line in annealed 400 nm LCMO grown on STO. The annealed sample shows no spontaneous increase between 250 K and 200 K.

Using the formalism of basic distortions, Abrashev (1999) calculated line positions for CMO, which are adopted here for the case of LCMO. Deviations are expected to be small, because the doping of CMO with La only slightly changes the tolerance factor. Defects caused by the adjustment to the new tolerance factor should not cause the approximation of LCMO by the CMO structure to fail. The identification of Abrashev (1999) of the line at approximately 480 cm^{-1} who understood the respective phonon modes to originate from a rotational distortion of the oxygen octahedra allows an interpretation of the anomalous MTR in the as-grown samples. Xiong et al. (2004) agree with the interpretation of Abrashev (1999). In particular, the intensity of a line, which is measured by a Lorenz fit curve, is proportional to the respective contribution to the DOS, that is proportional to the phononic thermal conductivity. Thus, the temperature dependence of the 480 cm^{-1} line intensity is chosen as a tool to analyze the difference in phonon structure between as-grown and annealed LCMO samples.

Figure 4.17 displays the intensities of the fits to the 480 cm^{-1} lines in as-grown and annealed LCMO in dependence of the temperature and compares them to the phononic contribution to the MTR in as-grown LCMO. The general agreement in behavior between the 480 cm^{-1} line fit of as-grown material and the MTR curve indicates that the additional contribution to the Raman spectra introduced by a rotation of the oxygen octahedra causes the phononic MTR, since the density of states is proportional to the thermal conductivity. Iliev et al. (1998) found that in the case of single-crystalline LCMO the intensities of the Jahn-Teller related lines increase with decreasing temperature until T_C, where they reach a maximum, whereas in the polycrystalline case the intensities increase monotonously with decreasing temperature. Our data confirm this correlation between the single-crystalline nature of thin film LCMO and the line intensities.

In an annealed sample of 400 nm LCMO grown on STO the MTR peaks at above 200 K and has a value in general agreement with Wiedemann-Franz. The fitted Raman intensities of the octahedral distortion, in contrast to the data taken from the as-grown sample, display no anomalous peak in the vicinity of the MTR peak. Therefore, increasing the oxygen stoichiometry improves the lattice coherence and reduces rotational distortions of the oxygen octahedra which causes the corresponding phononic density of states contribution to the Raman spectra to decrease. Thus, the anomalous MTR is most probably caused by the enhanced rotation of the oxygen octahedron, which couples to the electronic occupation of the manganese atom in the center yielding a polaronic state.

An analysis of the line widths provides information regarding the phononic mean free path (Abrashev, 1999) and consequently a measure of the strength of the distortion. While the 480 cm^{-1} line of the as-grown sample, corresponding to oxygen octahedron rotation, remains at a similar width between 250 K and 150 K, it then quickly narrows towards lower temperatures until reaching a minimum at 105 K, implying that the turning process of the octahedron terminates. The Jahn-Teller related line at 610 cm^{-1} naturally reaches a minimum width at 105 K corresponding to the metal-insulator phase transition. Major changes take place between 150 K and 100 K in agreement with the data presented in Fig. 4.11. In an annealed sample no such steep decrease, but rather a smooth decline towards and beyond the metal insulator transition (which then occurs at approximately 220 K) is observed. It is expected that the conclusions reached for as-grown LCMO on STO are valid also for the case of MgO, as Podobedov et al. (1998) found no difference between spectra of samples grown on different substrates (which is attributed in part to the low volume sensitivity of Raman spectroscopy).

In summary, this section demonstrated that the origin of the non-Wiedemann-Franz magnetothermal resistance in as-grown LCMO is within a rotation of the oxygen octahedra that does not occur in annealed films. Furthermore, the results indicate an influence of the magnetic field on the phonon spectrum, which is plausible, as by the superexchange transport model structural distortions and spin alignment are linked.

CHAPTER 5

MAGNETOTHERMAL RESISTANCE IN THE FILM PLANE

In the presence of a magnetic field additional contributions to the resistance of a sample can arise. This so-called magnetoresistance is defined as the normalized change of the electrical resistance caused by the field as

$$\mathrm{MR} = \frac{R_{\mathrm{B}\neq 0} - R_{\mathrm{B}=0}}{R_{\mathrm{B}\neq 0}}. \tag{5.1}$$

Depending on the sign of this change, the magnetoresistance can be positive or negative. In the case of free electrons in a magnetic field the magnetoresistance will be positive, since the electrical resistance increases due to the Lorentz force guiding electrons into a spiral motion. Positive magnetoresistance is generally associated with a magnetic field also in solids, even though it can be superimposed by negative contributions arising from different scattering or transport mechanisms, as seen in the anisotropic (AMR), giant (GMR), tunneling (TMR) or colossal (CMR) magnetoresistance effects. The CMR as the largest of these effects was in the previous chapter shown to possess an analogy in terms of the magnetic field dependent thermal conductivity.

The AMR, as the smallest of the magnetoresistance effects mentioned above, should also have a thermal counterpart, which would be much smaller than in the case of the CMR and therefore much more difficult to measure. In particular, the 3ω method generally suffers from large uncertainties, so that differences in thermal conductivity of smaller than 5% -10% are usually not detectable. This chapter demonstrates that nevertheless it is possible to determine the magnetic field influence on the thermal conductivity in an AMR material, Permalloy, by the 3ω method. However, the result requires careful discussion, since it relies on a measurement of the substrate thermal conductivity that could be implausible.

5.1. The Anisotropic Magnetoresistance

The AMR was discovered in 1857, when Thomson observed the electrical resistance to depend on the angle ϕ between an electrical current and the direction of an applied magnetic field. The physical reason explaining this observation is the alignment of the sample magnetization with the field and a resulting asymmetry in the electronic scattering properties, that can phenomenologically be described as (McGuire and Potter, 1975)

$$\rho(\phi) = \rho_\perp + (\rho_\parallel - \rho_\perp)\cos^2(\phi). \tag{5.2}$$

$\rho_\perp$ and $\rho_\parallel$ denote the resistivity measured perpendicular and parallel to the magnetization, respectively. With increasing magnetic field, the AMR rises and eventually saturates, while the sample magnetization aligns with the field. The AMR is caused by spin orbit coupling, which stems from a non-circular symmetric charge distribution within the unit cell (e.g. in the case of 3d electrons, the electronic states at $l_z = 2$ are more frequently populated than those at $l_z = 0$). This asymmetry results in a non-zero probability for a spin flip generated by the spin-orbit coupling, which ultimately leads to a change in the electrical resistance in the presence of a magnetic field (McGuire and Potter, 1975).

Permalloy (Py) is a ferromagnetic alloy composed of Ni and Fe in the ratio of 4:1 and suitable for spintronic applications. One of its principal properties is a large Anisotropic Magnetoresistance, which can reach resistance changes of up to several percent (Mitchell et al., 1964, Jedema et al., 2001, Nahrwold et al., 2010, Manzin et al., 2014). The AMR is commonly defined as the difference in the electrical resistance in the film plane between the value at a state with the sample magnetization parallel to the probing electrical current and perpendicular (or at an angle) to it as $\mathrm{AMR} = \frac{R_\perp - R_\parallel}{R_\perp}$.

As described previously, the heat conductivity of a material is usually decomposed into a phononic and an electronic contribution as $\kappa = \kappa_{ph} + \kappa_e$. In simple metals, the phononic contribution is negligible at room temperature and the Wiedemann-Franz law is valid, i.e. the electronic thermal conductivity is expected to relate to the electrical conductivity σ, the specific resistivity ρ and the temperature T according to

$$\frac{\kappa_e}{\sigma} = \kappa_e \rho = L_0 T, \tag{5.3}$$

where, as in the previous chapter, the Lorenz number L_0 is assumed to be constant with respect to the temperature as originally expected from the Drude theory. The AMR should, by Eq. 5.3, contribute to the thermal conductance as a magnetothermal resistance (MTR) analogous to that introduced in Chapter 4. The MTR is then given by the ratio between the thermal conductance values in parallel alignment to the field, $\kappa_\parallel$, to that at a relative angle ϕ, κ_ϕ, as

$$\mathrm{MTR} = \frac{1/\kappa_{\phi} - 1/\kappa_{\|}}{1/\kappa_{\phi}} = \frac{\kappa_{\|} - \kappa_{\phi}}{\kappa_{\|}}. \tag{5.4}$$

For the Wiedemann-Franz relation to be valid, the electron scattering processes that degrade the electrical conductivity need to be predominantly elastic, which is an assumption fulfilled for metals such as Py. Again, this relation is assumed for the discussion in spite of its incompleteness, as it distinctly demonstrates deviations from free-electron behavior. The magnitude of the MTR is, neglecting the phononic contribution in a good metal such as Py, limited by the magnitude of the AMR.

The MTR in AMR materials has been studied previously in the case of Ni nanowires (Ou et al., 2008, Kimling et al., 2013). One of the reasons for their choice of nanowires was the increased resistivity of the material caused by an enhanced crystallite interface density, which could cause non-Wiedemann-Franz behavior and therefore increase the effect for better measurability. Both studies found a Wiedemann-Franz-like contribution of the AMR to the thermal conductance between 300 K and 77 K. In addition, they claim a contribution of normal phonon scattering processes that should lead to an additional contribution to the thermal conductance at temperatures, at which the effect of the Umklapp processes decreases, since additional scattering processes are introduced in addition to those assumed in the Drude theory (see Section 2.1).

As mentioned above, in the case of thin film Py the AMR has been found to possess values of several percent. The resulting changes in thermal conductivity described by the Wiedemann-Franz law therefore are expected to be of similar magnitude. Measuring a difference in thermal conductivity of this magnitude has proven to be difficult, as the statistical uncertainty of 3ω thin film thermal conductivity data is generally thought to be of the order of 5-10% (Mix, 2010, Kimling, 2013). In this chapter it is demonstrated that, with rigorous control of the experiment and large sampling rates, changes of the thin film thermal conductivity of Py of less than 4% can be measured using the 3ω method and, by the angular dependence, attributed these changes to the anisotropic MTR.

5.2. Magnetothermal Resistance in Permalloy

Generally, the AMR and related effects such as the anisotropic MTR are identified by their characteristic angular dependency. In the case of the AMR this dependency is given by $\cos^2(\phi)$, so that, since ρ and κ are inversely proportional due to the Wiedemann-Franz law, the MTR should display an angle dependency of $\sin^2(\phi)$. Here ϕ is the angle between the sample magnetization and the easy axis. A contribution of the AMR to the MTR can thus be measured by positioning the sample in an external magnetic field parallel to the sample surface and rotating the sample or the field while measuring the thermal conductance.

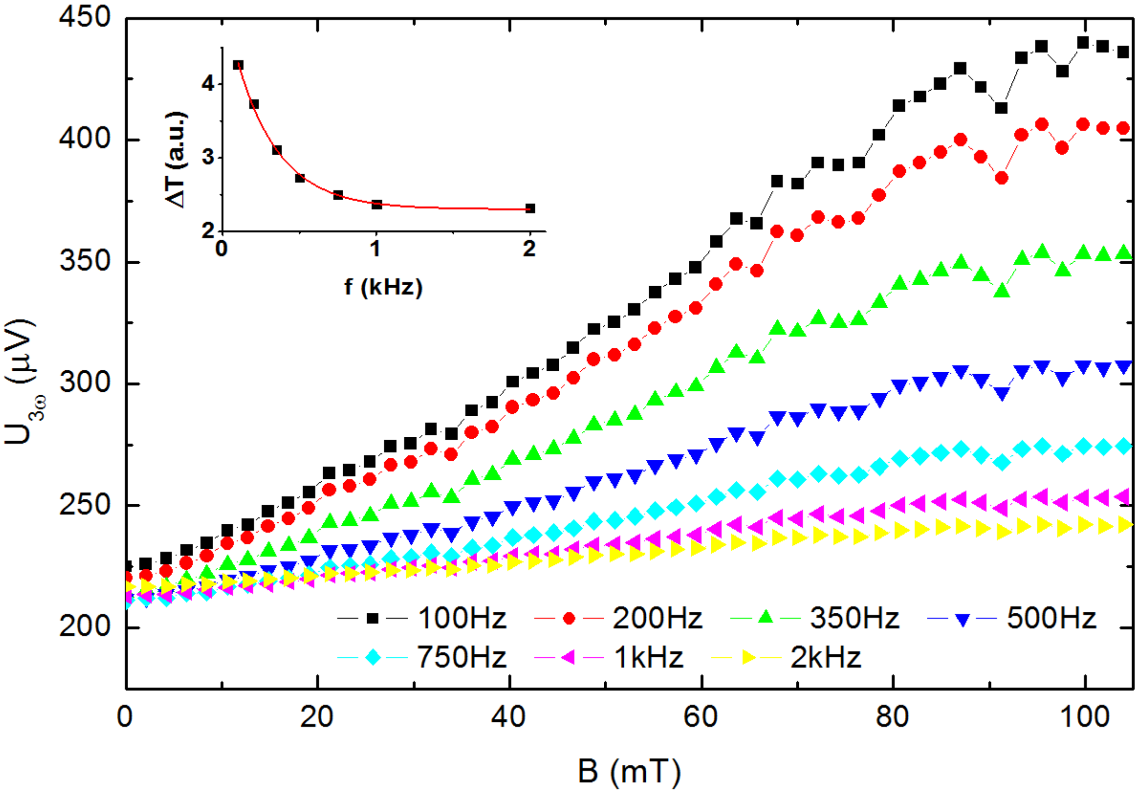

Figure 5.1.: Magnetic field dependence of the signal at the third harmonic in the 300 nm thick sample between zero and 105 mT. ϕ is set to $0°$. The inset displays a f^{-1} fit to the data at 100 mT. The systematic reduction of the data at 92 mT is a measurement artifact. Error bars are omitted for clarity.

The thermal conductance perpendicular to the film plane of the substrate is measured by the standard 3ω method. The thermal conductance in the film plane is determined by the Bayesian extension presented in Chapter 3.3. The necessary field-dependent substrate thermal conductivities were determined by the slope-based method introduced in Chapter 3.1 and cross-checked by the Bayesian algorithm. Both methods resulted values comparable up to a relative difference of 2%.

The samples consisted of 300 nm thick Py films grown on Si substrates by industrial sputtering at Sensitec GmbH. 200 nm of Al_2O_3 were deposited by RF magnetron sputtering on top of the Py film to insulate it from the 50 nm Au capping layer that was structured into the 3ω structure by optical lithography. Reference samples were grown and structured under the same conditions and had a Py film thickness of 20 nm. The measurement method eliminates the need for a separate determination of thermal interface resistances, as was explained in Chapter 3.1.

The thermal conductance of the samples was measured in magnetic fields of up to 105 mT

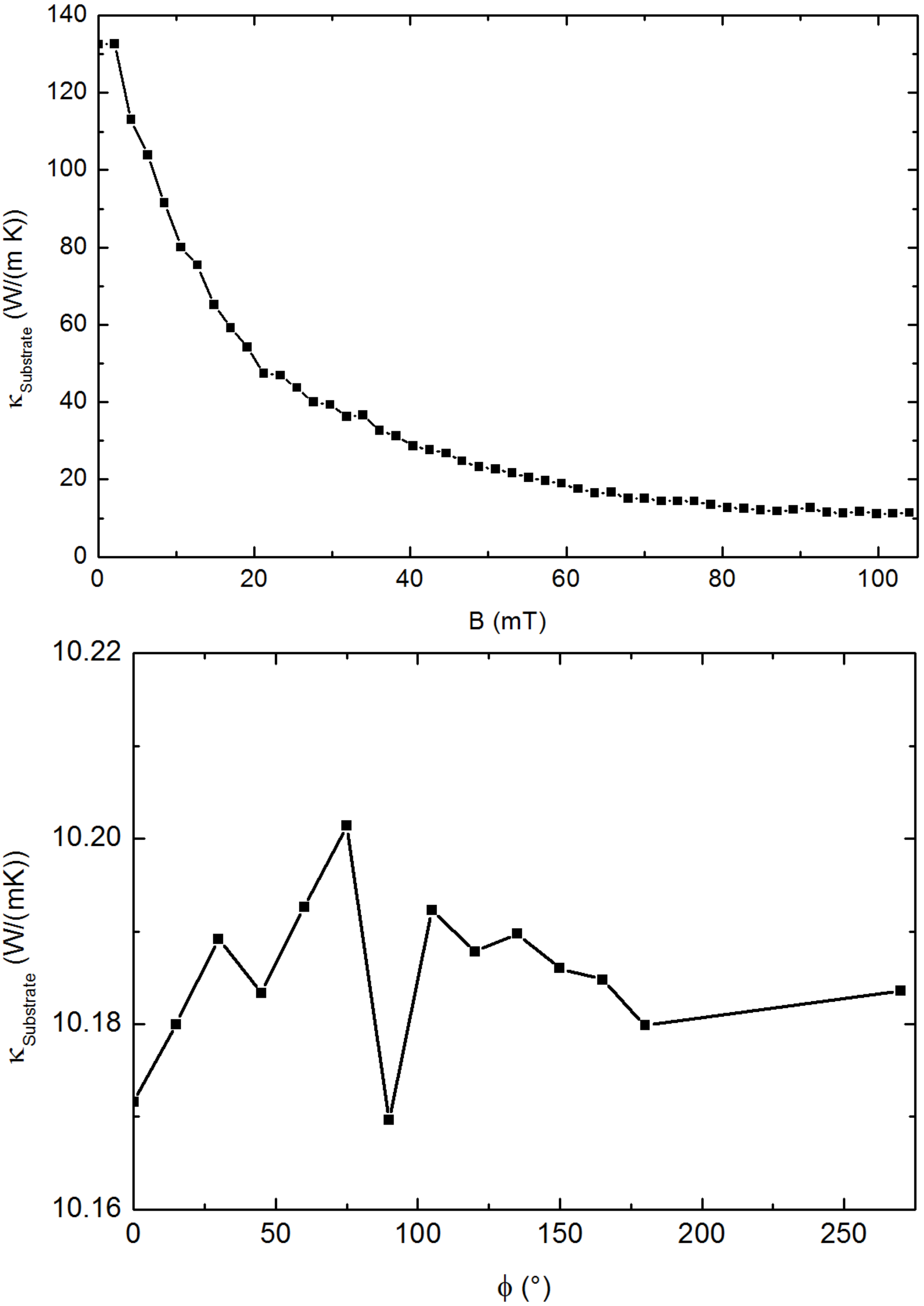

Figure 5.2.: Top: The thermal conductivity of the Si substrate determined by the slope method. Bottom: The thermal conductivity of the Si substrate as a function of the rotation angle ϕ at an in-plane field of 105 mT.

at a temperature of (13.8 ± 0.2)°C in a water cooled electromagnet. The field step size was 2.1 mT; at each field step the measurement was carried out at seven excitation frequencies between 100 Hz and 2 kHz with a sampling rate of 1000 data points per frequency to obtain a mean value and a standard deviation.

Fig. 5.1 displays the magnetic field dependence of the $U_{3\omega}$ signal with applied frequency at $\phi = 0°$. Evidently, $U_{3\omega}$ and thus the temperature oscillation generally decreases with increasing frequency as is to be expected, since the amplitude of the thermal oscillation is proportional to the integral of the heating power above the average over half a period:

$$\Delta T \propto \int_0^{\pi/(2\omega)} \sin(2\omega t)\,\mathrm{d}t \propto \frac{1}{\omega}, \tag{5.5}$$

which is displayed in the inset of Fig. 5.1.

More importantly, the temperature oscillation increases with increasing field strength and saturates at a field strength of approx. 95 mT. The substrate thermal conductivity that is required by the Bayesian algorithm was extracted by the slope-based method and is found to be insensitive to in-plane rotation (Fig. 5.2). While at room temperature the thermal conductivity amounts to approx. 132 W/(m K), its value seems to decrease dramatically with increasing field. This counterintuitive and possibly unphysical behavior is addressed in the following section. Nevertheless, the data are evaluated further assuming that the results obtained for the substrate thermal conductance are reliable. Consequently, the results need to be taken with caution.

As the temperature oscillation originates from the effectiveness of heat transport away from the heater structure, an increasing temperature oscillation at constant frequency is equivalent, but not proportional, to a decrease in thermal conductivity. In the case of the 100 Hz measurement the measured 3ω voltage signal at a field of 100 mT has decreased to 45% of the original (zero field) value. At zero field, the thermal conductivity in the film plane of the Permalloy thin film, displayed in the top panel of Fig. 5.3, amounts to $\kappa_{\mathrm{xy}} = (14.2 \pm 0.4)$ W/(m K). Assuming that the thermal conductance values of the Si substrate determined by the slope method are correct, the maximum relative decrease in thermal conductivity is determined to 3.4%.

The thermal conductance in the film plane clearly exhibits a $\sin^2(\phi)$ behavior. The statistical uncertainty totals to approx. 3%. The thermal conductivity perpendicular to the film plane is not strongly affected by the in-plane magnetic field (bottom panel in Fig. 5.3). A small, and statistically insignificant, contribution displays $\sin^2(\phi)$ characteristics and is equivalent to a MTR of 0.24%. The zero-field thermal conductance of Py perpendicular to the film plane amounts to $\kappa_{\mathrm{z}} = 14.1$ W/(m K). Py therefore displays negligible zero-field anisotropy in the thermal conductivity.

The zero-field thermal conductivity is in agreement with the expected result from Wiedemann-Franz calculations (measured resistivity $\rho = (50.3 \pm 0.6)$ $\mu\Omega\,$cm, expected from Wiedemann-Franz: $\rho = (51.5 \pm 1.4)$ $\mu\Omega\,$cm). The electrical AMR measured by the supplier amounts

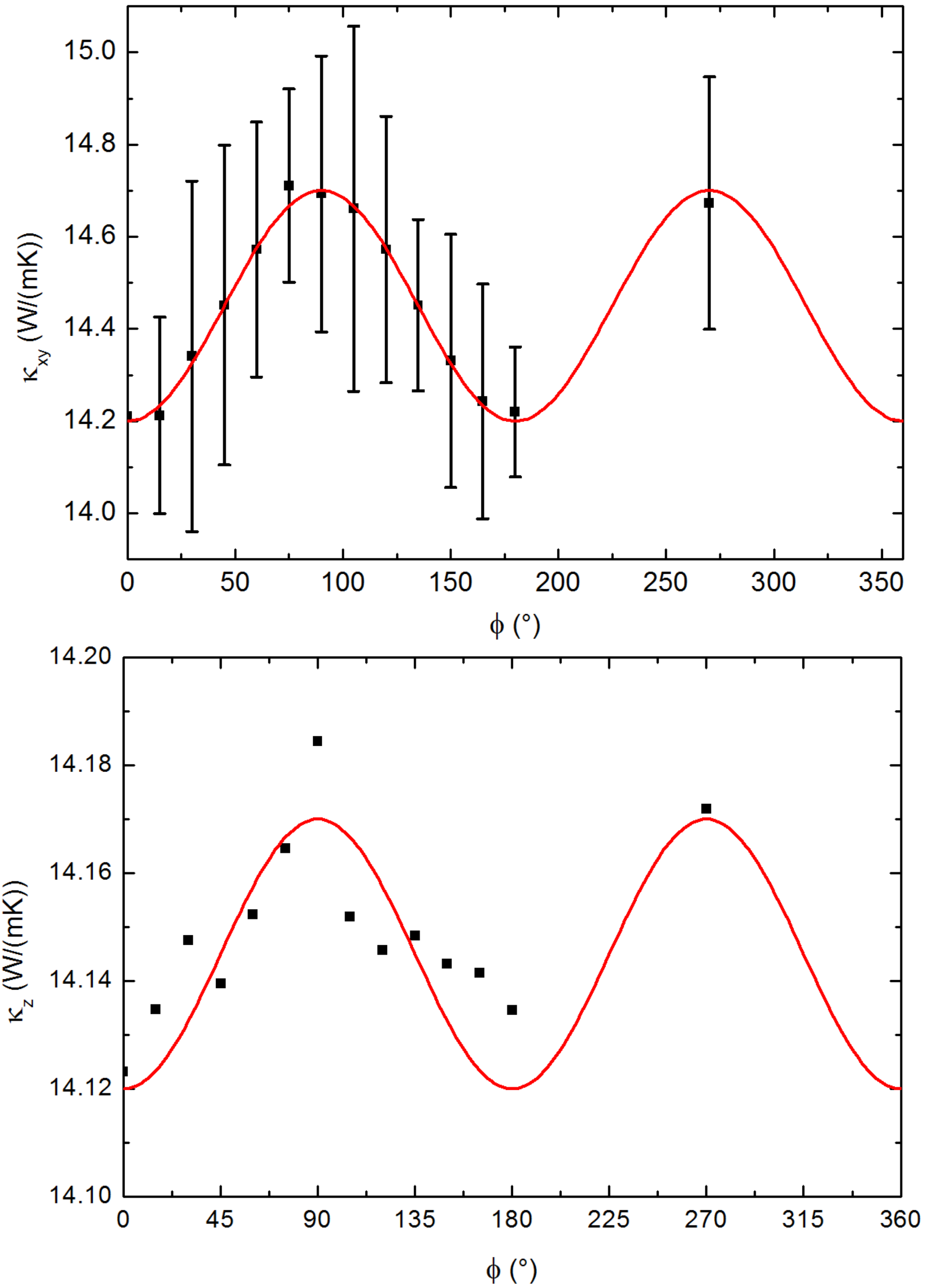

Figure 5.3.: Angle dependence of the thermal conductivity parallel (top) and perpendicular (bottom) to the film plane, κ_z. The red curve represents a $\sin^2(\phi)$ fit. Error bars are omitted for clarity in the k_z data ($\Delta\kappa_z \approx 0.2$ W/(m K)).

to 3.6%, which, since the MTR is equal to 3.4% also, possibly allows to conclude that the Wiedemann-Franz law may be valid in Py. Nevertheless, it needs to be kept in mind that the basis of this evaluation was the possibly unphysical thermal conductivity data obtained from the Si substrate by the slope method. Therefore, the agreement of the thermal conductivity measurement with the expectation from the Wiedemann-Franz law could be by chance and the data generally are not yet understood.

5.3. Discussion

The extraordinarily large reduction in the thermal conductance of Si that was observed in the previous section requires a careful discussion, as it apparently has not been measured previously by other groups. Also it has to be kept in mind that the reduction by an order of magnitude is implausible considering a magnetoresistance effect of approx. 2.5%, which was measure in a field of 100 mT as a consistency check.

There are several possibilities why such measurements can occur, even if they are reproducible in the same measurement setup. Not only can the latter be faulty or unreliable, but also the material itself can be of insufficient quality. For instance, the doping process could lead to a gradient in the dopant concentration and cause a top layer with extraordinarily high charge carrier concentration. The strong effect in a magnetic field is surprising also in so far as silicon and the dopant, boron, are not magnetic. Alternatively, the source of error could be a combination of such factors or of those discussed below.

To examine the origin of the unphysical MTR in Si, measurements of the field dependent thermal conductivity need to be performed on other Si wafers to exclude the silicon wafer as such and on other undoped and insulating substrates to exclude the measurement setup as a cause of the peculiar data. Measurements of the cross-plane thermal conductivity on MgO and $SrTiO_3$ (STO) substrates determined by the slope-method did not exhibit an effect of the magnetic field (Fig. 5.4), but rather field-independent signals, so that the experiment as such can be excluded as a reason for the strong effect observed here. The strong reduction in thermal conductivity in the presence of a magnetic field was measured not only in the samples consisting of a thick Py layer on top of the substrate, but also in the sample consisting of a thin Py layer on top of the substrate and a blank Si wafer. This order of measurement was chosen in order to prevent possible systematic errors.

Since three different Si wafers displayed comparable behavior, it is unlikely, but not impossible, that the wafers are at fault. To examine the wafer as the root cause, the thermal conductivities of a wafer produced by two different suppliers were measured. While wafers supplied by Sensitec displayed the anomalous behavior of the thermal conductivity with a small magnetic field, those supplied by Crystec and Singulus did not demonstrate such a behavior.

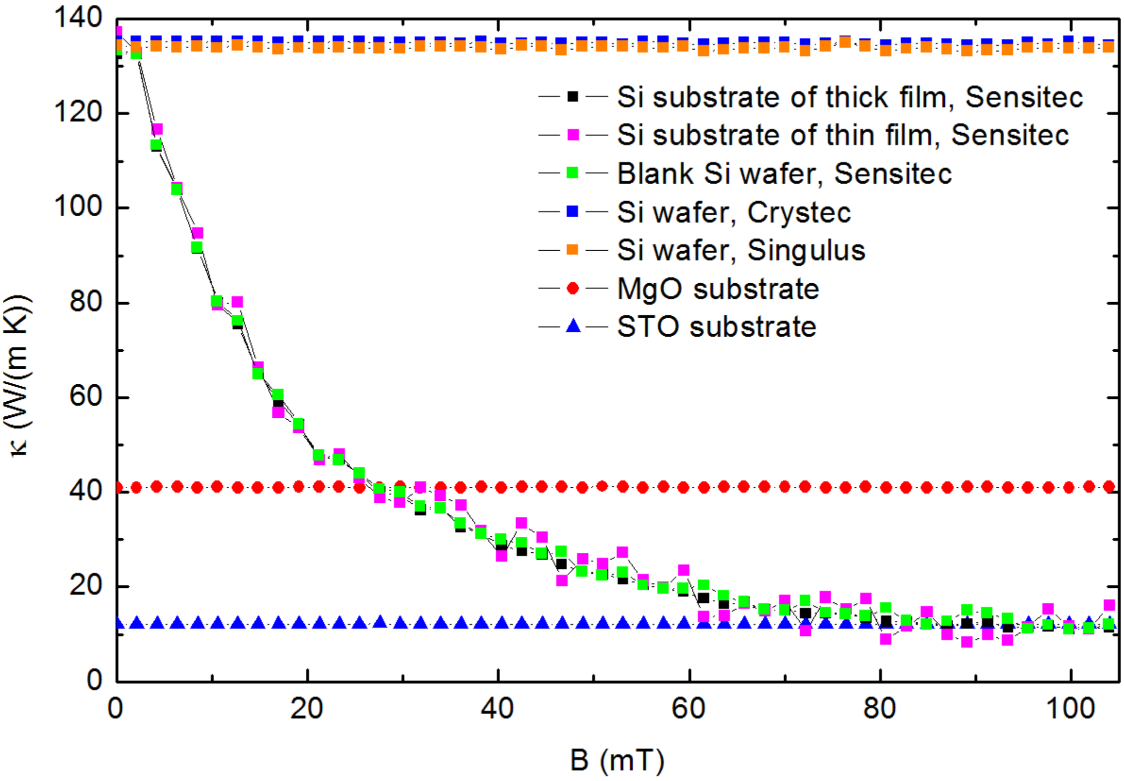

Figure 5.4.: Field dependent thermal conductance determined by the slope method of an MgO substrate (red), an STO substrate (blue), Si wafers supplied by Sensitec (sample with thick Py film: black solid square, sample with thin Py film: magenta open square, blank wafer: green open square), Si wafers supplied by Singulus (orange) and by Crystec (blue).

The silicon substrate is, by natural oxidation, capped with several nanometers of SiO_2. It is unlikely that this layer has an impact on the thermal conductivity for three reasons. Firstly, SiO_2 is nonmagnetic. Secondly, the layer typically is very thin compared to the thermal penetration depth of the 3ω method. As a third reason, the strong reduction effect was not only seen in the bare substrate but also in systems in which a film was grown on the substrate in-situ so that no SiO_2 layer should have formed.

In addition, a measurement of the Hall effect resulted in a charge carrier density of $n = (7 \pm 2) \cdot 10^{18}\ \mathrm{cm}^{-3}$. Considering the fact that no information about the dopant concentration was available from the supplier, such a high charge carrier concentration seems improbable. Since knowledge of the state of doping is imperative for the end user of strongly doped wafers, the lack of information about this quantity could possibly imply that the charge carrier concentration assumed by the supplier is far lower. Thus, there could be considerable doping inhomogeneities within the wafer that could lead to phenomena at an interface layer between the substrate and the Al_2O_3 layer.

In conclusion, the data presented in this chapter are not entirely understood, since the thermal properties of the silicon substrate are unclear. It is possible that, even though the abnormal effect was observed in multiple wafers, the batch of wafers obtained from Sensitec is in some way of lesser quality or contains (magnetic) impurities. Nevertheless, a MTR value in Permalloy consistent with the electrical AMR could still be extracted from the measurements assuming that the thermal conductivity values of the silicon substrate are accurate.

CHAPTER 6

THIN FILM THERMAL CONDUCTANCE OF YIG

Knowledge of the thermal properties of a system is fundamental in experiments including heat flow. In solids, heat is mainly transported by long-wavelength acoustic phonons. Therefore, even comparably thick 'thin film' systems encounter the generic issue that the heat conductivity is dependent on the film thickness, since long wavelength phonons will be scattered by surfaces or interfaces. For the electrical conductance, such an effect is described by the Fuchs-Sondheimer relation (Fuchs, 1938, Sondheimer, 2001). The derivation of this relation was simplified by the comparably easy access to experimental data, i.e. measurement of electrically conducting thin films on insulating substrates. In addition, due to the Pauli principle, only electrons at the Fermi surface participate in transport, so that a Fermi velocity and mean free path for the theoretical analysis can be computed.

For heat transport, the full phonon spectrum needs to be considered and the heat conduction of the substrate can usually not be eliminated in the experiment, thus rendering the determination of thin film heat conductance an ambitious task. This chapter presents an extraction of thickness dependent data for the heat conduction in thin film samples, in which the substrate has a heat conductivity comparable to that of the film material. Parts of this chapter were published as publication [P4].

6.1. Previous Research

The interaction of the spin degree of freedom with a thermal energy flow in a solid, spin-caloritronics, is a recent field of research (Bauer et al., 2012, Boona et al., 2014). Notably, YIG ($Y_3Fe_5O_{12}$) is of interest in spin-caloritronics, as it is a prototype material for spin dynamics experiments due to its very low damping, for temperature driven pure spin currents, and the spin Seebeck effect (Uchida et al., 2010, Schreier et al., 2013, Kehlberger et al., 2013). Particularly, the origin of the spin Seebeck effect is still controversial (Jaworski et al., 2011, Kehlberger et al., 2013, Geprägs et al., 2014), and its explanation includes magnon-phonon interaction. Here, the so far unknown temperature dependence of the thermal conductance of thin film YIG is needed to quantitatively determine the real temperature gradients in the investigated systems. Generally, crucial temperature gradients are calculated using bulk thermal conductivities of YIG (Schreier et al., 2013, Boona and Heremans, 2014), even though thin films of several hundred nm thickness are used. Determining the thin film thermal conductance of YIG thin films is of importance in order to quantitatively determine the real temperature gradients in the investigated systems and thus to quantify the spin Seebeck coefficients. This is all the more important, as recent efforts have begun to establish a metrology standard for the spin Seebeck effect (European Metrology Research Project: Spintronics and spin-caloritronics in magnetic nanosystems).

The quality of YIG films generally is determined by ferromagnetic resonance spectroscopy (FMR) measurements. The concept is based on the torque applied to the magnetic moments in the YIG film by an external field that causes the spins to precess, and is described by the Landau-Lifshitz equation. This precession frequency possesses an eigenfrequency, the ferromagnetic resonance frequency. The Kittel equation connects this eigenfrequency to the external field and the saturation magnetization of the sample. By extending the Landau-Lifshitz equation to include a damping term (see Section 2.2), phenomenological spin relaxation effects are taken into account in the model (Kittel, 2006). Finally, the full width at half maximum (FWHM) of the line width of the FMR resonance line can be correlated to the damping factor, the Gilbert damping constant α (Patton, 1984, Onbasli et al., 2014). As one of the main characteristics of high quality YIG is its low magnetic damping, the FMR line width is a measure of the sample quality (Onbasli et al., 2014).

Mostly for numerical reasons, as explained in Section 3.2, the conventional 3ω method to determine thin film thermal conductances fails in systems in which the film thermal conductivity is comparable to that of the substrate. Literature values vary between $(6\dots8)$ W/(m K) for bulk material at room temperature (Slack and Oliver, 1971, Padture and Klemens, 1997, Hofmeister, 2006), but Padture and Klemens (1997) discuss that their result of approximately 6 W/(m K) possibly underestimates the true value by up to 1.5 W/(m K). To conserve the validity of the classical 3ω approach, the thermal penetration depth needs to be smaller than the film thickness, which requires careful electron beam lithography and a high-frequency (1 MHz) lock-in amplifier, which are typically not available to many institutes. Conveniently, the Bayesian technique introduced in Section 3.3 is capable of determining the thermal conductance in the low-frequency regime and also in substrate-film combinations that are not directly analyzable by the differential 3ω method. On the other hand, the thermal conductance of the film is measurable at suitable higher frequencies that reduce the thermal penetration depth. This chapter demonstrates that the Bayesian technique used at low frequencies and the classical slope-based technique applied to the high-frequency regime come to results that are compatible within their error margins. Using both techniques the thermal conductance of gadolinium iron garnet (GGG) and yttrium iron garnet are determined at temperatures below room temperature.

While there exist theoretical calculations of the magnon thermal conductivity in YIG at low temperature (Kumar, 1982, Rezende et al., 2014), the results disagree by orders of magnitude with respect to experimental results (Boona and Heremans, 2014). According to Callaway and Boyd (1964), magnetic impurity scattering has a strong effect by reducing the magnon thermal conductivity from its (boundary limited) value. Already in 1962, Lüthi measured the magnon thermal conductivity in bulk YIG and found a value of around 1 W/(m K) at 5 K and of 0.4 W/(m K) at 1.5 K (Lüthi, B., 1962). Measurements of Pan et al. (2013) demonstrated that the magnon thermal conductivity in YIG is below 0.06 W/(m K) at temperatures below 1 K, where the magnonic contribution makes up more than 70% of the thermal transport. As all these experiments were performed on bulk YIG samples, new and accurate experimental thin film global and magnon thermal conductance values of YIG can be a great advantage and of great importance in the field of spin caloritronics.

6.2. Thickness Dependence and Magnetic Field Contribution

In this section data on the thermal conductance of YIG are presented. The YIG samples used were liquid phase epitaxy (LPE) and pulsed laser deposition (PLD) grown films on (5$\times$10) mm GGG substrates. The film thicknesses of the first batch of samples were $6.7\ \mu\mathrm{m}$ and $2.1\ \mu\mathrm{m}$ (LPE) and $190\ \mathrm{nm}$ (PLD). The second batch contained samples grown by LPE with thicknesses of 1.51 $\mu\mathrm{m}$, 3.08 $\mu\mathrm{m}$, 7.78 $\mu\mathrm{m}$, 12.01 $\mu\mathrm{m}$, 22.83 $\mu\mathrm{m}$ and 50.66 $\mu\mathrm{m}$. The gold layer, from which the 3ω heater structure was patterned, was grown by DC sputter deposition. AFM measurements show the YIG film roughness to be below 1 nm (Fig. 6.1). Figure 4.8 had displayed a $\theta-2\theta$ x-ray diffraction (XRD) scan of a sample composed of 50 nm of gold on 20 nm of $\mathrm{Al_2O_3}$ grown on a MgO substrate and demonstrated that the material is grown in the fcc structure. The fit to the XRR data (Fig. 6.2) very well reproduces the region around the angle of total reflection and allows the extraction of the Au film roughness of 0.7 nm. The heater strip (thickness: 50 nm) is rectangular in shape with a length of 1 mm between the voltage contacts and a width of 20 μm, which yields a four-point room temperature specific resistivity of Au of $2.6 \cdot 10^{-8}\ \Omega\mathrm{m}$. The temperature dependence of its resistance and temperature coefficient of resistance are shown in the inset of Fig. 6.3 and follow the Bloch-Grüneisen law. Both the absolute values and the temperature at which the $R(T)$ curve saturates at low temperature agree with previous results (see e.g. the review by Matula (1979)). In particular, the slope of the resistance vs. temperature is a measure of the signal resolution, so that below 10 K no meaningful 3ω measurement can be performed. Due to the low temperature coefficient below

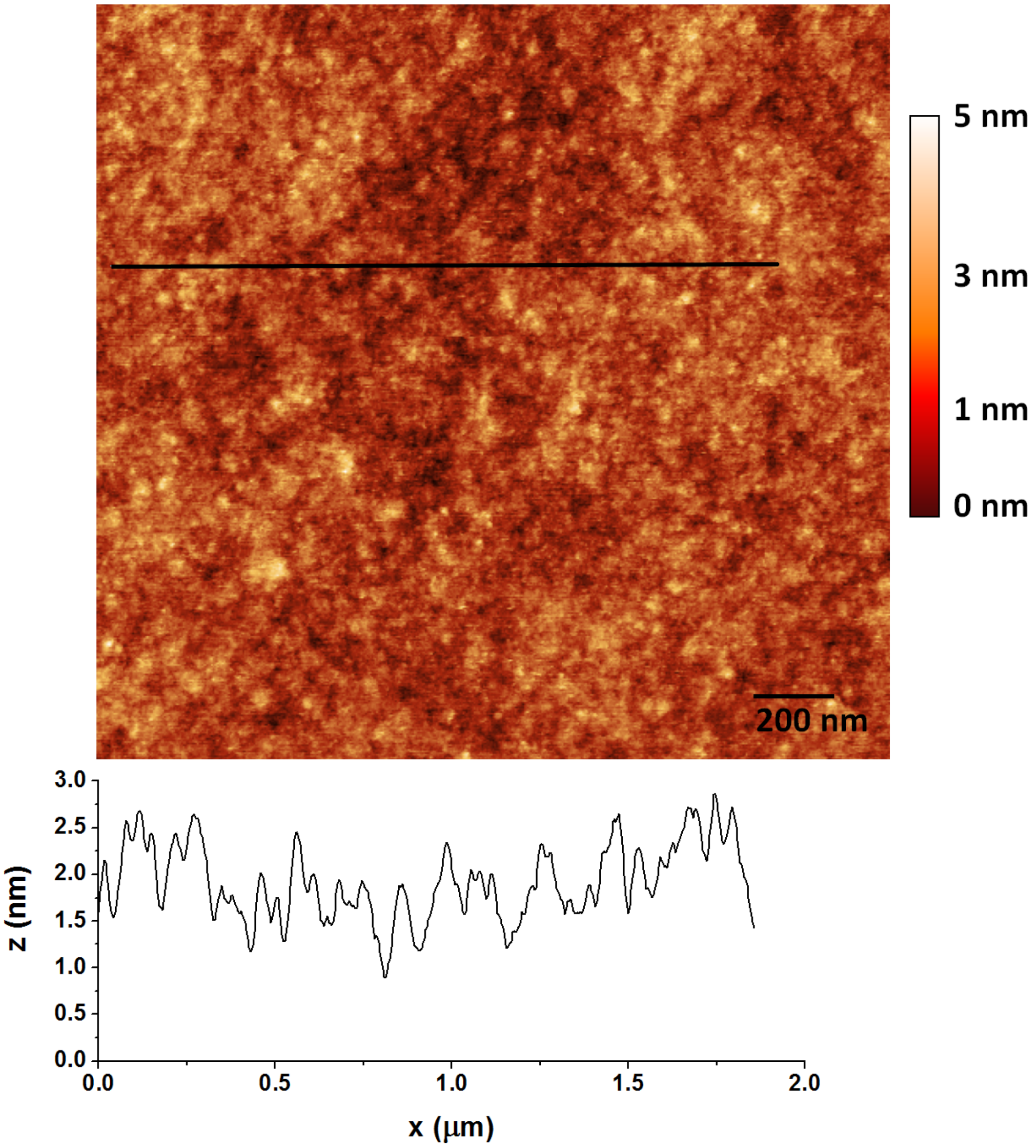

Figure 6.1.: Atomic Force Microscopy scan of a 150 nm thick YIG film (top). The black line indicates the position of a line scan presented below.

10 K a measurement of the thermal conductivity is only possible above this temperature.

The two-dimensional fitting algorithm presented in Section 3.3 can only be applied to the temperature dependent data, if the temperature dependence of the specific heat and the density are taken into account. Geller et al. (1969) analyzed the coefficient of thermal expansion for a number of garnets including GGG and YIG and found a change Δa_0 in the pseudo-cubic lattice constant in GGG fitting

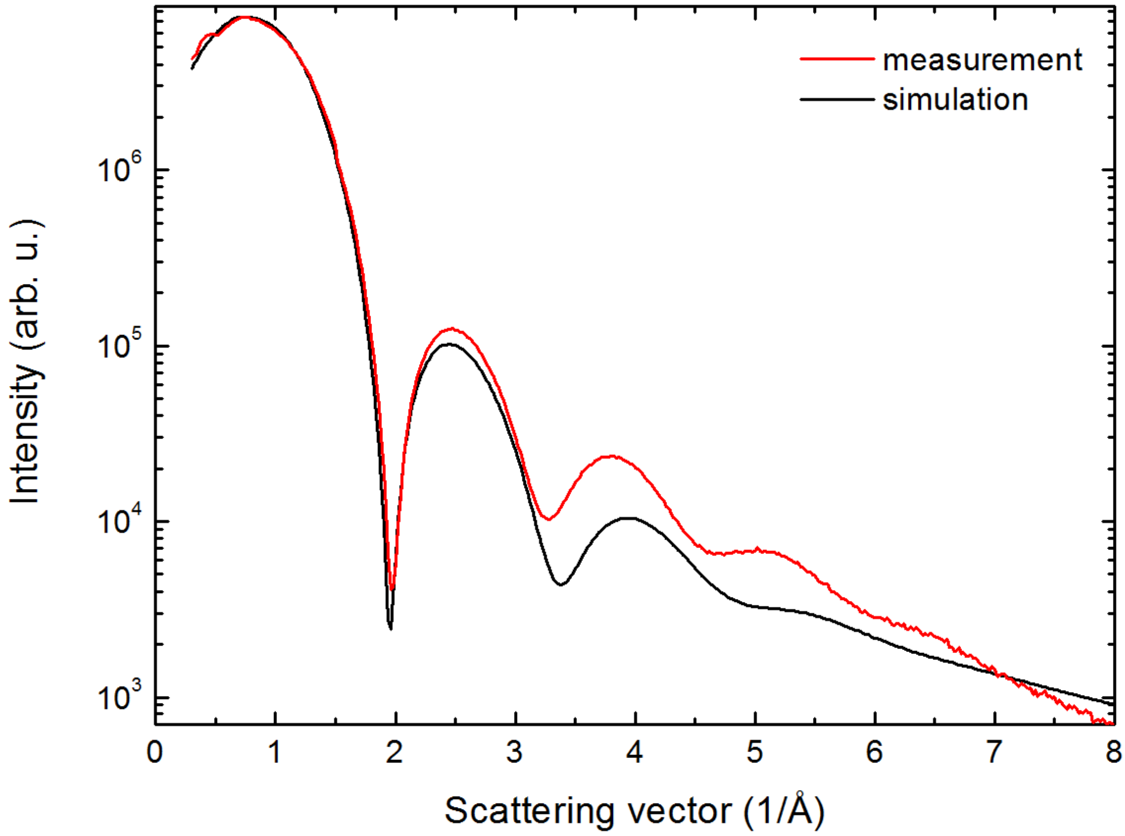

Figure 6.2.: X-ray reflectivity curve (red) and fit (black) of a 5 nm thick gold layer on a GGG substrate.

$$\frac{\Delta a_o}{a_0} = 2.2 - 7.1 \cdot 10^{-6} T + \frac{2.5 \cdot 10^{-9}}{2} T^2 - \frac{0.03}{T}. \tag{6.1}$$

Using furthermore the classical Debye T^3 law, the specific heat capacity can be approximated as

$$C_P(T) = C_P(300\ \mathrm{K}) \left(\frac{T}{300\ \mathrm{K}}\right)^3 . \tag{6.2}$$

Inserting this into Eq. 3.32 and calculating the expectation values for the thermal conductivity results in almost identical cross-plane and in-plane values (which is not suprising given the complex unit cell).

A low-frequency measurement of the thermal conductance of a GGG substrate was used to supply the algorithm with the thermal conductance values of the substrate. While the slope method yielded a cross-plane thermal conductance for GGG of $\kappa_z = 7.8$ W/(m K), the two-dimensional method resulted in $\kappa_z = (8.6 \pm 1.6)$ W/(m K). High-frequency regime data were taken on two YIG samples to determine the room temperature thermal conductance of

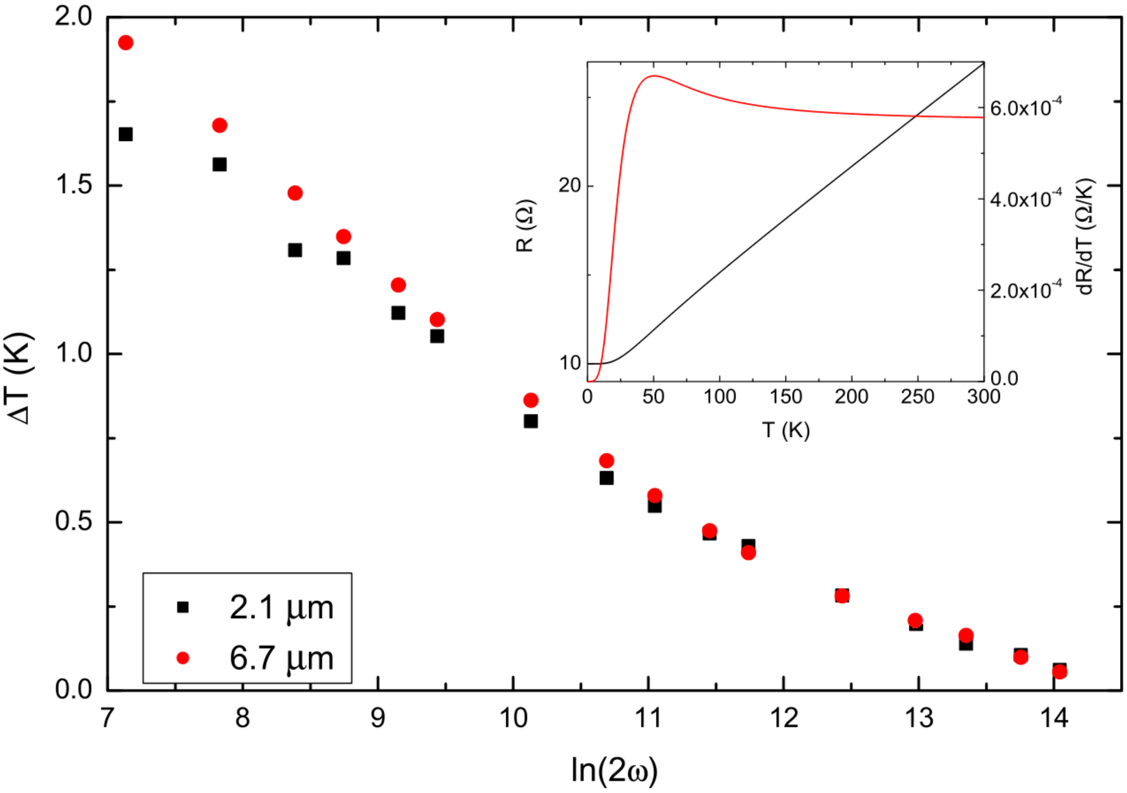

Figure 6.3.: The temperature oscillation in the heater structure in dependence of $\ln(2\omega)$ measured between 100 Hz to 100 kHz with ω the dimensionless angular frequency measured in Hz. The inset shows the temperature dependence of the resistance of the Au heater strip (black) and its temperature derivative (red).

YIG. Above a certain frequency the reduced thermal penetration depth causes the method to be sensitive to the probed film only. In the high-frequency range above 50 kHz the data of the 6.7 μm and 2.1 μm films overlap, indicating that the thermal penetration depth is smaller than the thickness of the thinner film.

The fitting algorithm presented in Section 3.3 was applied to the low-frequency data below 2 kHz. The process resulted in the probability distribution function (PDF) displayed in Fig. 3.8 for a room temperature measurement. A highest density region is clearly visible. Evaluation of the joint probability distribution via the respective marginal PDFs led to values of $\kappa_{xy} = (9.5 \pm 1.1)\ \mathrm{W/(m\,K)}$ and $\kappa_z = (8.5 \pm 0.6)\ \mathrm{W/(m\,K)}$. Both values of the thermal conductance are larger than the literature value, which does not lie within the error of the in-plane value determined by the algorithm. A possible reason is given by the small size of the sample, which, compared to bulk material, should contain less lattice defects and therefore possess an increased thermal conductance. In general, the 3ω method is prone to substantial systematic uncertainties of up to 10%, so that a difference between values should not be

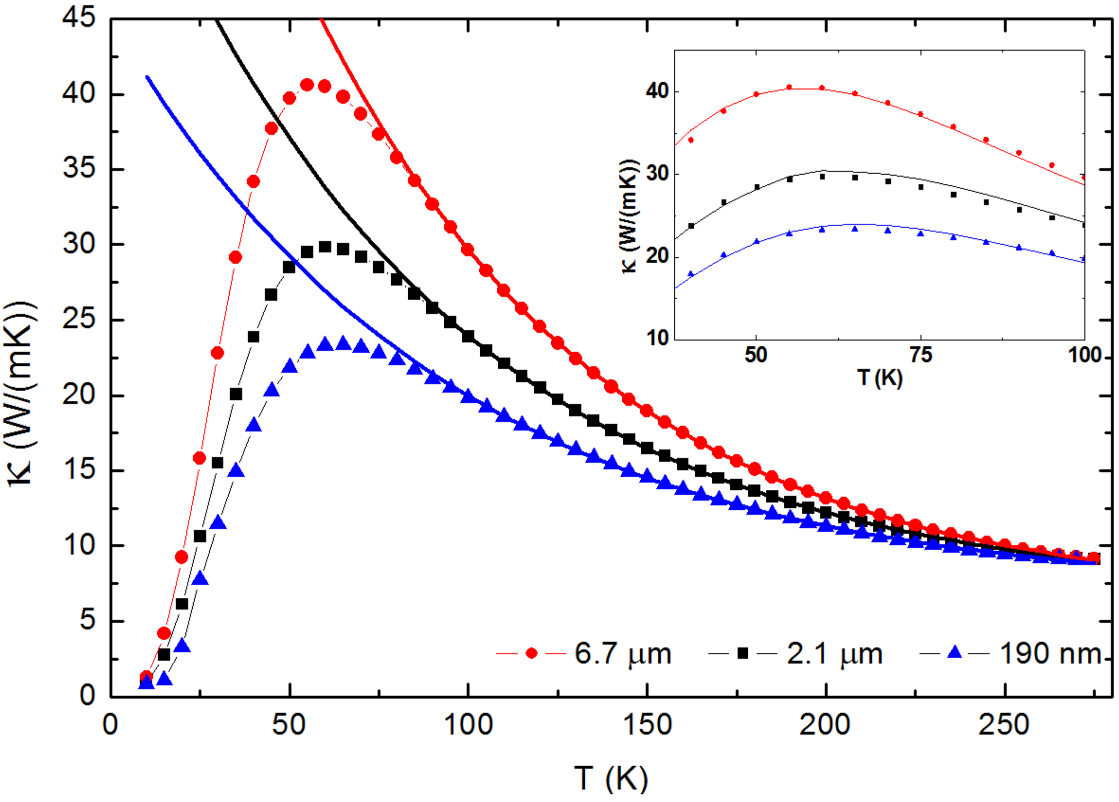

Figure 6.4.: Temperature dependent thermal conductances of YIG samples (first batch: 6.7 μm (red circles), 2.1 μm (black squares) and 190 nm (blue triangles)) and exponential fits to the high-temperature regions (solid lines). The inset displays the fit by the Callaway model around the maximum.

overrated. In addition, Kapitza interface thermal resistances have not been taken into account. The fact that the slope-based values of the thermal conductivity of YIG and the result of the presented algorithm agree well implies that the new method is capable of providing physically sound results.

The Bayesian approach is capable of providing temperature dependent thermal conductance values down to low temperatures. Fig. 6.4 shows the thermal conductance of a first batch of YIG films with thicknesses of 6.7 μm, 2.1 μm and 190 nm. A clear peak in the thermal conductance is visible at 57 K, 60 K and 65 K, respectively. At high temperatures, Umklapp scattering is the dominant factor that reduces the thermal conductance and the thermal conductances are expected to be thickness independent, while the peak in the thermal conductance is a measure for the length scale at which phonon boundary scattering becomes predominant. Therefore, a smaller film thickness should lead to a shift of the peak towards higher temperatures and, correspondingly, to lower peak values of the thermal conductance. This is observed in the data, which provide peak thermal conductances of approximately 41 W/(m K), 30 W/(m K) and

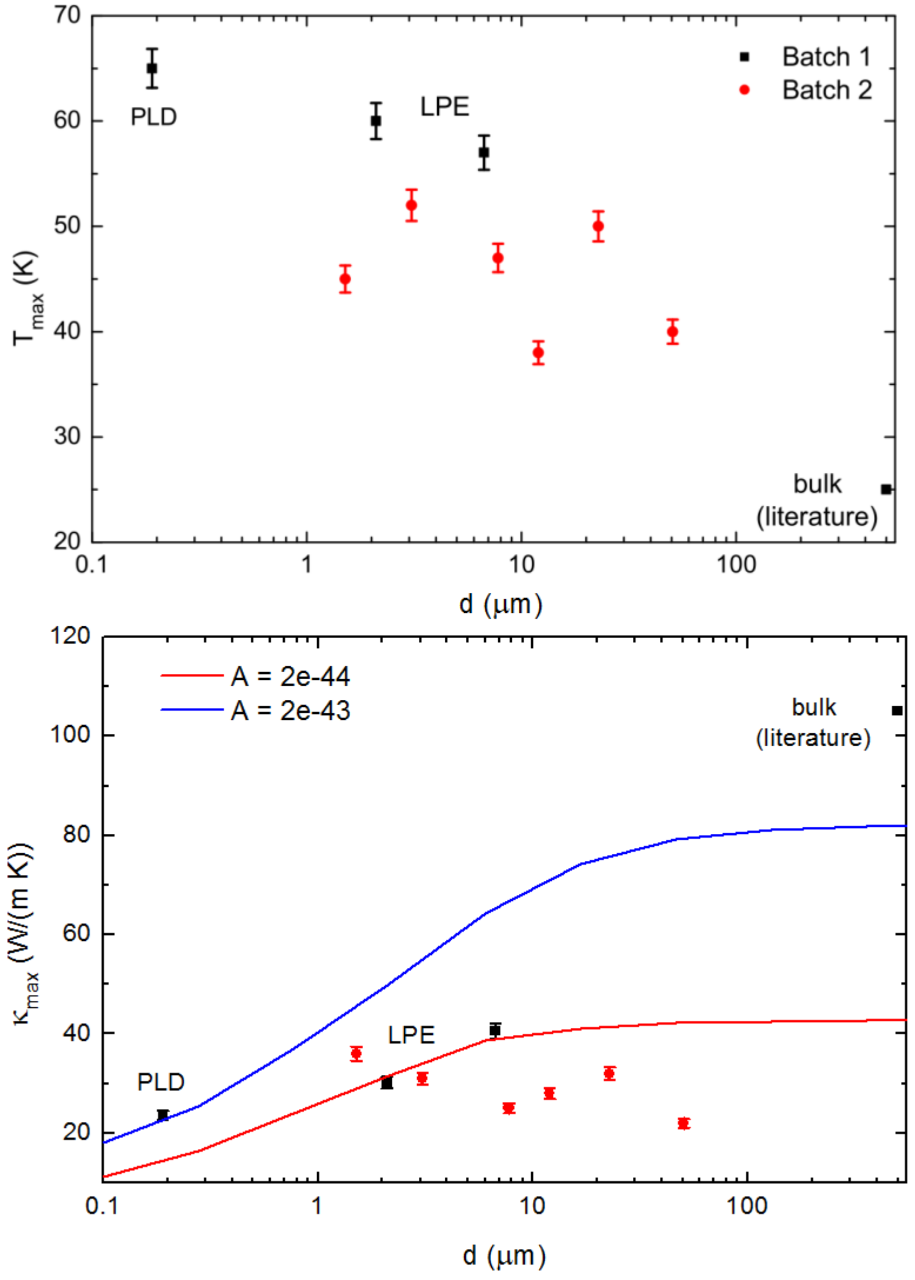

Figure 6.5.: Peak temperature $T_{\max}$ (upper plot) of the thermal conductance and peak value $\kappa_{\max}$ (lower plot) as function of film thickness. The data point at 500 μm is taken from Boona and Heremans (2014). The black squares result from the first batch of samples, while the red circles correspond to the second batch of samples. The error bars are derived from the sample-to-sample variation of $T_{\max}$ and $\kappa_{\max}$. The blue and red lines in the lower plot indicate the dependence on the defect concentration parameter of the maximum in the thermal conductivity at constant scattering parameters other than the thickness effect.

24 W/(m K), respectively. In bulk material Boona and Heremans (2014) found a peak thermal conductivity of approximately 110 W/(m K) at 25 K. The high temperature region of the data fits an exponential decay close to the maximum as is expected from phonon transport theory.

The second batch of films grown by LPE with thicknesses of 1.51 $\mu\mathrm{m}$, 3.08 $\mu\mathrm{m}$, 7.78 $\mu\mathrm{m}$, 12.01 $\mu\mathrm{m}$, 22.83 $\mu\mathrm{m}$ and 50.66 $\mu\mathrm{m}$ did not confirm the behavior seen in the first batch. It can be expected that films approaching the bulk state approach bulk values of κ, but this effect is not observed in the data (Fig. 6.5). There is no apparent systematic trend, even though all thermal conductivity curves can be fitted individually using the Callaway model, but with strongly varying defect concentrations. The sample-to-sample variation of the maximum thermal conductivity, determined from two randomly chosen samples within one wafer, amounts to 8% and that of the maximum temperature to 6%. This confirms the reproducibility of the results within uncertainty limits. The data imply that the quality of the film, i.e. the defect concentration, is a vital piece of information required to understand the thin film thermal conductance of YIG. At room temperature the values of the thermal conductance obtained using the model are slightly larger than the literature value.

The fact that thin film thermal conductances can be lower by a factor of three to five than those of bulk YIG implies that temperature gradients estimated in thin film spin-caloritronic experiments can differ from their actual values significantly. Fig. 6.5 summarizes the thickness dependence of the peak temperature and the peak thermal conductance and indicates that it can be necessary to implement thin film thermal conductances in the evaluation of spin-caloritronic data. The model data (red circles and blue lines) are calculated using the Callaway model of thermal conductivity (Callaway, 1959), which models the thermal conductivity in terms of relaxation times (see Section 2.2). In particular, scattering of phonons with frequency ω at point defects is described by $\tau_d^{-1} = A\omega^4$ with A a material specific constant proportional to the defect density.

While the data for the first batch of samples grown by LPE can be explained using a single set of relaxation times and only varying the thickness-dependent boundary scattering relaxation time based on the actual thickness of the films, the data taken from the thinnest film deviate from this model. A different parameter set is required, in which the strongest difference between the samples is a different defect concentration given by the model parameter A. The difference of an order of magnitude in both values of A used to describe the films grown by PLD and LPE implies a large difference between the defect densities in films grown by both techniques. The defects do not need to be of the same type in both sets of samples and a difference in film quality (PLD resulting in a larger defect concentration) is to be expected. In the case of the bulk sample there may be additional influences that are unknown, as the sample was measured by Boona and Heremans (2014). This implies that the quality of the film, given by the defect concentration, is a vital piece of information necessary to understand thin film thermal conductance of YIG. Lattice strain as a possible reason for the large difference in sample quality can be excluded. The lattice constants of YIG, 12.376Å, and that of GGG, 12.383Å, imply a strain of 0.06% (Sposito et al., 2013). Strain effects at the interface between substrate and film are expected to have a negligible influence on the thermal conductivity, as the study of Alam et al. (2012) suggests sub-percent changes in κ for less than 0.1% strain.

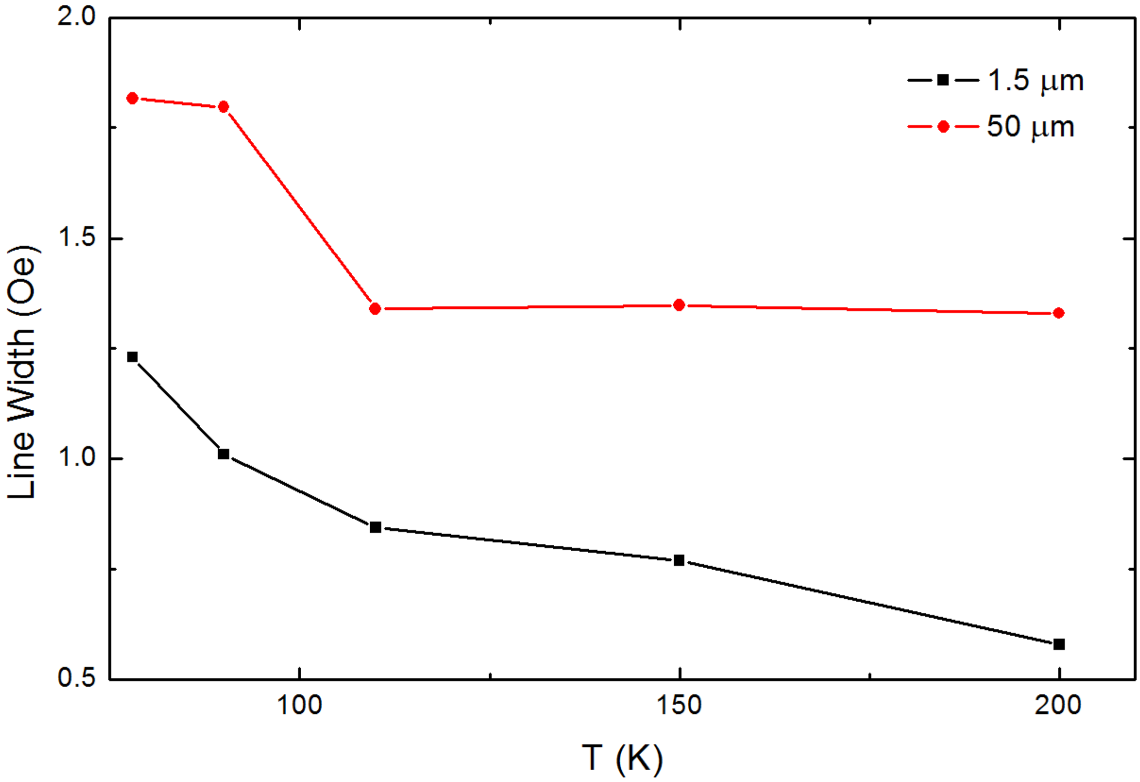

Figure 6.6.: FMR line width of YIG thin films with a thickness of 1.5 μm and 50 μm, respectively, taken at 9.6 GHz at the university of Halle by Tim Richter. The data were taken by Tim Richter at the university of Halle.

The FMR line width is frequently used as a marker for the sample quality, as was explained in the previous section. Fig. 6.6 shows the FMR line width of two samples with a thickness of 1.5 μm and 50 μm, respectively, taken at 9.6 GHz. The line width decreases with increasing temperature, which is consistent with previous measurements on 1 μm thick YIG films (Vittoria et al., 1985). Unfortunately, no FMR data could be taken at temperatures below 80 K due to the restriction of the setup to nitrogen cooling, so that the strong increase in slope cannot be correlated to the increase in thermal conductivity to lower temperatures. Vittoria et al. (1985) had observed an increase towards lower temperatures comparable to the measurements in Fig. 6.6. Of particular interest, Vittoria et al. (1985) observed a pronounced maximum in the line width at 50 K. Generally, here the thicker sample shows a larger line width, which is inconsistent with the general trend that with increasing film thickness the sample quality increases and therefore the line width decreases (Onbasli et al., 2014). Thus, the thicker sample could be of lower quality than the thinner sample. The defects leading to magnetic damping, however, do not need to be identical to those relevant for phonon scattering, so that these line width data are only an indication as to why the thermal conductivity maxima do not behave monotonously with the sample thickness.

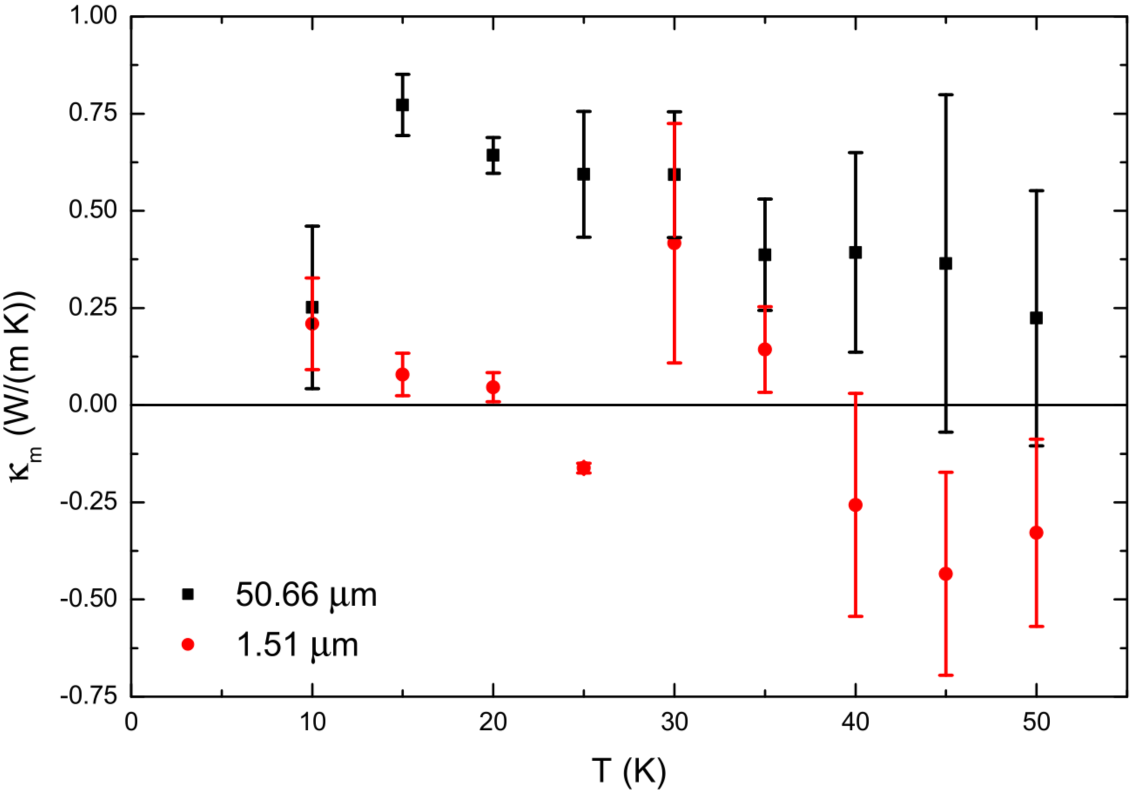

Figure 6.7.: Magnetic field dependent contribution of the thermal conductivity of YIG films with thicknesses of 50.66 μm and 1.51 μm.

Finally, Fig. 6.7 displays the difference in thermal conductivity κ_m of YIG films between 10 K and 50 K in samples with thicknesses of 50.66 μm and 1.51 μm when in zero field and in a magnetic field of 8 T, which freezes out the magnonic contribution (Boona and Heremans, 2014). Statistical errors are determined by sampling 100 data points per temperature point, which is necessary due to the small magnitude of the difference. Our data show that κ_m may be thickness dependent and that the magnetic field may affect the thermal conductivity differently in thick films, while the thin film does not show a contribution significantly different from zero. Above 40 K the difference cannot be distinguished from thermal noise. The data suggest that the temperature of the largest difference is at approx. 15 K in the thick film, while there is no significant difference in the thin film. The point of largest difference is at a temperature much lower than the peak thermal conductivity, which is in agreement with Boona and Heremans

(2014). Generally, it is inferred that the magnetic field dependent contribution to the thermal conductivity below 50 K does not exceed 1 W/(m K).

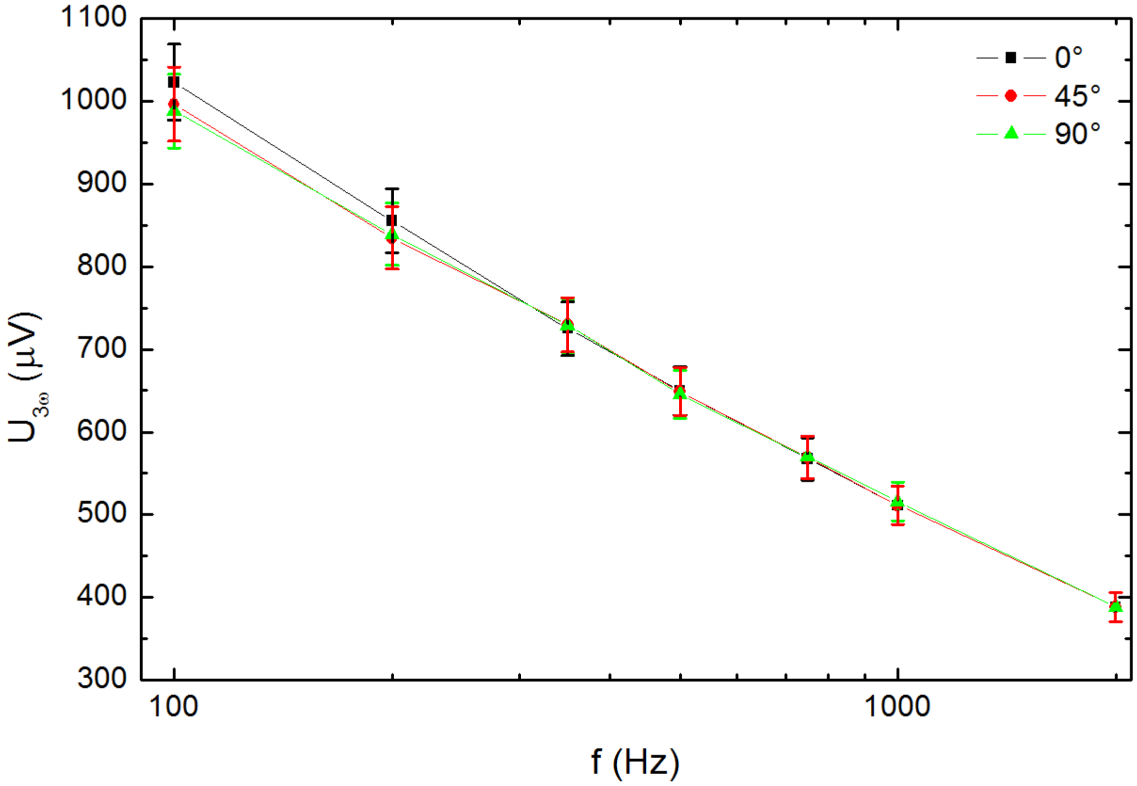

Figure 6.8.: Angle dependent 3ω measurements on a 190 nm thick YIG sample on GGG taken at 0°, 45° and 90°.

In principle, it is possible that the spin Hall effect (SHE) influences the magnetic field contribution of the thermal conductance by injecting spin currents into the samples. There are two main reasons why the SHE can be neglected in the measurements. Firstly, the spin Hall angle is a measure of the strength of the expected SHE. In gold the previously measured spin Hall angles are at least one order of magnitude, if not two, smaller than in platinum (Isasa et al., 2015). Measurements by Sebastian Gönnenwein do not show a spin Hall angle in gold significantly different from zero (Gönnenwein, private communication). Therefore, no spin Hall effect contribution is to be expected in our measurements. Secondly, the resistance and therefore the measurement of the thermal conductivity could have been manipulated by the spin Hall magnetoresistance (SHMR). The SHMR displays a characteristic angular $\sin^2\phi$ dependence (Nakayama et al., 2013, Althammer et al., 2013, Meyer et al., 2014). The 3ω signal was therefore measured in a magnetic field of 1 T at angles of 0°, 45° and 90° (Fig. 6.8). As there is no significant difference between the data obtained at these three angles, no observable SHMR and therefore negligible SHE influence is present in these measurements.

In addition the inverse spin Hall effect (ISHE) can possibly affect the signal in the measurement device. However, the injection efficiency decreases inversely with the film thickness (Althammer et al., 2013), so that at an Au thickness of 50 nm no significant spin Hall manipulated signal is to be expected. Secondly, the ISHE is not expected to be measurable at 3ω, as it depends on the temperature gradient, that influences the second harmonic. Therefore, the inverse spin Hall effect can be neglected.

Finally, in the experiments including an external field the magnetization induced by the Oersted field generated by the current in the Au strip will not significantly manipulate the thermal conductivity, as the fields generated by sub-Amp currents are much smaller than the external field of 8 T.

In conclusion, the two-dimensional 3ω technique, assisted by a Bayesian data evaluation scheme, was employed to YIG samples grown on GGG by different methods. It was demonstrated that the method allows the extraction and interpretation of thermal conductivity data between 10 K and room temperature. The results agree with bulk values at room temperature, but differ significantly towards lower temperature, where the thermal conductance is shown to be significantly reduced at small thicknesses compared to bulk material. In particular, in films grown by LPE the effect of the defect density exceeds that of the expected thickness dependency. Therefore, an analysis of the thermal conductivity is recommendable prior to spin caloritronic experiments at low temperature.

CHAPTER 7

CONCLUSION AND OUTLOOK

The goal of this thesis was to shed light on the influence of spin caloritronic effects on heat transport and to develop techniques used to study thermal transport further. In particular, the 3ω method was applied and researched to achieve four objectives.

The influence of a magnetic field on the thermal conductivity perpendicular to the film plane in $\mathrm{La}_{0.67}\mathrm{Ca}_{0.33}\mathrm{MnO}_3$ (LCMO) was studied. While a significant effect of the magnetothermal resistance (MTR) was expected due to the colossal magnetoresistive properties in LCMO, the expectations were exceeded by the actually measured effect. A clear dependence of the thermal conductance on the magnetic field was observed. An analysis of the effect of oxygen stoichiometry, film thickness and the choice of the substrate on the MTR showed agreement with the Wiedemann-Franz expectation in unstrained (annealed) LCMO, but not in strained (as-grown) samples. Raman spectroscopy revealed that this is owed to a strong rotational distortion of the oxygen octahedra, affecting the coupling of the spin and charge degrees of freedom at the manganese site. The results show that in systems with such strong electron-lattice interaction manipulation of the phonon spectrum is possible by magnetic fields acting on the electron spin.

Furthermore, it was demonstrated that the original 3ω method is inapplicable in spin-caloritronic contexts and at low temperatures, as frequently the thermal conductivities of the film and the substrate are similar in magnitude. To overcome this issue, a method was developed that determined the thermal conductance of thin film samples simultaneously based on a model of two-dimensional heat transport, which is solved by a Bayesian technique. This technique was applied to two systems, namely Permalloy, that displays anisotropic magnetoresistance (AMR), and $\mathrm{Y}_3\mathrm{Fe}_5\mathrm{O}_{12}$ (YIG), that is commonly used in spin caloritronic experiments due to its low magnetic damping.

Concerning Permalloy, as a third goal, the magnetic field is shown not only to have an impact on the in-plane electrical resistance, but also on the thermal conductivity as expected from the Wiedemann-Franz law. The effect, however, is small and only shows a magnitude of 3.4%. Changes in the thermal conductivity of this smallness are generally believed not to be measurable by the 3ω method. By using large sampling rates and the Bayesian algorithm that only allows the measurement of the in-plane thermal conductivity to begin with the effect of the AMR on the thermal conductivity was detected. Nontheless, this conclusion needs to be taken with caution, since the evaluation of the thermal conductance of Permalloy relies on a prior measurement of the thermal conductivity of the Si substrate that could be considered to be erroneous.

Also the fourth goal, a measurement of the low temperature thermal conductance of thin film YIG, was achieved by means of the Bayesian technique. For thin film YIG a room temperature thermal conductance of $\kappa_z = (8.5 \pm 0.6)\ \mathrm{W/(m\,K)}$ with very low anisotropy was found. The low temperature behavior proved not to depend prominently on the dimensions of the sample, but rather on the defect concentration in the YIG films. The large influence of defects was demonstrated in films grown by pulsed laser deposition and liquid phase epitaxy, and was shown for film thicknesses between 190 nm and 50 μm. In addition, the magnetic field dependence of the thermal conductance was studied between 10 K and 50 K. No significant effect was found, and only an upper limit of a magnetic field dependent thermal conductivity of 1 W/(m K) can be given.

Of course, the research conducted here is far from having fully explored the importance of the thermal conductivity in the field of spin caloritronics. For instance, Kapitza interface resistances have not been introduced into the Bayesian model. Then, a particularly topical research area is the thermal conductivity of the magnon sub-system in YIG, as it is closely linked to other research, such as that on the spin Seebeck effect. The effort described in the last part of Section 6.2 should be expanded in a systematic study of the magnetic field contribution to the thermal conductance of thin film YIG. In order to do so it is necessary to replace gold as the material used for the 3ω heater by a different metal, that displays an adequate slope in the temperature dependent resistance below 10 K. Finally, an interesting link to the magnon system of a magnetic layer on top of a nonmagnetic layer can be established by studying spin pumping. The influence of the spin Hall effect and spin Hall magnetoresistance on the thermal conductivity could be studied, e.g. by depositing platinum and gold heater structures on the same sample with and without an aluminum buffer layer.

Research on the role of thermal conductivity in spin caloritronics has only begun. Facilitated by the Bayesian algorithm research on a variety of material systems and phenomena is now possible.

APPENDIX A

TEMPERATURE PROFILE OF THE PLD HEATER

In order to produce a homogeneous thin film the substrate temperature needs to be constant over the entire deposition area. The figure on the following page shows the heater temperature profile at a heating power of 58 W, 93 W and 136 W measured by a pyrometer as well as the mean temperature at the corresponding power setting. While the standard deviation of the temperature throughout the heater remains at approx. 25 K independent of the heating power, the peak deviation from the mean value increases with the power. In order to reach 800°C the maximum available power is required, which leads to spatially inhomogeneous heating of the substrate. Inhomogeneous heating in turn leads to inhomogeneous film growth and quality, that results in different metal insulator transition temperatures at different locations on the sample. Fixing a copper plate underneath the substrate and gluing the plate to the heater allows a smooth temperature distribution over the entire substrate area and leads to homogeneous film growth at high substrate temperatures. Through a subsequent modernization of the PLD setup using a laser heated substrate holder this procedure became redundant.

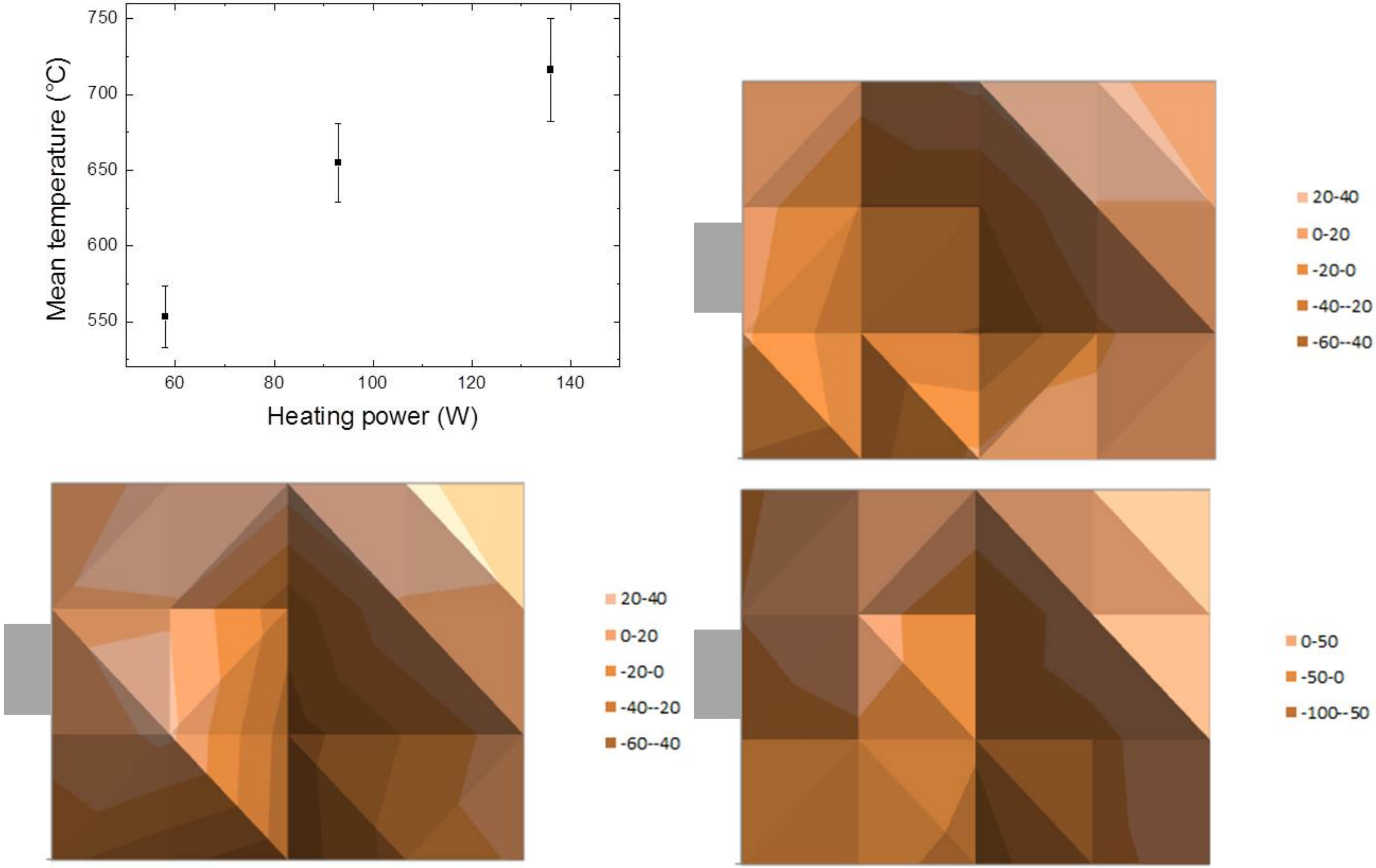

Heater temperature profile; the grey rectangle on the left side of the heater represents the coupling to the transfer arm. The top left figure displays the mean temperature of the heater as a function of the heating power. The top right, bottom left and bottom right figures illustrate the temperature deviation in °C from the mean temperature at heating powers of 58 W, 93 W and 136 W, respectively.

LIST OF FIGURES

1.1. Idea of spin caloritronics. 3

1.2. Charge current with arbitrary spin orientation (top) and pure spin current (bottom). In the former case no angular momentum is transfered, whereas in the latter case no net charge is transported. 4

2.1. The resistance (black) and the numerical temperature derivative of the resistance (red) as a function of temperature of a metal with a Debye temperature of 140 K, a constant $A = 32$ and a saturation resistance of 10 Ω. 10

2.2. Influence of Normal, Umklapp, boundary and defect scattering on the thermal conductivity of Si. Reprinted figure with permission from Glassbrenner and Slack (1964), copyright 1964 by the American Physical Society. 17

2.3. Constituents of the Callaway model of thermal conductivity. The bosonic nature of phonons, the Debye approximation and a parametrization of the scattering processes in terms of relaxation times are inserted into the Boltzmann equation, which is solved to give a temperature and sample thickness dependent thermal conductivity. 19

2.4. Influence of Gilbert damping on the thermal conductivity of a hypothetical magnetic insulator. The suppressing effect of increased magnon phonon scattering on the thermal conductivity is clearly visible in comparison with the model, in which the damping term is not included (no coupling). Values around $\alpha_G = 10^{-4}$ are physical for $Y_3Fe_5O_{12}$. 21

2.5. Phonon (black solid line) and magnon (red solid line) dispersion relations normalized to unity at π/a and the respective fits to leading order (dotted lines). 22

3.1. The one-dimensional (original) 3ω method assumes thermal transport parallel to the sample surface. Information about the thin film is obtained from the difference between sample (left) and reference sample (right). The gold layer on top is used as a measuring device for the temperature increase ΔT. 26

3.2. Overview of the main options for 3ω measurements. 27

3.3. Measured frequency dependency of $U_{3\omega}$ of a 2.1 μm thick film of $Y_3Fe_5O_{12}$ on a $Gd_3Ga_5O_{12}$ substrate. The frequency-dependent transition between a penetration depth larger than the film thickness to smaller than the film thickness is clearly visible at approximately 10^4 Hz. 28

3.4. Temperature oscillations measured at frequencies 100 Hz and 1 kHz in a sample of 6.7 μm thick YIG ($Y_3Fe_5O_{12}$) grown on GGG ($Gd_3Ga_5O_{12}$). The difference of the temperature oscillations clearly approaches zero for low temperatures. . . 34

3.5. Black lines: The temperature oscillation ΔT as a function of the in-plane thermal conductivity (top left), cross-plane thermal conductivity (top right), the thermal diffusivity (bottom left) and the specific heat capacity (bottom right). Red lines: The first derivatives of ΔT with respect to each material parameter on the x-axis as a function of this parameter. In each figure only the parameter given on the abscissa is used as a variable, while all others were kept constant at an arbitrary mean value. 38

3.6. Workflow of the Bayesian method implemented to solve the inverse problem of finding the thermal conductance from Eq. 3.32. 39

3.7. Cumulative Gaussian distribution $\phi(\Sigma)$ (black line) and the following probability $p(\Sigma)$ of overlap between data o and model m_i (red line). 41

3.8. Visualization of the PDF computation process. Top left: Uniform prior. Top right: Anisotropy biased prior. Bottom left: Anisotropy biased prior with superimposed Gaussian around a previously known value $\{\kappa_{\mathrm{xy}}, \kappa_{\mathrm{z}}\}$. Bottom right: Posterior PDF. 42

3.9. Schematic of the 3ω structure layout (not to scale). The two outer pads are used to apply the AC current to the system, while the inner contact pads are used to measure the third harmonic of the voltage drop $U_{3\omega}$. 43

3.10. Layout of the Wheatstone bridge used to eliminate the U_ω combination from the total signal and thereby facilitate the isolation of the 3ω component in the lock-in. 44

3.11. Measurement workflow as carried out for all experiments. The left image of an Anfatec elock-in amplifier is printed by courtesy of the Anfatec AG. 45

3.12. The effect of the balance voltage on U_ω (black squares) and $U_{3\omega}$ (red circles). 47

3.13. Influence of erroneous values of the substrate thermal conductivity. The red circles correspond to the thermal conductivity of a YIG film on a GGG substrate with a certain thermal conductivity, while the black squares represent that regarding a substrate thermal conductivity increased by 10%. The blue and green solid lines represent the relative change after a manipulation of the substrate thermal conductivity by 1% and 10%, respectively. 48

3.14. Effect of ambient helium pressure on $U_{3\omega}$. 49

3.15. Linear relation of resistance and temperature of the heater structure (data: black line, fit: red line). The blue line represents the relative error of the data with respect to the linear fit. 50

4.1. Electrical resistivity of an as-grown $400\ \mathrm{nm}$ thick LCMO sample as a function of temperature for magnetic fields of 0 T (black squares) and 3 T (red squares). The resulting maximum magnetoresistance amounts to approx. 700%. 55

4.2. Phase diagram of $\mathrm{La}_{1-x}\mathrm{Ca}_x\mathrm{MnO}_3$ based on Schiffer et al. (1995). The denominations PM, FM and AFM abbreviate paramagnetic, ferromagnetic and antiferromagnetic, respectively. Reprinted figure with permission from Schiffer et al. (1995). Copyright 1995 by the American Physical Society. 56

4.3. Illustration of the double exchange mechanism by the example of $\mathrm{La}_{1-x}\mathrm{Ca}_x\mathrm{MnO}_3$. 58

4.4. Left: CaTiO_3 perovskite crystal found in Magnet Cove, Hot Spring County, Arkansas (USA) (Wikimedia, 2015). Right: Perovskite crystal structure. The blue circles depict atoms located at the A site (e.g. La or Ca), the red circles correspond to oxygen atoms and the green atom at the center of the unit cell corresponds to an atom at the B site (e.g. Mn). 59

4.5. Crystal field effect on the electronic energy levels in $\mathrm{La}^{3+}\mathrm{Mn}^{3+}\mathrm{O}_3^{2-}$ leading to a degeneracy in the $\mathrm{e_g}$ orbitals, which is lifted by the Jahn-Teller distortion, i.e. an elongation in the z direction. The states $\mathrm{e_g}$ and $\mathrm{t_{2g}}$ are degenerate in the middle section ('crystal field') and their splitting is only shown as a simplification. 61

4.6. The out-of-plane lattice constants of LCMO and the available substrates, STO, LAO and MGO. 63

4.7. AFM scan of a 400 nm thick LCMO sample grown on STO. Step flow growth mode is clearly visible. 67

4.8. Top: XRD spectrum including the STO substrate peak at 46.5° and the (002) LCMO peak at 47.3° with Laue oscillations on the right side of the peak (left) and rocking curve with a full width at half maximum of 0.07° (right) of the (002) peak of LCMO. Bottom: θ-2θ XRD scan of $\mathrm{Al_2O_3}$ and Au grown on MgO and identified reflections of face-centered cubic (fcc) Au, $\mathrm{Al_2O_3}$ and MgO. The analysis of this scan has been performed by Paulina Hołuj. 68

4.9. Magnetization hysteresis of as-grown LCMO deposited at a temperature of 735°C (black) and 830°C (red), LCMO grown at 830°C and post-annealed at a temperature of 800°C for two hours (green) and post-annealed at 950°C for two hours (blue). The substrate contributions have been subtracted and geometry factors have been accounted for. 69

4.10. Thermal conductivity as a function of temperature of an as-grown LCMO film of 400 nm thickness grown on STO. 71

4.11. Temperature dependent CMR (black squares) and MTR (red triangles) measured in an as-grown 400 nm thick sample on STO. The peak position of the MTR notably differs from that of the CMR. 72

4.12. Top: As-grown sample. Temperature dependence of the CMR (black squares) compared to the electronic contribution to the MTR (blue triangles) and the 'phononic' contribution to the MTR. Bottom: Temperature dependent MTR of an annealed sample of 400 nm thick LCMO grown on STO (red squares). Additionally, the expected MTR inferred from CMR data by the Wiedemann-Franz law is displayed (black line). 73

4.13. Effect of phenomena sorted by their characteristic length scale from small (top) to large (bottom) on strain, which in turn affects the phonon spectrum through dislocations of atoms. 74

4.14. Top: Temperature dependent MTR of as-grown samples of 400 nm and 200 nm LCMO on STO and 100 nm LCMO on MgO. Bottom: Annealed samples of 400 nm of LCMO grown on STO and LAO. 75

4.15. Exemplary demonstration of a fit (red line) of individual Lorentz profiles (green lines) to a spectrum of Raman shift at 633 nm (black line). 83

4.16. Raw Raman spectra at 633 nm of as-grown 400 nm LCMO on STO. The STO signal is invisible due to the limited information depth of the setup. The identification of the Jahn-Teller associated lines ('J-T') and that caused by a rotation of the oxygen octahedron ('rotation') is based on Abrashev (1999). The temperatures of the spectra are 300 K, 250 K, 200 K, 150 K, 125 K, 115 K, 105 K, 95 K and 85 K and are shifted vertically for clarity. 84

4.17. The temperature dependence of the intensity of the 480 cm^{-1} Raman line in as-grown 400 nm LCMO grown on STO (red circles) in comparison to the phononic contribution to the MTR (black squares). Open blue circles represent the intensity of the 480 cm^{-1} line in annealed 400 nm LCMO grown on STO. The annealed sample shows no spontaneous increase between 250 K and 200 K. 85

5.1. Magnetic field dependence of the signal at the third harmonic in the 300 nm thick sample between zero and 105 mT. ϕ is set to $0°$. The inset displays a f^{-1} fit to the data at 100 mT. The systematic reduction of the data at 92 mT is a measurement artifact. Error bars are omitted for clarity. 92
5.2. Top: The thermal conductivity of the Si substrate determined by the slope method. Bottom: The thermal conductivity of the Si substrate as a function of the rotation angle ϕ at an in-plane field of 105 mT. 93
5.3. Angle dependence of the thermal conductivity parallel (top) and perpendicular (bottom) to the film plane, κ_z. The red curve represents a $\sin^2(\phi)$ fit. Error bars are omitted for clarity in the k_z data ($\Delta\kappa_z \approx 0.2$ W/(m K)). 95
5.4. Field dependent thermal conductance determined by the slope method of an MgO substrate (red), an STO substrate (blue), Si wafers supplied by Sensitec (sample with thick Py film: black solid square, sample with thin Py film: magenta open square, blank wafer: green open square), Si wafers supplied by Singulus (orange) and by Crystec (blue). 97

6.1. Atomic Force Microscopy scan of a 150 nm thick YIG film (top). The black line indicates the position of a line scan presented below. 102
6.2. X-ray reflectivity curve (red) and fit (black) of a 5 nm thick gold layer on a GGG substrate. 103
6.3. The temperature oscillation in the heater structure in dependence of $\ln(2\omega)$ measured between 100 Hz to 100 kHz with ω the dimensionless angular frequency measured in Hz. The inset shows the temperature dependence of the resistance of the Au heater strip (black) and its temperature derivative (red). 104
6.4. Temperature dependent thermal conductances of YIG samples (first batch: 6.7 μm (red circles), 2.1 μm (black squares) and 190 nm (blue triangles)) and exponential fits to the high-temperature regions (solid lines). The inset displays the fit by the Callaway model around the maximum. 105
6.5. Peak temperature $T_{\max}$ (upper plot) of the thermal conductance and peak value $\kappa_{\max}$ (lower plot) as function of film thickness. The data point at 500 μm is taken from Boona and Heremans (2014). The black squares result from the first batch of samples, while the red circles correspond to the second batch of samples. The error bars are derived from the sample-to-sample variation of $T_{\max}$ and $\kappa_{\max}$. The blue and red lines in the lower plot indicate the dependence on the defect concentration parameter of the maximum in the thermal conductivity at constant scattering parameters other than the thickness effect. 106
6.6. FMR line width of YIG thin films with a thickness of 1.5 μm and 50 μm, respectively, taken at 9.6 GHz at the university of Halle by Tim Richter. The data were taken by Tim Richter at the university of Halle. 108

6.7. Magnetic field dependent contribution of the thermal conductivity of YIG films with thicknesses of 50.66 μm and 1.51 μm. 109
6.8. Angle dependent 3ω measurements on a 190 nm thick YIG sample on GGG taken at 0°, 45° and 90°. 110

BIBLIOGRAPHY

M. Abrashev, J. Bäckström, L. Börjesson, V. Popov, R. Chakalov, N. Kolev, R.-L. Meng, and M. Iliev. Raman spectroscopy of $\mathrm{CaMnO_3}$: Mode assignment and relationship between Raman line intensities and structural distortions. *Phys. Rev. B*, 65(18):184301, 2002.

M. V. Abrashev. Raman Study of the Variations of the Jahn-Teller Distortions through the Metal - Insulator Transition in Magnetoresistive $\mathrm{La_{0.7}Ca_{0.3}MnO_3}$ Thin Films. *Phys. Stat. Sol.*, 215:631–636, 1999.

M. Agrawal, V. I. Vasyuchka, A. A. Serga, A. D. Karenowska, G. A. Melkov, and B. Hillebrands. Direct measurement of magnon temperature: New insight into magnon-phonon coupling in magnetic insulators. *Phys. Rev. Lett.*, 111:107204, 2013.

M. T. Alam, M. P. Manoharan, M. A. Haque, C. Muratore, and A. Voevodin. Influence of strain on thermal conductivity of silicon nitride thin films. *J. Micromech. Microeng.*, 22: 045001, 2012.

M. Althammer, S. Meyer, H. Nakayama, M. Schreier, S. Altmannshofer, M. Weiler, H. Huebl, S. Geprägs, M. Opel, R. Gross, D. Meier, C. Klewe, T. Kuschel, J.-M. Schmalhorst, G. Reiss, L. Shen, A. Gupta, Y.-T. Chen, G. E. W. Bauer, E. Saitoh, and S. T. B. Gönnenwein. Quantitative study of the spin hall magnetoresistance in ferromagnetic insulator/normal metal hybrids. *Phys. Rev. B*, 87:224401, 2013.

P. W. Anderson and H. Hasegawa. Considerations on double exchange. *Phys. Rev.*, 100: 675–681, 1955.

G. E. W. Bauer, E. Saitoh, and B. J. van Wees. Spin caloritronics. *Nat. Mater.*, 11:391–399, 2012.

N. G. Bebenin. Ferromagnetic manganites $\mathrm{La_{1-x}Ca_xMnO_3}$. *Phys. Met. Metallogr.*, 111(3): 236–252, 2011.

F. Bloch. Zum elektrischen Widerstandsgesetz bei tiefen Temperaturen. *Z. Phys.*, 59:208–214, 1930.

M. L. Boas. *Mathematical Methods in the Physical Sciences*. Wiley & Sons, Inc., Hoboken, New Jersey, 2006.

S. R. Boona and J. P. Heremans. Magnon thermal mean free path in yttrium iron garnet. *Phys. Rev. B*, 90:064421, 2014.

S. R. Boona, R. C. Myers, and J. P. Heremans. Spin caloritronics. *Energy Environ. Sci.*, 7: 885–910, 2014.

T. Borca-Tasciuc, A. R. Kumar, and G. Chen. Data reduction in 3ω method for thin-film thermal conductivity determination. *Rev. Sci. Instrum.*, 72(4):2139, 2001.

D. G. Cahill. Thermal conductivity measurement from 30 to 750 K: the 3ω method. *Rev. Sci. Instrum.*, 61(2):802, 1990.

D. G. Cahill. erratum. *Rev. Sci. Instrum.*, 73:3701, 2002.

D. G. Cahill and R. O. Pohl. Thermal conductivity of amorphous solids above the plateau. *Phys. Rev. B*, 35(8):4067–4073, 1987.

R. Cai, Y. Wang, X. Liu, W. Gao, Y. Chen, and J. Sun. Origin of Different Growth Modes for Epitaxial Manganite Films. *J. Am. Ceram. Soc.*, 96(5):1660–1665, 2013.

J. Callaway. Model for lattice thermal conductivity at low temperatures. *Phys. Rev.*, 113: 1046–1051, 1959.

J. Callaway and R. Boyd. Model for lattice thermal conductivity at low temperatures. *Phys. Rev.*, 134:A1655, 1964.

G. Campillo, A. Berger, J. Osorio, J. E. Pearson, S. D. Bader, E. Baca, and P. Prieto. Substrate dependence of magnetic properties of $La_{0.67}Ca_{0.33}MnO_3$ films. *J. Magn. Magn. Mater.*, 237: 61–68, 2001.

W. S. Capinski, H. J. Maris, T. Ruf, M. Cardona, K. Ploog, and D. S. Katzer. Thermal-conductivity measurements of GaAs/AlAs superlattices using a picosecond optical pump-and-probe technique. *Phys. Rev. B*, 59:8105–8113, 1999.

H. S. Carslaw and J. C. Jäger. *Conduction of Heat in Solids*. Oxford University Press, Oxford, 1959.

V. Cherepanov, I. Kolokolov, and V. S. L'Vov. The saga of YIG: spectra, thermodynamics, interaction and relaxation of magnons in a complex magnet. *Physics Reports*, 229, 1993.

G. Czycholl, editor. *Theoretische Festkörperphysik*. Springer-Verlag, Berlin ,Heidelberg, 3rd edition, 2008.

C. Dames and G. Chen. 1ω, 2ω, and 3ω Methods for Measurements of Thermal Properties. *Rev. Sci. Instrum.*, 76(12):124902, 2005.

P. G. de Gennes. Effects of double exchange in magnetic crystals. *Phys. Rev.*, 118:141–154, 1960.

J. Fabian, S. D. Sarma, I. Žutić, and S. Das Sarma. Spintronics: Fundamentals and applications. *Rev. Mod. Phys.*, 76(April):323–410, 2004.

A. Feldman. Algorithm for Solutions of the Thermal Diffusion Equation in a Stratified Medium with a Modulated Heating Source. *NIST Interagency/Internal Report (NISTIR)*, 5928, 1996.

Manuel Feuchter. *Investigations on Joule heating applications by multiphysical continuum simulations in nanoscale systems*. PhD thesis, Karlsruhe Institute of Technology, 2014.

K. Fuchs. *Proc. Camb. Phil. Soc.*, 34:100, 1938.

H. Fujishiro. Heat transport anomalies around ferromagnetic and charge-order transitions in $\mathrm{La}_{1x}\mathrm{Ca}_x\mathrm{MnO}_3$. *AIP Conf. Proc.*, 554(2001):433–436, 2001.

T. Fukuda and H. J. Scheel. *Crystal Growth Technology*. Wiley, New York, 2003.

S. Geller, G. P. Espinosa, and P. B. Crandall. Thermal expansion of yttrium and gadolinium iron, gallium and aluminum garnets. *J. Appl. Cryst.*, 2:86, 1969.

S. Geprägs, A. Kehlberger, T. Schulz, C. Mix, F. Della Coletta, S. Meyer, A. Kamra, M. Althammer, G. Jakob, H. Huebl, R. Gross, S. T.B. Gönnenwein, and M. Kläui. Origin of the spin Seebeck effect probed by temperature dependent measurements in $\mathrm{Gd}_3\mathrm{Fe}_5\mathrm{O}_{12}$. *arXiv:1405.4971*, 2014.

T. L. Gilbert. A Phenomenologial Theory of Damping in Ferromagnetic Materials. *IEEE Trans. Magn.*, 40(6):3443 – 3449, 2004.

C. J. Glassbrenner and G. A. Slack. Thermal Conductivity of Silicon and Germanium from 3řK to the Melting Point. *Phys. Rev.*, 134(4A):A1058 – A1069, 1964.

S. T. B. Gönnenwein. private communication.

K. E. Goodson, O. W. Käding, M. Roesler, and R. Zachai. Experimental investigation of thermal conduction normal to diamond-silicon boundaries. *J. Appl. Phys.*, 77(4):1385–1392, 1995.

E. Grüneisen. Die Abhängigkeit des elektrischen Widerstandes reiner Metalle von der Temperatur. *Ann. Phys.*, 5:530–540, 1933.

E. M. Hankiewicz, G. Vignale, and Y. Tserkovnyak. Inhomogeneous Gilbert damping from impurities and electron-electron interactions. *Phys. Rev. B*, 78:020404, 2008.

M. E. Hawley, C. D. Adams, P. N. Arendt, E. L. Brosha, F. H. Garzon, R. J. Houlton, M. F. Hundley, R. H. Heffner, Q. X. Jia, J. Neumeier, and X. D. Wu. CMR films structure as a function of growth and processing. *J. Cryst. Growth*, 174(1-4):455–463, 1997.

A. M. Hofmeister. Thermal diffusivity of garnets at high temperature. *Phys. Chem. Miner.*, 33 (1):45–62, 2006.

T Holstein. Studies of polaron motion: Part I. The molecular-crystal model. *Ann. Phys.*, 8(3): 325–342, 1959.

P. Hołuj, C. Euler, B. Balke, U. Kolb, and G. Jakob. Reduced thermal conductivity of TiNiSn/HfNiSn superlattices. 2015.

S. Hunklinger, editor. *Festkörperphysik*. Oldenbourg Wissenschaftsverlag GmbH, München, 2007.

M. N. Iliev and M. V. Abrashev. Raman phonons and Raman Jahn-Teller bands in perovskite-like manganites. *J. Raman Spectrosc.*, 32(10):805–811, 2001.

M. N. Iliev, H.-G. Lee, V. N. Popov, Y. Y. Sun, C. Thomsen, R. L. Meng, and C. W. Chu. Raman spectroscopy of orthorhombic perovskitelike $\mathrm{YMnO_3}$ and $\mathrm{LaMnO_3}$. *Phys. Rev. B*, 57 (5):2872–2877, 1998.

M. Isasa, E. Villamor, L. E. Hueso, M. Gradhand, and F. Casanova. Temperature dependence of spin diffusion length and spin hall angle in au and pt. *Phys. Rev. B*, 91:024402, 2015.

T. Jäger. *Thermoelectric properties of TiNiSn and with reduced thermal conductivities*. PhD thesis, University of Mainz, 2013.

H. A. Jahn and E. Teller. Stability of Polyatomic Molecules in Degenerate Electronic States. I. Orbital Degeneracy. *Proceedings of the Royal Society of London. Series A, Mathematical and Physical Sciences*, 161(905):220–235, 1937.

G. Jakob, F. Martin, W. Westerburg, and H. Adrian. Magnetoresistivity and crystal structure of epitaxial La0.67Ca0.33MnO3 films. *J. Magn. Magn. Mater.*, 5:1247–1248, 1998a.

G. Jakob, F. Martin, W. Westerburg, and H. Adrian. Evidence of charge-carrier compensation effects in $\mathrm{La_{0.67}Ca_{0.33}MnO_3}$. *Phys. Rev. B*, 57(17):252–255, 1998b.

G. Jakob, W. Westerburg, F. Martin, and H. Adrian. Small-polaron transport in $\mathrm{La_{0.67}Ca_{0.33}MnO_3}$ thin films. *Phys. Rev. B*, 58(22):14966–14970, 1998c.

C. M. Jaworski, J. Yang, S. Mack, D. D. Awschalom, R. C. Myers, and J. P. Heremans. Spin-Seebeck Effect: A Phonon Driven Spin Distribution. *Phys. Rev. Lett.*, 106(18):186601, 2011.

F. J. Jedema, A. T. Filip, and B. J. van Wees. Electrical spin injection and accumulation at room temperature in an all-metal mesoscopic spin valve. *Nature*, 410:345–348, 2001.

S. Jin, T. H. Tiefel, M. McCormack, R. A. Fastnacht, R. Ramesh, and L. H. Chen. Thousandfold change in resistivity in magnetoresistive la-ca-mn-o films. *Science*, 264(5157):413–415, 1994.

G. H. Jonker and J. H. van Santen. Ferromagnetic compounds of manganese with perovskite structure. *Physica*, 16(3):337 – 349, 1950.

P. L. Kapitza. Heat Transfer and Superfluidity of Helium II. *Phys. Rev.*, 60:354–355, 1941.

A. Kehlberger, R. Röser, G. Jakob, U. Ritzmann, D. Hinzke, U. Nowak, M. C. Onbasli, D. H. Kim, C. A. Ross, M. B. Jungfleisch, B. Hillebrands, and M. Kläui. Determination of the origin of the spin Seebeck effect - bulk vs. interface effects. 2013.

J. Kimling. *Transport Phenomena in Thermoelectric and Ferromagnetic Nanostructures*. PhD thesis, University of Hamburg, 2013.

J. Kimling, J. Gooth, and K. Nielsch. Anisotropic magnetothermal resistance in Ni nanowires. *Phys. Rev. B*, 87(9):094409, 2013.

Charles Kittel. *Festkörperphysik*. Oldenbourg Wissenschaftsverlag GmbH, München, 14th edition, 2006.

H. A. Kramers. Théorie générale de la rotation paramagnétique dans les cristaux. *Proc. Amsterdam Acad.*, 33:959, 1930.

H.-U. Krebs, M. Weisheit, S. Erik, T. Scharf, C. Fuhse, M. St, K. Sturm, M. Seibt, H. Kijewski, D. Nelke, E. Panchenko, and M. Buback. Pulsed Laser Deposition (PLD) - a Versatile Thin Film Technique UHV-chamber. *Adv. Solid State Phys.*, page 505, 2003.

K. Kubo and N. Ohata. A Quantum Theory of Double Exchange I. *J. Phys. Soc. Jpn.*, 33, 1972.

A. Kumar. Low-temperature magnon thermal conductivity of ferromagnetic insulators with impurities. *Phys. Rev. B*, 25:3369–3373, 1982.

G. Langer, J. Hartmann, and M. Reichling. Thermal conductivity of thin metallic films measured by photothermal profile analysis. *Rev. Sci. Instrum.*, 68(3):1510–1513, 1997.

I. R. Lewis and H. G. M. Edwards, editors. *Handbook of Raman Spectroscopy*. Marcel Dekker, New York, 2001.

N. Liebing, S. Serrano-Guisan, K. Rott, G. Reiss, J. Langer, B. Ocker, and H. W. Schumacher. Tunneling magnetothermopower in magnetic tunnel junction nanopillars. *Phys. Rev. Lett.*, 107:177201, 2011.

Lüthi, B. Thermal conductivity of yttrium iron garnet. *J. Phys. Chem. Sol.*, 23(1âĂŞ2):35 – 38, 1962.

G. Y. Lyubarskii, editor. *Application of Group Theory in Physics*. Pergamon Press, New York, 1960.

A. Manzin, V. Nabaei, H. Corte-Leon, O. Kazakova, P. Krzysteczko, and H.W. Schumacher. Modeling of anisotropic magnetoresistance properties of permalloy nanostructures. *IEEE Transactions on Magnetics*, 50(4):1–4, 2014.

F Martin, G Jakob, W Westerburg, and H Adrian. Growth mechanism and transport properties of thin La0.67Ca0.33MnO3 films. *J. Magn. Magn. Mater.*, 197:509–511, 1999.

L.W. Martin, Y.-H. Chu, and R. Ramesh. Advances in the growth and characterization of magnetic, ferroelectric, and multiferroic oxide thin films. *Materials Science and Engineering: R: Reports*, 68:89 – 133, 2010.

R.A. Matula. Electrical resistivity of copper, gold, palladium and silver. *J. Phys Chem. Ref. Data*, 8(4):1179–1298, 1979.

T.R. McGuire and R.I. Potter. Anisotropic magnetoresistance in ferromagnetic 3d alloys. *IEEE Transactions on Magnetics*, 11(4):1018–1038, 1975.

S. Meyer, M. Althammer, S. Geprägs, M. Opel, R. Gross, and S. T. B. Gönnenwein. Temperature dependent spin transport properties of platinum inferred from spin hall magnetoresistance measurements. *Appl. Phys. Lett.*, 104(24):242411, 2014.

E. N. Mitchell, H. B. Haukaas, H. D. Bale, and J. B. Streeper. Compositional and thickness dependence of the ferromagnetic anisotropy in resistance of iron-nickel films. *J. Appl. Phys.*, 35(9):2604–2608, 1964.

C. Mix. *Messung der thermischen Leitfähigkeit von dünnen Schichten*. Diploma thesis, University of Mainz, 2010.

C. Mix. *Laserablation von oxidischen Multilagenstrukturen zur Untersuchung von heteroepitaktischen Grenzflächenzuständen*. PhD thesis, University of Mainz, 2013.

V. Moshnyaga and K. Samwer. Electron-lattice correlations and phase transitions in CMR manganites. *Ann. Phys.*, 523(8-9):652–663, 2011.

V. Moshnyaga, L. Sudheendra, O. Lebedev, S. Köster, K. Gehrke, O. Shapoval, a. Belenchuk, B. Damaschke, G. van Tendeloo, and K. Samwer. A-Site Ordering versus Electronic Inhomogeneity in Colossally Magnetoresistive Manganite Films. *Phys. Rev. Lett.*, 97(10): 107205, 2006.

C. Moure and O. Peña. Magnetic features in REMeO$_3$ perovskites and their solid solutions (RE=rare-earth, Me=Mn, Cr). *J. Magn. Magn. Mater.*, 337-338:1–22, 2013.

A. Mukherjee, W. S. Cole, P. Woodward, M. Randeria, and N. Trivedi. Theory of Strain-Controlled Magnetotransport and Stabilization of the Ferromagnetic Insulating Phase in Manganite Thin Films. *Phys. Rev. Lett.*, 110(15):157201, 2013.

G. Nahrwold, J. M. Scholtyssek, S. Motl-Ziegler, O. Albrecht, U. Merkt, and G. Meier. Structural, magnetic, and transport properties of permalloy for spintronic experiments. *J. Appl. Phys.*, 108(1):013907, 2010.

H. Nakayama, M. Althammer, Y.-T. Chen, K. Uchida, Y. Kajiwara, D. Kikuchi, T. Ohtani, S. Geprägs, M. Opel, S. Takahashi, R. Gross, G. E. W. Bauer, S. T. B. Gönnenwein, and E. Saitoh. Spin Hall Magnetoresistance Induced by a Nonequilibrium Proximity Effect. *Phys. Rev. Lett.*, 110(20):206601, 2013.

C. Nelson, M. Zimmermann, Y. Kim, J. Hill, Doon Gibbs, V. Kiryukhin, T. Koo, S.-W. Cheong, D. Casa, B. Keimer, Y. Tomioka, Y. Tokura, T. Gog, and C. Venkataraman. Correlated polarons in dissimilar perovskite manganites. *Phys. Rev. B*, 64(17):174405, 2001.

T. Ohnishi, K. Shibuya, M. Lippmaa, D. Kobayashi, H. Kumigashira, M. Oshima, and H. Koinuma. Preparation of thermally stable TiO2-terminated SrTiO3(100) substrate surfaces. *Appl. Phys. Lett.*, 85(2):272–274, 2004.

T. Okuda and Y. Tomioka. Low-temperature properties of $\mathrm{La}_{1-x}\mathrm{Ca}_x\mathrm{MnO}_3$ single crystals: Comparison with $\mathrm{La}_{1-x}\mathrm{Sr}_x\mathrm{MnO}_3$. *Phys. Rev. B*, 61(12):8009–8015, 2000.

B. W. Olson, S. Graham, and K. Chen. A practical extension of the 3ω method to multilayer structures. *Rev. Sci. Instrum.*, 76(5):053901, 2005.

M. C. Onbasli, A. Kehlberger, D. H. Kim, G. Jakob, M. Kläui, A. V. Chumak, B. Hillebrands, and C. A. Ross. Pulsed laser deposition of epitaxial yttrium iron garnet films with low gilbert damping and bulk-like magnetization. *APL Mat.*, 2:106102, 2014.

M. N. Ou, T. J. Yang, S. R. Harutyunyan, Y. Y. Chen, C. D. Chen, and S. J. Lai. Electrical and thermal transport in single nickel nanowire. *Appl. Phys. Lett.*, 92(6):063101, 2008.

C. A. Paddock and G. L. Eesley. Transient thermoreflectance from thin metal films. *J. Appl. Phys.*, 60(1):285–290, 1986.

N. P. Padture and P. G. Klemens. Low Thermal Conductivity in Garnets. *J. Am. Ceram. Soc.*, 80(4):1018–1020, 1997.

B. Y. Pan, T. Y. Guan, X. C. Hong, S. Y. Zhou, X. Qiu, H. Zhang, and S. Y. Li. Specific heat and thermal conductivity of ferromagnetic magnons in Yttrium Iron Garnet. *Europhys. Lett.*, 103(3):37005, 2013.

A. E. Pantoja, H. J. Trodahl, R. G. Buckley, Y. Tomioka, and Y. Tokura. Raman spectroscopy of orthorhombic LCMO, x=0.1-0.3. *J. Phys. - Cond. Mat.*, 13:3741–3752, 2001.

M. Paranjape and A. K. Raychaudhuri. Annealing induced grain growth and grain connectivity in an epitaxial film of $\mathrm{LaLa_{0.67}Ca_{0.33}MnO_3}$ and its effect on low field colossal magnetoresistance. *Solid State Commun.*, 123(12):521–525, 2002.

C. E. Patton. Magnetic excitations in solids. *Phys. Rev.*, 103:251, 1984.

V. B. Podobedov, D. B. Romero, A. Weber, J. P. Rice, R. Schreekala, M. Rajeswari, R. Ramesh, T. Venkatesan, and H. D. Drew. Diagnostics of 'colossal' magnetoresistance manganite films by Raman spectroscopy. *Appl. Phys. Lett.*, 73(22):3217, 1998.

V. N. Popov. Shell model parameters for layered copper oxides. *J. Phys. Condens. Matter*, 7 (8):1625–1638, 1995.

L. Pottier. Micrometer scale visualization of thermal waves by photoreflectance microscopy. *Appl. Phys. Lett.*, 64(13):1618–1619, 1994.

R. C. Powell, editor. *Symmetry, Group Theory and the Physical Properties of Crystals*. Springer, New York, 2010.

A. P. Ramirez. Colossal magnetoresistance. *J. Phys Condens. Matter*, 9:8171–8199, 1997.

R. A. Rao, D. Lavric, T. K. Nath, C. B. Eom, L. Wu, and F. Tsui. Effects of film thickness and lattice mismatch on strain states and magnetic properties of $\mathrm{La_{0.8}Ca_{0.2}MnO_3}$ thin films. *J. Appl. Phys.*, 85(8):4794, 1999.

E. Rebhan, editor. *Theoretische Physik II*. Elsevier GmbH, München, 2005.

S. M. Rezende, R. L. Rodríguez-Suárez, J. C. Lopez Ortiz, and A. Azevedo. Thermal properties of magnons and the spin seebeck effect in yttrium iron garnet/normal metal hybrid structures. *Phys. Rev. B*, 89:134406, 2014.

U. Ritzmann, D. Hinzke, and U. Nowak. Propagation of thermally induced magnonic spin currents. *Phys. Rev. B*, 89:024409, 2014.

H. Röder, Jun Zang, and A. R. Bishop. Lattice effects in the colossal-magnetoresistance manganites. *Phys. Rev. Lett.*, 76:1356–1359, 1996.

L. M. Rodriguez-Martinez and J. P. Attfield. Cation disorder and size effects in magnetoresistive manganese oxide perovskites. *Phys. Rev. B*, 54(22):R15622–R15625, 1996.

A. Rosencwaig, J. Opsal, W. L. Smith, and D. L. Willenborg. Detection of thermal waves through optical reflectance. *Appl. Phys. Lett.*, 46(11):1013–1015, 1985.

E. Ruch and A. Schönhofer. Ein Beweis des Jahn-Teller-Theorems mit Hilfe eines Satzes über die Induktion von Darstellungen endlicher Gruppen. *Theor. Chim. Acta*, 3(4):291–304, 1965.

M. B. Salamon and M. Jaime. The physics of manganites: Structure and transport. *Rev. Mod. Phys.*, 73:583–628, 2001.

P. Schiffer, A. P. Ramirez, W. Bao, and S.-W. Cheong. Low Temperature Magnetoresistance and the Magnetic Phase Diagram of $La_{1-x}Ca_xMnO_3$. *Phys. Rev. Lett.*, 75(18):3336–3339, 1995.

A. Schönflies. *Krystallsysteme und Krystallstructur*. Habilitation, University of Göttingen, 1891.

M. Schreier, A. Kamra, M. Weiler, J. Xiao, G. E. W. Bauer, R Gross, and S. T. B. Gönnenwein. Magnon, phonon, and electron temperature profiles and the spin seebeck effect in magnetic insulator/normal metal hybrid structures. *Phys. Rev. B*, 88:094410, 2013.

F. Siebert and P. Hildebrandt, editors. *Vibrational Spectroscopy in Life Science*. Wiley, Weinheim, 2008.

P. K. Siwach, H. K. Singh, and O. N. Srivastava. Effect of strain relaxation on magnetotransport properties of epitaxial $La_{0.7}Ca_{0.3}MnO_3$ films. *cond-mat/0503712*, 2005.

P. K. Siwach, H. K. Singh, and O. N. Srivastava. Influence of strain relaxation on magnetotransport properties of epitaxial $La_{0.7}Ca_{0.3}MnO_3$ films. *J. Phys. Condens. Matter*, 18(43): 9783–9794, 2006.

G. A. Slack and D. W. Oliver. Thermal Conductivity of Garnets and Phonon Scattering by Rare-Earth Ions. *Phys. Rev. B*, 4(2):592–609, 1971.

E. Smith and G. Dent, editors. *Modern Raman Spectroscopy – A Practical Approach*. John Wiley & Sons Ltd, New York, 2005.

E. H. Sondheimer. The mean free path of electrons in metals. *Adv. Phys.*, 50:499, 2001.

A. Sposito, T. C. May-Smith, G. B. G. Stenning, P. A. J. de Groot, and R. W. Eason. Pulsed laser deposition of high-quality μm-thick YIG films on YAG. *Opt. Mater. Express*, 3(5):624, 2013.

A. M. Stuart. Inverse Problems: A Bayesian Perspective. *Acta Numerica*, 19:451–559, 2010.

P. F. Sullivan and G. Seidel. Steady-state, ac-temperature calorimetry. *Phys. Rev.*, 173:679–685, 1968.

A. C. Tam. Applications of photoacoustic sensing techniques. *Rev. Mod. Phys.*, 58:381–431, 1986.

X. Tian, M. E. Itkis, E. B. Bekyarova, and R. C. Haddon. Anisotropic Thermal and Electrical Properties of Thin Thermal Interface Layers of Graphite Nanoplatelet-Based Composites. *Sci. Rep.*, 3:1710, 2013.

R. Tripathi, A. Dogra, A. K. Srivastava, V. P. S. Awana, R. K. Kotnala, G. L. Bhalla, and H. Kishan. Influence of sintering temperature and oxygen annealing on transport properties of $La_{0.67}Ca_{0.33}MnO_3$. *J. Phys. D. Appl. Phys.*, 42(2):025003, 2009.

T. M. Tritt, editor. *Thermal Conductivity*. Kluwer Academic / Plenum Publishers, New York, 2004.

K. Uchida, J. Xiao, H. Adachi, J. Ohe, S. Takahashi, J. Ieda, T. Ota, Y. Kajiwara, H. Umezawa, H. Kawai, G. E. W. Bauer, S. Maekawa, and E. Saitoh. Spin Seebeck insulator. *Nat. Mater.*, 9(11):894–897, 2010.

C. M. Varma. Electronic and magnetic states in the giant magnetoresistive compounds. *Phys. Rev. B*, 54(10):7328–7333, 1996.

T. Venkatesan. Pulsed laser deposition - invention or discovery? *J. Phys. D. Appl. Phys.*, 47 (3):034001, 2014.

D. W. Visser, A. P. Ramirez, and M. A. Subramanian. Thermal Conductivity of Manganite Perovskites: Colossal Magnetoresistance as a Lattice-Dynamics Transition. *Phys. Rev. Lett.*, 78(20):3947–3950, 1997.

C. Vittoria, P. Lubitz, P. Hansen, and W. Tolksdorf. FMR linewidth measurements in bismuth-substituted YIG. *J. Appl. Phys.*, 57(8):3699–3700, 1985.

F. Völklein and T. Zetterer, editors. *Praxiswissen Mikrosystemtechnik*. Friedr. Vieweg & Sohn Verlag / GWV Fachverlage GmbH, Wiesbaden, 2006.

F. Völklein, H. Reith, T. W. Cornelius, M. Rauber, and R. Neumann. The experimental investigation of thermal conductivity and the Wiedemann-Franz law for single metallic nanowires. *Nanotechnology*, 20:325706, 2009.

W. H. Weber and R. Merlin, editors. *Raman Scattering in Materials Science*. Springer, Berlin, 2000.

W. Westerburg, G. Jakob, F. Martin, and H. Adrian. High-temperature transport properties of Lao.67Cao.33MnO3 films. *J. Magn. Magn. Mater.*, 197:536–538, 1999a.

W. Westerburg, F. Martin, S. Friedrich, M. Maier, and G. Jakob. Current dependence of grain boundary magnetoresistance in $La_{0.67}Ca_{0.33}MnO_3$ films. *J. Appl. Phys.*, 86:2173–2177, 1999b.

Wikimedia. Perowskite, Magnet Cove, Hot Spring County, Arkansas, USA, 2015. URL `upload.wikimedia.org/wikipedia/commons/0/06/Perovskite-bem-52b.jpg`.

D. C. Worledge, G. J. Snyder, M. R. Beasley, T. H. Geballe, R. Hiskes, and S. DiCarolis. Anneal-tunable Curie temperature and transport of $La_{0.67}Ca_{0.33}MnO_3$. *J. Appl. Phys.*, 80 (9):5158–5161, 1996.

Y. M. Xiong, T. Chen, G. Y. Wang, X. H. Chen, X. Chen, and C. L. Chen. Raman spectra in epitaxial thin film $La_{1-x}Ca_xMnO_3$ (x=0.33, 0.5) grown on different substrates. *Phys. Rev. B.*, 70:094407, 2004.

C. Zener. Interaction between the d-Shells in the Transition Metals. II. Ferromagnetic Compounds of Manganese with Perovskite Structure. *Phys. Rev.*, 82(3):403–405, 1951.

G.-M. Zhao, K. Conder, H. Keller, and K. A. Müller. Giant oxygen isotope shift in the magnetoresistive perovskite $La_{1-x}Ca_xMnO_{3+y}$. *Lett. to Nat.*, 381:676–678, 1996.

R. Zhao, K. Jin, Z. Xu, H. Guo, L. Wang, C. Ge, H. Lu, and G. Yang. The oxygen vacancy effect on the magnetic property of the $LaMnO_{3-\delta}$ thin films. *Appl. Phys. Lett.*, 102(12): 122402, 2013.

LIST OF PUBLICATIONS

P1 **Reduced thermal conductivity of half-Heusler superlattices**.
Tino Jäger, Paulina Hołuj, Christian Mix, Christoph Euler, Myriam Haydee Aguirre, Sascha Populoh, Anke Weidenkaff, and Gerhard Jakob.
Semicond. Sci. Technol. **29**, 124003 (2014).

P2 **Magnetic field dependent thermal conductance in $\mathbf{La_{0.67}Ca_{0.33}MnO_3}$**.
Christoph Euler, Paulina Hołuj, Andreas Talkenberger, and Gerhard Jakob.
Journal of Magnetism and Magnetic Materials **381**, 188-193 (2015).

P3 **Reduced thermal conductivity of TiNiSn/HfNiSn superlattices**.
Paulina Hołuj, Christoph Euler, Benjamin Balke, Ute Kolb, and Gerhard Jakob.
Submitted to Physical Review Letters (2015).

P4 **Thermal conductance of thin film YIG determined using Bayesian statistics**.
Christoph Euler, Paulina Hołuj, Thomas Langner, Andreas Kehlberger, Vitaliy Vasyuchka, Matthias Kläui, and Gerhard Jakob.
Physical Review B **92**, 094406(2015).

P5 **Half-Heusler superlattices as model systems for nanostructured thermoelectrics**.
Paulina Hołuj, Tino Jäger, Christoph Euler, Emigdio Chavez Angel, Ute Kolb, Mathis M. Müller, Benjamin Balke, Myriam Haydee Aguirre, Sascha Populoh, Anke Weidenkaff, and Gerhard Jakob.
Submitted to Physica Status Solidi (2015).

ACKNOWLEDGMENTS

Removed due to data privacy.

CURICULUM VITAE

Removed due to data privacy.

EIDESSTATTLICHE ERKLÄRUNG

Hiermit erkläre ich an Eides statt, dass ich die vorliegende Dissertation selbstständig, ohne fremde Hilfe und nur unter Verwendung der angegebenen Hilfsmittel verfasst habe. Ich habe von der Ordnung zur Sicherung guter wissenschaftlicher Praxis in Forschung und Lehre und zum Umgang mit wissenschaftlichem Fehlverhalten Kenntnis genommen. Diese Dissertation wurde nicht als Prüfungsarbeit bei anderen Prüfungen eingereicht. Gleiche Abhandlungen oder Teile dieser Arbeit wurden nicht bei einer anderen Fakultät oder einem anderen Fachbereich als Dissertation eingereicht.

Mainz,